

Development and Evaluation of Radio Frequency Antennas for 7 Tesla Ultrahigh- Field Magnetic Resonance Imaging

Stefan Rietsch

Erwin L. Hahn Institute for Magnetic Resonance Imaging

Development and Evaluation of Radio Frequency Antennas for 7 Tesla Ultrahigh-Field Magnetic Resonance Imaging

Proefschrift

ter verkrijging van de graad van doctor
aan de Radboud Universiteit Nijmegen
op gezag van de rector magnificus prof. dr. J.H.J.M. van Krieken,
volgens besluit van het college van decanen
in het openbaar te verdedigen op woensdag 24 april 2019
om 10.30 uur precies

door
Stefan Hans Gerhard Rietsch
geboren op 29 juni 1988
te Erlangen, Duitsland

Promotoren: Prof. dr. David G. Norris
Prof. dr. Harald H. Quick, Universität Duisburg-Essen,
Duitsland

Manuscriptcommissie: Prof. dr. Arend Heerschap
Prof. dr. Andrew G. Webb, Universiteit Leiden
Dr. Dennis W.J. Klomp, Universitair Medisch Centrum
Utrecht

The studies in this thesis were performed at the Erwin L. Hahn Institute for Magnetic Resonance Imaging in Essen, Germany.

ISBN 978-3-00-061046-2

Copyright © 2018 by Stefan Rietsch, all rights reserved.

The copyrights of the articles and illustrations of chapter 2, 3, 4 and 5 that have been published or accepted for publication have been transferred to Medical Physics, American Institute of Physics, College Park, MD and Magnetic Resonance in Medicine, John Wiley & Sons Inc., Hoboken NY. The author has obtained the rights for their reproduction in this thesis.

Printed by: duprintes Print & Copy Center, Essen, Germany

Development and Evaluation of Radio Frequency Antennas for 7 Tesla Ultrahigh-Field Magnetic Resonance Imaging

Doctoral Thesis

to obtain the degree of doctor

from Radboud University Nijmegen

on the authority of the Rector Magnificus prof. dr. J.H.J.M. van Krieken,

according to the decision of the Council of Deans

to be defended in public on Wednesday, April 24, 2019

at 10.30 hours

by

Stefan Hans Gerhard Rietsch

born on June 29, 1988

in Erlangen (Germany)

Supervisors: Prof. dr. David G. Norris
Prof. dr. Harald H. Quick, University of Duisburg-Essen,
Germany

Doctoral Thesis Committee:

Prof. dr. Arend Heerschap
Prof. dr. Andrew G. Webb, Leiden University
Dr. Dennis W.J. Klomp, University Medical Center Utrecht

The studies in this thesis were performed at the Erwin L. Hahn Institute for Magnetic Resonance Imaging in Essen, Germany.

ISBN 978-3-00-061046-2

Copyright © 2018 by Stefan Rietsch, all rights reserved.

The copyrights of the articles and illustrations of chapter 2, 3, 4 and 5 that have been published or accepted for publication have been transferred to Medical Physics, American Institute of Physics, College Park, MD and Magnetic Resonance in Medicine, John Wiley & Sons Inc., Hoboken NY. The author has obtained the rights for their reproduction in this thesis.

Printed by: duprintes Print & Copy Center, Essen, Germany

For my family.

Contents

List of original publications	15
1 Introduction	17
1.1 The history of magnetic resonance imaging	17
1.2 Physical principles of magnetic resonance imaging	20
1.3 Objective of this thesis	45
2 Impact of different meander sizes on the RF transmit performance and coupling of microstrip line elements at 7 T	53
2.1 Introduction	55
2.2 Methods	56
2.3 Results	62
2.4 Discussion	82
2.5 Conclusion	85
3 Parallel Transmit Capability of Various RF Transmit Elements and Arrays at 7T MRI	91
3.1 Introduction	93
3.2 Methods	96
3.3 Results	104
3.4 Discussion	114
3.5 Conclusion	117
4 An 8-channel transmitter 7-channel receive RF coil setup for high SNR ultrahigh-field MRI of the shoulder at 7T	135
4.1 Introduction	137
4.2 Materials and Methods	140
4.3 Results	149
4.4 Discussion	164
4.5 Conclusions	168
5 7T ultra-high field body MR imaging with an 8-channel transmit / 32-channel receive radiofrequency coil array	179
5.1 Introduction	181
5.2 Methods	183
5.3 Results	184

5.4 Discussion	203
5.5 Conclusions	207
6 Summary	223
7 Samenvatting	227
8 Perspectives	231
Acknowledgments	239
Curriculum Vitae	245

List of original publications

Parts of this thesis are published in the following international peer-reviewed journal articles with the author of this thesis as first author:

Rietsch SHG, Quick HH, Orzada S.

Impact of different meander sizes on the RF transmit performance and coupling of microstrip line elements at 7 T.

Medical Physics 2015; 42(8): 4542–52

Rietsch SHG, Orzada S, Bitz AK, Gratz M, Ladd ME, Quick HH.

Parallel Transmit Capability of Various RF Transmit Elements and Arrays at 7T MRI.

Magnetic Resonance in Medicine 2018, 79(2):1116-1126

Rietsch SHG, Pfaffenrot V, Bitz AK, Orzada S, Lazik-palm A, Theysohn JM, Ladd ME, Quick HH, Kraff O.

An 8-channel transceiver 7-channel receive RF coil setup for high SNR ultrahigh-field MRI of the shoulder at 7T.

Medical Physics 2017, 44(12):6195-6208

Rietsch SHG, Orzada S, Maderwald S, Brunheim S, Philips BWJ, Scheenen TWJ, Ladd ME, Quick HH.

7T ultra-high field body MR imaging with an 8-channel transmit / 32-channel receive radiofrequency coil array.

Medical Physics 2018, 45(7):2978-2990

Chapter 1 Introduction

1.1 The history of magnetic resonance imaging

The initial steps towards today's medical imaging were made when Conrad Röntgen discovered the x-ray radiation in 1895. While this technique is still used especially for the depiction of bones, the invasive nature of the radiation and the reduced soft tissue contrast remain a problem. Fortunately, magnetic resonance imaging (MRI) is a well-suited alternative for modern radiologists. It is non-invasive, offers superb soft tissue contrast and allows for the assessment of brain function, spectroscopic information, the depiction of diffusion, blood circulation, heart movement and more.

From a physicist's point of view, MRI had its beginning with the discovery of the hyperfine structure in nuclei. This was explained by Wolfgang Pauli in 1924. In 1945, he was awarded with the Nobel Prize in physics.

In 1938, 14 years later, Isaac Rabi first described nuclear magnetic resonance (NMR) in molecular beams (1). He was rewarded with the Nobel Prize in 1944, just before his findings were further developed by Felix Bloch (2) and Edward Mills Purcell (3) in 1946. They independently accomplished NMR in liquids and solids which brought them the Nobel Prize in 1952. NMR was and is still performed to examine molecular structures using spectroscopy.

In 1950, Erwin L. Hahn realized that applying radio frequency (RF) pulses to a sample results in (Hahn) spin echoes (4). This approach is still utilized in today's spin echo sequences. Although often nominated, Hahn would never receive the Nobel Prize.

The transition of NMR towards medical imaging was initiated in 1971 by Raymond Damadian. In his work (5), he showed that "Spin echo nuclear magnetic

resonance measurements may be used as a method for discriminating between malignant tumors and normal tissue”.

In these times, information obtained with NMR was still unspecific with respect to location. This changed when in 1973 Paul Lauterbur published (6) first MR images acquired with a projection technique based on computer tomography. In 2003 he was awarded with the ‘Nobel Prize for Physiology or Medicine’.

The next step was initiated by Richard Ernst who, in 1975, realized that the Fourier Transform can be used to reconstruct images from k-space data (7). This technique is still used in MRI to this day. He received the Nobel Prize for chemistry in 1991.

Finally, the first human MR images were published in 1977 by Peter Mansfield (8). He performed proton imaging on a finger in vivo. This can be seen as the first proof of principle for human MRI which advanced significantly in the following decade. He received the Nobel Prize together with Paul Lauterbur in 2003.

In the 1980s the first MR systems were introduced for clinical use. Fueled by the broad utility of computers this was an emerging industry and innovative research field. The main magnetic B_0 field (precisely: magnetic flux density) increased in order to achieve higher signal-to-noise-ratio (SNR). Especially, the introduction of the first 1.5T by GE in 1984 was an important step. SNR increases more than linearly with field strength (9), thus higher B_0 improves imaging capabilities. Today 1.5 and 3T MRI systems are broadly used in the clinical environment.

In 1998 an 8T system was installed at Ohio State University. The first 7T MRI system was installed in 1999 at the University of Minnesota. In the following years slowly more research sites got involved in this technology until in 2016 about 60 ultrahigh-field (UHF) MRI systems with 7T field strength were installed. These systems were pure research systems which could not be used for clinical diagnoses. The main task was to find applications for which 7T could achieve an additional diagnostic benefit in human medical imaging. Just as these lines are written, the

manufacturer Siemens has obtained a 510k approval which allows radiologists to use 7T systems for diagnosis in very selected applications.

1.2 Physical principles of magnetic resonance imaging

The purpose of the following chapter is to give a compact overview of the theoretical background of MRI. The content is based on the established text books (10–12) and theses (13,14).

From spins to magnetization

The principles of MRI are based on quantum mechanical theory. One fundamental aspect of quantum mechanics is the quantization of physical properties like the angular momentum \vec{I} of protons and neutrons. This angular momentum \vec{I} is called spin and its quantization is twofold.

First, the absolute value of the spin is quantized:

$$|\vec{I}| = \hbar \sqrt{I(I+1)} \quad [1.1]$$

with the reduced Planck constant of $\hbar = 1.055 \cdot 10^{-34}$ Js. The permissible spin quantum numbers I are

$$I = 0, \frac{1}{2}, 1, \frac{3}{2}, \dots \quad [1.2]$$

Second, the z-component of the angular moment is quantized. If an external magnetic field along z-direction is applied, the component I_z is quantized by

$$I_z = m\hbar \quad [1.3]$$

with m being the magnetic quantum number which may take the values

$$m = -I, -I+1, \dots, I-1, I \quad [1.4]$$

The hydrogen nucleus ^1H with one proton can then be characterized by:

$$I = \frac{1}{2}, |\vec{I}| = \frac{\sqrt{3}}{2}\hbar, m = \pm \frac{1}{2}, I_z = \pm \frac{1}{2}\hbar \quad [1.5]$$

While this is the simplest example, other nuclei follow the same rules. Yet, according to the Pauli-principle, the spin of different neutrons and protons in a nucleus form pairs with antiparallel spin directions, because this minimizes the system's energy. Consequently, no angular momentum results for these pairs. This means for nuclei with an even number of protons and an even number of neutrons no net magnetization due to the spin results. All other nuclei in contrary have an intrinsic spin \vec{I} which results in a magnetic momentum $\vec{\mu}$

$$\vec{\mu} = \gamma \vec{I} \quad [1.6]$$

with γ being the nucleus-dependent gyromagnetic ratio. Hydrogen has a gyromagnetic ratio of $\gamma = 2\pi \cdot 42.58 \text{ MHz T}^{-1}$ which is the largest of all stable nuclei. In conjunction with the high natural abundance of hydrogen in tissue (about 66% of the body is water), hydrogen is the optimum nucleus for MRI since a high macroscopic magnetisation arises.

Following [1.5] the z-component of the magnetic momentum $\vec{\mu}$ of hydrogen in a magnetic field has two permissible values

$$\mu_z = \pm \frac{1}{2} \gamma \hbar \quad [1.7]$$

Which means that the z-component is aligned either parallel to the external magnetic field or antiparallel. These eigenstates have different energy levels

$$E = \pm \frac{1}{2} \gamma \hbar B_0 \quad [1.8]$$

and consequently, an energy difference of

$$\Delta E = -\gamma \hbar B_0 \quad [1.9]$$

arises between both eigenstates. Energy in form of radio frequency (RF) waves

$$E = \hbar \omega_0 \quad [1.10]$$

can be absorbed by the system if the resonance frequency ω_0 is used for transmission. This results into a change from the low energy to the high-energy eigenstate. The resonance frequency corresponds to the Larmor frequency

$$\omega_0 = \gamma B_0 \quad [1.11]$$

If an external field of $B_0 = 7$ T is applied, the Larmor frequency is

$$f_0 = \frac{\omega_0}{2\pi} \approx 297 \text{ MHz} \quad [1.12]$$

The two eigenstates furthermore correspond to a precession of the magnetic moment $\vec{\mu}$ around the axis of the external magnetic field. In general the magnetic moments within one sample all have different phases.

Utilization of the magnetic moment for MRI is only possible because of the intrinsic ambition for energy minimization. The occupation probability of the parallel state in an external magnetic field is higher since this is the lower energy level following the Boltzmann distribution. The sum of all N vectors $\vec{\mu}_i$ within a sample consequently results in a macroscopic equilibrium magnetization \vec{M}_0 parallel to the external magnetic field \vec{B}_0 :

$$\vec{M}_0 = \frac{1}{V} \sum_{i=1}^N \vec{\mu}_i = \frac{N}{V} \cdot \frac{\gamma^2 \hbar^2 \vec{B}_0}{4kT} \quad [1.13]$$

where $\frac{N}{V}$ is the sample's spin density, $k = 1.38 \cdot 10^{-23} \text{ JK}^{-1}$ the Boltzmann constant and T the absolute sample temperature. A high equilibrium magnetization is necessary to achieve a high signal-to-noise ratio (SNR) for MRI. All parts of [1.13] for a given subject are inalterable except for T and B_0 . Since cooling down a human subject is only possible to a limited extent, increasing B_0 is the only way to increase the net magnetization. This explains the constant drive towards even higher main magnetic fields in MRI.

Excitation and relaxation of a spin ensemble

While the spin itself is a quantum mechanical phenomena, for the description of MRI the net magnetization on a macroscopic scale (classical limit) is sufficient. The behavior of the magnetization \vec{M} can be described by the classical Euler equation of motion:

$$\frac{d}{dt}\vec{M}(t) = \vec{M}(t) \times \gamma\vec{B}(t) \quad [1.14]$$

This describes the precession of the magnetization \vec{M} around a magnetic field $\vec{B}(t)$. If \vec{M} and \vec{B} are aligned in parallel, like it is the case for the equilibrium magnetization \vec{M}_0 and the external magnetic field \vec{B}_0 , the cross product is zero and there is no time dependency of $\vec{M}(t)$. If however, the magnetization is tipped, a rotating magnetization vector will be generated in the transverse plane, which can generate an electromagnetic field in a suitably placed receiver coil.

A subject's equilibrium magnetization cannot simply be measured in MRI. Since the phase of all the spins within a sample is generally randomly distributed, also no transversal magnetization in the x-y-plane can be measured.

To change this, an external RF field \vec{B}_1 is applied using a transmit antenna. The frequency of \vec{B}_1 needs to be equal or close to the Larmor frequency and the direction of \vec{B}_1 has to be orthogonal to \vec{B}_0 . If \vec{B}_1 is used in 1.14, it becomes obvious that \vec{B}_1 also has to be orthogonal to \vec{M} for excitation. A (clockwise) circular polarized magnetic field \vec{B}_1 fulfills this requirement. As long as \vec{B}_1 is applied, the magnetization \vec{M} performs a precession around \vec{B}_1 in addition to the precession around \vec{B}_0 . This precession is characterized by ω_1 :

$$\omega_1 = \gamma|\vec{B}_1| \quad [1.15]$$

By adjusting the period of time for the excitation, the flip angle by which the magnetization \vec{M} is tilted can be determined:

$$\alpha = \omega_1 t_p \quad [1.16]$$

The signal which can be measured by a receive antenna (in general a conducting circuit e.g. loop, also called coil) which is oriented orthogonal to \vec{B}_0 is maximum if a 90° flip angle is achieved. After a 90° pulse, the full equilibrium magnetization has been tilted to form a transversal magnetization in the x-y-plane with all the spins being in phase. Consequently, their magnetization vectors add up and due to their precession around \vec{B}_0 a sinusoidal signal is induced in the coil following Faraday's law of induction. In general, a superposition of both \vec{B}_0 and \vec{B}_1 manipulates the magnetization \vec{M} during transmit. This manipulation and the return to the equilibrium magnetization are described by the Bloch equations in the specific directions:

$$\frac{d}{dt}M_x(t) = \left(\vec{M}(t) \times \gamma\vec{B}(t)\right)_x - \frac{M_x}{T_2} \quad [1.17]$$

$$\frac{d}{dt}M_y(t) = \left(\vec{M}(t) \times \gamma\vec{B}(t)\right)_y - \frac{M_y}{T_2} \quad [1.18]$$

$$\frac{d}{dt}M_z(t) = \left(\vec{M}(t) \times \gamma\vec{B}(t)\right)_z - \frac{M_0 - M_z}{T_1} \quad [1.19]$$

Here, the longitudinal relaxation time T_1 and the transversal relaxation time T_2 are tissue-dependent. This is the critical point for the generation of the MRI contrast. The recovery to the equilibrium state of $M_z(t)$ is described by T_1 while T_2 is a measure for the time during which the spins lose their phase coherence in the x-y-plane. This loss of phase coherence is exponential over time. Consequently, the amplitude of the measured signal, called free induction decay (FID), following a 90° pulse is exponentially damped.

In a real MRI experiment, local field inhomogeneity and varying susceptibility of the subject result in a locally depending Larmor frequency. As spins react to the

superposition of all magnetic fields in their environment, this leads to an accelerated deprivation of their phase coherence which is described by the T_2^* relaxation time ($T_2^* < T_2$).

Gradient encoding and image reconstruction

In order to gather information from specific local points within the subject, the signal needs to be spatially encoded. This is achieved by applying magnetic gradient fields which lead to a spatial dependency of the Larmor frequency:

$$\omega(\vec{r}, t) = \gamma B(\vec{r}, t) = \gamma (B_0 + \vec{G}(\vec{r}, t) \cdot \vec{r}) \quad [1.20]$$

MRI systems are capable of playing gradients in all three spatial dimensions:

$$\vec{G}(\vec{r}, t) = \frac{\partial \vec{B}}{\partial x} \vec{e}_x + \frac{\partial \vec{B}}{\partial y} \vec{e}_y + \frac{\partial \vec{B}}{\partial z} \vec{e}_z \quad [1.21]$$

Encoding a 2D image consists of three steps which are applied along the three orthogonal orientations:

- 1) Slice selection: During B_1 excitation a gradient e.g. in z-direction is switched on. Consequently, only spins in the slice that match the excitation frequency are excited. The slice thickness depends on the RF pulse bandwidth while the position depends on the carrier frequency. The slice orientation is adjustable at will.
- 2) Phase encoding: Switching on a gradient along y-direction after excitation results in different phases of the columns.
- 3) Frequency encoding: During measurement a readout gradient is applied along x-direction to encode additional information along that direction.

The results are gathered in a complex matrix called k-space. One line thereby represents one phase encoding step and the process has to be repeated until the

k-space is filled. Then, the 2D image is obtained by calculating the Fourier transform of the k-space. This allows to assign an intensity value to each pixel that corresponds to the transversal magnetization at that location at the time of measurement.

For 3D sequences the slice selection is replaced by an additional phase encoding in the slice direction. This takes longer but increases SNR. Image reconstruction is then possible using a 3D Fourier transform.

There are a variety of methods to modify the procedure. For example, only parts of the k-space are acquired (half-Fourier, every other line, etc.), the sampling is accomplished in a radial or spiral fashion and many more.

In general, the combination of excitation and gradient switching with a specific timing is called a pulse sequence. There are a variety of different sequence types for dedicated applications. Yet, two basic schemes can be differentiated: spin echo and gradient echo sequences.

Spin Echo

Since B_0 inhomogeneities leading to the T_2^* decay are locally fixed, the resulting dephasing of spins and the loss of the transverse magnetization can be reversed. The signal can be recovered using a spin echo as shown by Erwin Hahn (4).

The pulse sequence diagram of a spin echo sequence in Figure 1.1 shows 4 lines for the RF pulses (B_1 excitation) and the 3 gradient orientations.

A 90° pulse converts the equilibrium magnetization into a transversal magnetization. At the same time a slice selection gradient is played out. This ensures that only spins in a specific slice are excited. Applying the gradient also leads to dephasing of the spins along this direction. Consequently, the gradient needs to be switched in opposite direction to recover phase coherence.

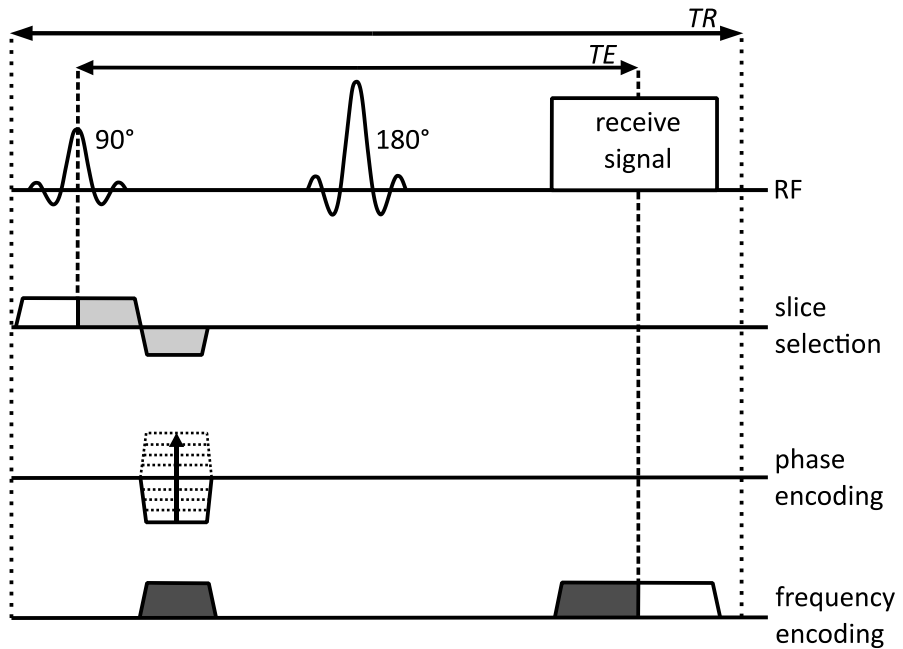


Figure 1.1: Timing of a spin echo sequence where a 90° excitation pulse is applied simultaneously with the slice selection gradient. Since the shaded part (above the horizontal axis) of the slice selection gradient leads to a dephasing within the slice, the gradient has to be played out with changed polarity after the 90° pulse to compensate for that. The 180° pulse generates a spin echo after the echo time TE has elapsed. Frequency encoding is performed during signal reception. Just like for the slice selection gradient, the frequency encoding gradient has to be played out simultaneously with the phase encoding to compensate for the dephasing. Due to the 180° pulse the polarity is identical with the frequency encoding gradient during reception. The whole procedure is repeated with varying phase encoding gradient amplitude with every repetition time TR .

After the 90° pulse the T_2^* decay leads to an FID. The spins lose their phase coherence due to varying Larmor frequencies. By playing out an 180° pulse after the time $TE/2$ has elapsed, the dephasing can be reversed since the spatially fixed field inhomogeneities now rephase the spins. This leads to a recovery signal (spin echo) after TE has elapsed.

For spatial localization the frequency encoding is used during signal reception when the echo is measured. Dephasing of the spins by this gradient is compensated by a gradient in the same direction before the 180° pulse.

The whole procedure is repeated for different phase encoding gradients after the time TR has elapsed.

Spin echo sequences are non-sensitive to T_2^* since this effect is cancelled. Image contrast can be primarily weighted towards T_2 . This depends on the user's choice for TR and TE . Other possibilities for contrast are T_1 and proton-density weighting.

Due to the 180° pulse, spin echo sequences are very robust against susceptibility and B_0 inhomogeneities which are locally fixed and consistent over time. Yet, the 180° pulse can be an obstacle at higher magnetic field strength due to the specific absorption rate (SAR) of RF energy in body tissue.

Gradient Echo

Another method to generate an echo without a 180° pulse is the gradient echo sequence. Instead of the 180° pulse, a gradient is used to refocus the spin ensemble and a gradient echo can consequently be measured.

This sequence type is comparably faster due to the reduced echo time. Also gradient echo sequences are less SAR intense while being more prone to susceptibility and B_0 inhomogeneity since the T_2^* dephasing is not compensated. Besides T_1 and proton-density weighting, gradient echo sequences allow T_2^* weighting.

The excitation pulse does not necessarily have to be a 90° pulse. By reducing the flip angle to achieve a specific flip angle called the Ernst Angle, the maximum signal-to-noise-ratio can be achieved. Reduced flip angles are also used in order to reduce SAR, generate dedicated contrasts or achieve a steady state in which recovery of

the magnetization and repeated excitation result in a steady state of the spin ensemble.

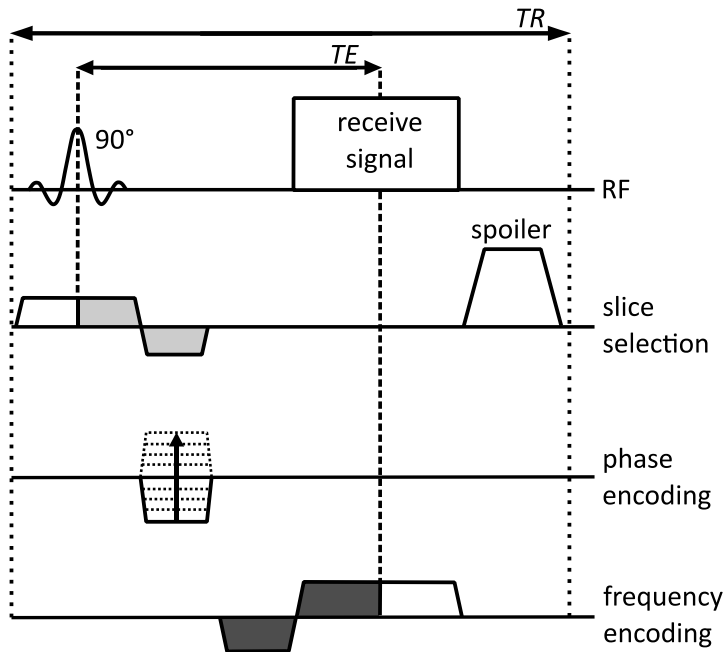


Figure 1.2: Timing of a gradient echo sequence. Compared to the spin echo sequence, no 180° refocusing pulse is used. Instead, a dephasing is achieved by the left part of the shaded frequency encoding gradient. Then the frequency encoding gradient is played out with changed polarity. At a specific point in time (after TE has elapsed), the dephasing which has been induced is fully compensated and a gradient echo can be measured. The shaded areas of the frequency encoding gradient below and above the horizontal axis are identical (identical time-amplitude-integral). A spoiler dephases remaining transversal magnetization before the next excitation.

Furthermore, both spin echo and gradient echo sequences can be accompanied by pulses for magnetization preparation, for example to saturate the fat signal. Single shot techniques with only one excitation can be used where the whole k-space is filled with multiple phase encoding echoes. Hybrids of both sequence types are possible and varieties for different applications have been developed for either

or combinations of both types. Detailed information can be found in dedicated text books (11).

Antennas for MRI

In general, MRI coils are antennas used for RF transmit (Tx) and/or reception (Rx). In clinical MRI systems a large-volume body RF coil surrounds the body of the patient. The body coil is a birdcage antenna primarily used for transmit and is integrated into the MRI system behind the covers of the patient tunnel. While it is possible to receive with the body RF coil as well, instead local receive coils (surface coils) are mostly used. To maximize SNR, these Rx-coils should surround the investigated body region tightly and seamlessly if possible. Loop elements are normally used as receive elements for clinical MRI (1.5T and 3T).

At higher field strength ($\geq 3T$), the short wavelength makes the application of body coils difficult. Here, local coils which are placed close to the subject are mostly used both for transmit and receive (transceiver coil). Yet, it is also possible to split the coil into a transmit-only and receive-only part, or into a transceiver and receive-only part.

To characterize the coil, it is convenient to separate the \vec{B}_1 field in two parts (15).

$$B_1^+ = \frac{B_{1x} + iB_{1y}}{2} \quad [1.22]$$

$$B_1^- = \frac{B_{1x} - iB_{1y}}{2} \quad [1.23]$$

Here, B_{1x} and B_{1y} describe the complex components of \vec{B}_1 in the x and y-plane. While B_1^+ represents the transmit field, B_1^- represents the receive field of an MR coil. Both quantities describe different aspects of a coil. High B_1^+ for a certain input power P means that the coil is very power efficient B_1^+/\sqrt{P} and short excitation pulses are possible. High B_1^- means that the coil is sensitive and can produce a high SNR.

Another important aspect of MRI coils is the SAR efficiency, which is the ratio of B_1^+ and the square root of the SAR (normally averaged over 10 g segments) in units of $[\frac{\mu T \sqrt{kg}}{\sqrt{W}}]$. In general coils should exhibit high B_1^+ with minimum SAR.

It should be noted that power on the transmit side lies in the area of 10 kW peak for 7T. In comparison, the voltage measured by preamps is in the range of nV. Furthermore, the dynamic range among the receive signals between the peak in the k-space center and thermal noise floor in the border regions is about 120 dB (16). This results in an enormous dynamic range of the MR system in general and of the receive chain in particular.

Every MRI image is influenced by noise. This noise has different sources. The two main sources are the molecular Brownian motion in the patient (white noise equally distributed among all frequencies) which inductively couples to the receiver coil, and the thermal noise in the RF receive chain. While measuring, thermal noise can only be reduced by minimizing the receiver bandwidth. To minimize the noise and maximize SNR, one aim of coil construction is to maximize the so called Q-ratio defined by $Q_{\text{unloaded}}/Q_{\text{loaded}}$. The Q-factor (quality factor) of a resonant structure can be measured with a network analyzer by dividing the resonant frequency by the 3 dB bandwidth for both unloaded and loaded condition. In this way, it is ensured that the coil works in the body noise dominated regime where the unavoidable sample noise dominates. Typically a Q-ratio of more than 2 is desirable for MR antennas.

Minor noise results from other RF circuitry and amplifiers, digitization noise and noise that comes from outside of the MRI system and passes the Faraday cage around the system.

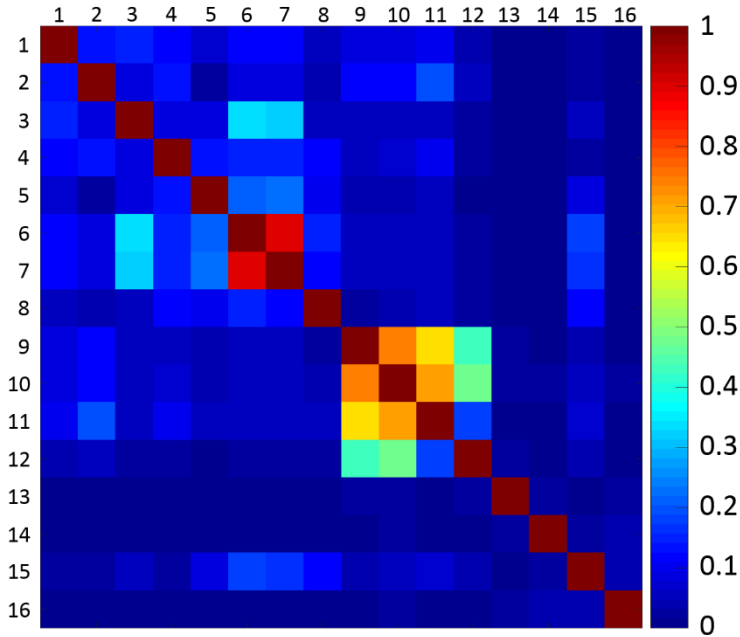


Figure 1.3: Magnitude of the noise correlation coefficient for a 16-channel Rx-only coil. All diagonal values are $r(i, i) = 1$ while off-diagonal elements have non-zero values. High correlation is visible between channel 6 and 7.

In order to investigate the crosstalk between channels, the noise correlation between individual coil channels can be measured. Therefore, one channel at a time is used for receive while it or all the other channels are unblanked in turn, without transmitting an RF pulse. This means that only noise is received by the current channel. The result is a complex noise matrix. One possible representation is the noise correlation coefficient between the ‘transmit’ and the receive channels. This gives a complex, symmetrical matrix with normalized diagonal. In general the

(Pearson) correlation coefficient r between the two random variables x and y is defined as (17):

$$r = \frac{1}{N-1} \sum_{i=1}^N \left(\frac{x_i - \mu_x}{\sigma_x} \right) \left(\frac{y_i - \mu_y}{\sigma_y} \right) \quad [1.24]$$

Here, each of the variables has N observations. μ_x and μ_y are the mean value of the data while σ_x and σ_y are the standard deviation. The correlation coefficient measures both strength and direction of the linear relationship of the variables, so in the context of noise, the more similar signal x (receiver channel) and y (transmit channel only transmitting noise) are the higher the correlation coefficient will be.

To assess the SNR of a coil, quantitative evaluations are rather unpractical for MRI. Often a relative SNR comparison between two coils is drawn by acquiring the same data under comparable circumstances with these two coils. Then the relative SNR maps can be compared by division. Consequently, the gain of e.g. a receive coil in comparison to a remote body coil can be evaluated.

SNR maps can be calculated for each pixel of an image by using the complex signals of the receive channels written in a vector \vec{b} and \vec{b}' is transposed. Then the residual sum of squares (RSS) image is calculated:

$$RSS = \sqrt{\vec{b} \circ \vec{b}'} \quad [1.25]$$

The optimum SNR combination OPT can be calculated by including the inverted noise correlation matrix N^{-1} :

$$OPT = \sqrt{\vec{b} \circ N^{-1} \circ \vec{b}'}$$

Parallel imaging

The most time consuming part of an MRI sequence is the phase encoding which has to be performed for each k-space line. If N encoding steps are necessary to fill

k-space along phase direction, and the TR lies in the range of a few milliseconds up to full T1 recovery of cerebrospinal fluid at about 3 s, the total acquisition time

$$TA = N \cdot TR \quad [1.26]$$

can easily be several minutes long. This is especially critical for 3D sequences with two phase encoding directions.

The solution is to reduce the number of phase encoding steps by skipping every R^{th} k-space line. This reduces TA by a factor of R . The spacing ΔG between the k-space lines in the phase encoding direction is inversely proportional to the field of view (FOV) in that direction. This means that by skipping k-space lines the image gets smaller.

As long as the whole object is covered no artifacts arise. Yet, if the FOV is smaller than the object, regions outside of the FOV appear as folding artifacts inside the image after reconstruction since the phase which is encoded by the gradients is identical for both positions.

By making use of the channel-dependent reception profiles B_1^- of a multi-channel receiver coil, the folding artifacts can be disentangled. Two methods are most important and widely used for that purpose. The first one is SENSE (18) (sensitivity encoding) which works in the image domain. The second method is called GRAPPA (19) (generalized autocalibrating partially parallel acquisitions) and works in k-space.

As often in MR physics, the reduction of time comes at cost of another quantity, in this case SNR. The SNR of accelerated images SNR_R with the reduction factor R is reduced compared to the unaccelerated SNR with $R = 1$.

$$SNR_R = \frac{SNR_1}{g\sqrt{R}} \quad [1.27]$$

Here, SNR_R is inversely proportional to the square root of R and the coil-dependent geometry factor $g(\vec{r}, R)$ which is depending both on the position \vec{r} and reduction

factor R . This means that noise, and consequently SNR, are not equally distributed in the image domain for accelerated imaging.

Even for a perfect coil the SNR in parallel imaging is reduced by R . Yet, a low g -factor is important in order to not reduce the SNR any further. Thus, one aim when constructing receive coils is to optimize the g -factor such that optimum parallel imaging capabilities are given. Assessment of the g -factor is an important point regarding coil evaluation. It should be noted, that the g -factor is not necessarily identical for SENSE and GRAPPA applications.

Ultrahigh field MRI at 7T

MRI using a main magnetic field of 7T or above is called ultrahigh-field MRI. The main advantage of higher field strength is the more than linear increase in SNR (9). This increased SNR can be used to increase spatial and/or temporal resolution (20). However, several obstacles arise as well. Inhomogeneities in the main magnetic field B_0 introduced by susceptibility effects at tissue boundaries especially between air and tissue, can lead to geometric distortions or intra-voxel dephasing (20).

MRI at 7T necessitates approximately 300 MHz radiofrequency (RF) fields for excitation of nuclear spin ensembles. This corresponds to a wavelength of 1 m in air. The wavelength in body tissue is reduced by the relative permittivity according to a factor of $\epsilon_r^{-0.5}$. The relative permittivity ϵ_r of tissue lies in the range of 45 to 75 for human tissue (21). This leads to a wavelength of about 13 cm inside of the body depending on the specific tissue type. Consequently, the wavelength is of the order of the dimensions of the investigated subject and the field inside the body can no longer be described by the quasistatic approximation. A transition to the electromagnetic field regime occurs and wave patterns occur due to constructive and deconstructive interferences of the RF (22). This is disadvantageous because it directly influences the flip angle distribution during transmission. Spin excitation is non-uniform which leads to signal voids, variable contrast and SNR (20). The

problem is exacerbated by the reduced penetration depth of RF into the body (23) which depends on the frequency and the material parameters.

In order to tackle the inhomogeneous B_1 excitation, several approaches like RF shimming (24,25), TIAMO (26,27) or transmit sense (28,29) have been presented. All these approaches are based on multi-transmit RF systems. This means that two or more transmit antennas are used which are driven by at least one or more RF power amplifiers. Modulators can be used to manipulate the amplitude and/or phase of the waveform generated by one exciter. Alternatively, separate chains of exciter, modulator and RF power amplifier can be used. The latter allows full parallel transmit (pTx) capability and maximum degrees of freedom (DOF) for RF manipulation.

Radiofrequency shimming

At 7T, constructive and destructive interference of RF fields can be manipulated when more than one antenna element is used for RF shimming. For each element the same RF pulse is played out. By applying a channel-dependent fixed amplitude and/or phase, represented by the complex weighting factor b_i , the resulting field $\vec{B}_{1,\text{sum}}^+(\vec{r})$ is a superposition of the channel-dependent fields $\vec{B}_{1,i}^+(\vec{r})$:

$$\vec{B}_{1,\text{sum}}^+(\vec{r}) = \sum_{i=1}^N b_i \cdot \vec{B}_{1,i}^+(\vec{r}) \quad [1.30]$$

To be more flexible, multi-channel transmit systems with modulators allow amplitude/phase adjustment for each channel.

In general, the aim of RF shimming is to achieve a homogeneous excitation within the region of interest or a maximum flip angle there within. Also, a compromise between both can be desirable. To achieve this, a target $\vec{B}_{1,\text{sum}}^+$ is defined and the system of equations, which is typically overdetermined, is solved using an optimization algorithm. While in the brain or extremities RF shimming is

sufficient for most applications at 7T, signal drop outs that occur for body imaging can be hard to remove. Due to the size of the subject, different shims simply shift the signal drop out to another location.

TIAMO

Time interleaved acquisition of modes (26,27) (TIAMO) is a method that combines two RF shims in one acquisition. In an 8-channel system, which are broadly employed in 7T MRI systems, for example, the circular polarized (CP+) mode with 45° phase increment between the channels and the CP2+ mode with 90° phase increment can be used.

Using short time-averaging, every other k-space line of a sequence is acquired twice with two alternating shim settings. An alternative is to acquire the full k-space with the first shim setting and then again acquire the k-space with the second shim setting. Both measurements are subsequently reconstructed in a combined reconstruction. Mathematically this corresponds to a measurement with a doubled number of receive elements.

Acquiring every line twice doubles the scan time. This can be partly compensated by using higher acceleration factors which is possible due to the increased number of virtual receive elements. With this technique, it is possible to homogenize the image and get rid of signal voids.

Another advantage can be that using two RF shims results in a total SAR that is the sum of two spatially different distributions (30). This can lead to reduced time-averaged RF deposition compared to a single RF shim.

Transmit Sense and Parallel Transmit

Multi-channel systems with full parallel transmit (pTx) capability allow to play out independent waveforms with each channel. Mathematically, this means that the complex weighting factors in [1.28] vary over time which leads to increased flexibility regarding the B_1 manipulation.

If in addition, varying gradient waveforms are played out, three additional degrees of freedom can be used for manipulation. This approach is called transmit sense (28,29).

These advanced methods also allow to exclusively excite a dedicated region of interest in the subject (zoomed imaging). This can be advantageous if only this region of interest is important for the diagnostic question. Furthermore, no negative impact of the surrounding regions is to be expected which, for example, allows free-breathing measurements without triggering.

While in theory this allows for optimum imaging results, only few practical implementations have been published so far. This is due to the high complexity of calculations (time consuming), expensive hardware and accurate knowledge of the B_1 and B_0 distributions that are necessary.

Specific Absorption Rate

Time-varying magnetic fields used for RF excitation are accompanied by time-varying electric fields according to Maxwell's equations. Due to the conductivity of tissue, field energy is dissipated in the tissue which leads to a temperature rise comparable to the principle of a microwave. This heat contribution due to absorbed RF fields is quantified by the specific absorption rate (SAR). In order to protect the subject from tissue damage by RF fields, limits set by the International Electrotechnical Commission (IEC) in the guideline IEC 60601-2-33 are not to be exceeded. These guidelines include limits for maximum tissue temperature, body

core temperature, and body core temperature rise. Furthermore, limits for global and local SAR are given for an averaging time of 6 min. Global SAR supervision can be sufficient for birdcage coils at 1.5T and 3T since it is expected that the quasi-static approximation is valid. Also a 'history of safe use' seems to justify global SAR supervision for these clinical systems (21). Yet, it has been shown that birdcage body coils could be a safety hazard even in 1.5T systems (31,32). As soon as 7T MRI is performed, the short wavelength in the body and parallel transmit approaches necessitate the use of multi-channel coils and a local SAR supervision for which the IEC guidelines provide different limits. Also, the guidelines provide three operating modes (normal mode, 1st level controlled mode, 2nd level controlled mode) with increasing limits both for temperature and SAR. The maximum local SAR limit for the trunk is for example 10 W/kg in the normal operating mode. Values for SAR in a tissue volume ΔV can be described by (21):

$$SAR = \frac{1}{2\Delta V} \iiint_{\Delta V} \frac{\sigma(\vec{r})}{\rho(\vec{r})} |\vec{E}(\vec{r})|^2 dV \quad [1.28]$$

which suggests that SAR [W/kg] is proportional to the square of the absolute value of the electric field $\vec{E}(\vec{r})$, to the tissue conductivity $\sigma(\vec{r})$ and to the reciprocal of the tissue density $\rho(\vec{r})$. Since both conductivity and tissue density vary for each tissue type, the SAR does also vary depending on the spatial location. Local SAR values also depend on the tissue volume ΔV which does normally correspond to averaged tissue masses of e.g. 10 g (21). Corresponding values are consequently described as SAR_{10g} values. High flip angles and RF pulse bandwidth also lead to increased SAR (11). This explains why large flip angles like the 180° pulse of spin echo sequences are disadvantageous especially at 7T and above. Consequently, gradient echo sequences with low bandwidth are most favorable with respect to SAR. For many applications at 7T, local SAR is the limiting factor.

RF simulations and coil validation

For MRI measurements no direct measurement of the SAR is possible. Consequently, the investigator needs to rely on RF field simulations that use realistic models for the human body (33). This is especially important for MRI at 7T where the aforementioned short wavelength and the use of multi-channel transmit approaches comes on top of the inhomogeneous SAR distribution due to conductivity differences. Local SAR supervision following the IEC guidelines mentioned above is necessary. The following section gives a brief summary of simulations and coil validation. More detailed information about simulation can be found in the literature (34).

The behavior of electric \vec{E} and magnetic \vec{H} fields which are both changing in time and space is described by the Maxwell equations (34). These are given here in differential form.

Ampère's law:

$$\nabla \times \vec{H} = \vec{J} + \frac{\partial \vec{D}}{\partial t} \quad [1.31]$$

Faraday's law:

$$\nabla \times \vec{E} = -\frac{\partial \vec{B}}{\partial t} \quad [1.32]$$

Gauss's law:

$$\nabla \cdot \vec{D} = \rho \quad [1.33]$$

Gauss's law for magnetism:

$$\nabla \cdot \vec{B} = 0 \quad [1.34]$$

Here, \vec{J} is the current density, \vec{D} is the electric displacement, ρ is the electric charge density, t represents the time and \vec{B} is the magnetic flux density. The main

magnetic field B_0 in MRI is often misleadingly called magnetic field while it is actually a magnetic flux density.

Furthermore, the following relations are valid :

$$\vec{B} = \mu \vec{H} \quad [1.35]$$

$$\vec{D} = \epsilon \vec{E} \quad [1.36]$$

$$\vec{J} = \sigma \vec{E} \quad [1.36]$$

These connect magnetic flux and field via the magnetic permeability μ , the electric displacement and field via the electric permittivity ϵ , and the current density via the conductivity σ and the electric field.

Following the foregoing equations, in general, a specific current distribution, e.g. on the conductor of a transmit coil, results in a specific field distribution. Yet, this field distribution can only be calculated analytically for relatively simple geometries. Since in MRI, both conducting structures of the coil and the tissue distribution in the human subjects (δ, μ and ϵ) are complicated, an analytical calculation of an RF coil's behavior is mostly not possible.

Instead, computational RF simulations are performed. As the problem as a whole cannot be solved, the spatial domain is separated into smaller subdomains (cells) for which discretized Maxwell's equations can be solved numerically. This discretization allows for efficient handling by computers but it also introduces pitfalls as numerical dispersion (34) and stability issues (34,35).

The simulation procedure can be performed in the time domain or in the frequency domain. Time domain methods are for example the finite-difference time domain (FDTD) and the finite integration technique (FIT). Frequency domain methods are for example the finite element method (FEM) or the method of moments (MoM). All methods are based on field components or potentials for each cell. For all methods, a trade-off between simulation time, accuracy and size of the

domain is necessary. The resolution must be fine enough to obtain a desired accuracy of the simulation (21).

In FDTD, a uniform Cartesian grid is applied where the simulation domain is 'meshed'. The grid has to be fine enough to model sharp variations in the structure like corners. In addition, the cell size has to be small compared to the RF wavelength λ to limit the resulting numerical error. It is recommended to use a maximum cell size which is less than $1/20$ of the shortest occurring wavelength (21). The size of the simulation domain is only limited by the computational power of the simulation system. The simulation starts by exciting the system with a specific signal and calculating its response. Therefore, a leap frog approach is used, where electric and magnetic field components for each cell are alternately calculated on a staggered grid (E- and H-field grids are shifted by $\frac{1}{2}$ of the grid size) for each time step (34).

The main drawback of FDTD is the restriction to structured grids (staircase problem). This makes the method easily applicable but subtle structures necessitate high resolution and, consequently, small cells. Due to the stability criterion small time steps have to be used (34). For very resonant structures with a high quality factor, the energy inside the system only slowly decreases. Thus, in combination with small time steps, this results in a long computation time. The simulation time must be chosen long enough to satisfy a steady state energy criterion (e.g. remaining system energy of 10^{-8} compared to the input energy). Applying the Fourier transformation yields the frequency spectrum of the simulated coil. Consequently, time-domain is well suited for broadband applications.

The finite integration technique (FIT) is also time-domain based (36). It is computationally equivalent to the FDTD method using a Cartesian grid and the leapfrog time integration scheme (37). However, FIT is derived from Maxwell equations in integral form.

For multi-channel RF coils several excitation ports with an internal resistance of 50 Ohm can be simulated (21). The simulation can then be combined with a circuit network simulation. This allows the calculation of different RF shims by weighted superposition without re-simulating (21).

Results of the simulation can be displayed to investigate a coil's properties like coupling behavior, E -field, H -field, B -field, B_1^+ -field, B_1^+ -efficiency, SAR-efficiency and SAR distribution for a given input power. With respect to patient safety, the SAR_{10g} matrices (21) can be used to calculate the local tissue RF load.

Depending on the specific coil and simulation domain, the number of resulting SAR_{10g} matrices (21) can be in the order of 10^6 . This number makes a real-time SAR supervision of an MRI system unpractical if not impossible. To tackle this problem, a method called virtual observation points (VOP) has been presented (38). Therefore, an overestimation of the actual SAR values (e.g. 10%) allows for a clustering of the SAR_{10g} matrices. Within one cluster, the SAR values are comparable for a certain excitation vector which contains amplitude and phase for each transmit channel (21). The dominant SAR matrix of a cluster (called VOP) yields the maximum SAR for all excitation vectors. Consequently, it is sufficient to calculate the SAR for this specific VOP instead of calculating all SAR values for the cluster. The number VOPs can be much smaller (e.g. 100 VOPs) than the number of SAR_{10g} matrices (38). The higher the chosen maximum overestimation, the smaller the number of VOPs.

In order to validate the RF coil model used for simulation, field measurements can be performed in a homogenous phantom with simple geometry (39) for comparison. If the coil model is valid, simulations with realistic body models (33) yield results for the SAR_{10g} matrices which can be used for the calculation of VOPs. By measuring amplitude and phase during the acquisition on the MR system, SAR values can be calculated (21) and the measurement can be stopped if the limits would be exceeded.

1.3 Objective of this thesis

The aim of this thesis is to develop and evaluate different RF coil elements and arrays for 7T MR imaging. Various multichannel transmit/receive RF arrays have been simulated, constructed, and applied in different diagnostic applications of 7T UHF MRI on humans.

In chapter 2 the coupling behavior between neighboring RF coil elements is investigated. Starting with a micro stripline element, meander structures are introduced at both ends. This changes the coupling between the elements in an array configuration. It can be shown that for this setup, an optimum range of meander sizes can be used to minimize the coupling between two neighboring elements. Efforts are made to investigate the reason for this changing coupling behavior. Changes in power transferred between different parts of the elements, represented by the Pointing vector, can be identified to describe this behavior. Changing the distance between the elements or the distance to the subject slightly shifts the optimum size of the meanders depending on the exact configuration. Four different pairs of elements were constructed to compare the coupling results from the simulations with the coupling measured between real elements in a comparable measurement setup.

The focus of chapter 3 is on remote RF coil arrays for 7T body imaging. Here 4 and 8-channel RF coil arrays which are mounted on the MR system's bore liner are simulated using a realistic human body model as coil loading. Altogether, 22 configurations are compared using four different designs. Compared to what was found in chapter 2 for close-fitting coil elements, enhanced coupling can be demonstrated for all remote coil configurations. Furthermore, a non-negligible part of the power is radiated towards both ends of the bore liner depending on the RF shim setting. Radiation is one of the reasons why remote coils show comparably low power efficiency. In the direct comparison between the 22 configurations, 8 λ over two dipoles with shield are most favorable.

Chapter 4 presents an 8-channel transmit 7-channel receive RF coil setup for 7T shoulder MRI. Safe use of the coil setup is demonstrated by comparing simulated and measured fields. Besides the characterization on the bench, 7T MRI of the shoulder is shown in volunteers. The power efficiency of the transmit coil provides a maximum B_1^+ of 19 μ T when the hardware power limits of the 8-channel system are exploited. This allows for promising images with good quality and sub-millimeter spatial resolution.

In the shoulder, an RF shim using 8 transmit channels is sufficient for fairly homogeneous images. Chapter 5 investigates MR body imaging at 7T. Here, TIAMO is used for image homogenization in transversal orientation. The focus of the chapter is on the construction and evaluation of an 8-channel transmit 32-channel receive RF body array for 7T. This coil consists of 8-transceiver micro stripline elements with meanders and 24-receive only loops. The coil is compared to an 8-channel transceiver coil of comparable geometry. As can be shown, the additional receive-only loops provide about 33% more SNR even in the subject's center as well as enhanced acceleration capabilities. Safe use was again demonstrated by field measurements which are compared to the simulated equivalent of the setup. High quality images in the heart, abdomen and pelvis of volunteers can be achieved when using this coil.

Chapters 2-5 have been published in peer-reviewed journals and are formatted accordingly.

The sixth and final chapter gives a brief summary and discussion of the presented work.

References

1. Rabi II, Zacharias JR, Millman S, Kusch P. A New Method of Measuring Nuclear Magnetic Moment. *Phys Rev* 1938;53(4):318.
2. Bloch F, Hansen WW, Packard M. Nuclear Induction. *Phys Rev* 1946;69:127.
3. Purcell EM, Torrey HC, Pound R V. Resonance Absorption by Nuclear Magnetic Moments in a Solid. *Phys Rev* 1946;69:37.
4. Hahn EL. Spin Echoes. *Phys Rev* 1950;80:580.
5. Damadian R. Tumor Detection by Nuclear Magnetic Resonance. *Science* (80-) 1971;171(3976):1151–3.
6. Lauterbur PC. Image Formation by Induced Local Interactions: Examples Employing Nuclear Magnetic Resonance. *Nature* 1973;242:190–1.
7. Kumar A, Welte D, Ernst RR. NMR Fourier zeugmatography. *J Magn Reson* 1975;18:69–83.
8. Mansfield BP, Sc B, Ph D, Sc AAMB, Ph D. Medical imaging by NMR. 1977;50:188–94.
9. Pohmann R, Speck O, Scheffler K. Signal-to-Noise Ratio and MR Tissue Parameters in Human Brain Imaging at 3, 7, and 9.4 Tesla Using Current Receive Coil Arrays. *Magn Reson Med* 2016;75(2):1–9.
10. Haacke EM, Brown RW, Thompson MR, Vankatesan R. Magnetic Resonance Imaging - Physical Principles and Sequence Design. John Wiley

- & Sons, Inc.; 1999.
11. Bernstein M, King K, Zhou X. Handbook of MRI Pulse Sequences. Elsevier Academic Press; 2004.
 12. Reiser MF, Semmler W, Hricak H. Magnetic Resonance Tomography. Springer-Verlag Berlin Heidelberg; 2008.
 13. Orzada S. New Excitation Concepts for Ultra-High-Field Human MRI. PhD thesis, ISBN: 978-3-00-041249-3. 2012.
 14. Johst S. Acquisition Methods for 7 Tesla MRI from Head to Toe. PhD thesis, ISBN: 978-3-00-047676-1. 2014.
 15. Hoult DI. The Principle of Reciprocity in Signal Strength Calculations - A Mathematical Guide. Concepts Magn Reson 2000;12(4):173–87.
 16. Behin R, Bishop J, Henkelman RM. Dynamic range requirements for MRI. Concepts Magn Reson Part B Magn Reson Eng 2005;26(1):28–35.
 17. Press WH, Teukolsky SA, Vetterling WT, Flannery BP. Numerical Recipes in C - The Art of Scientific Computing. Second Edi. Cambridge University Press; 1992.
 18. Pruessmann KP, Weiger M, Scheidegger MB, Boesiger P. SENSE: sensitivity encoding for fast MRI. Magn Reson Med 1999;42(5):952–62.
 19. Griswold MA, Jakob PM, Heidemann RM, Nittka M, Jellus V, Wang J, Kiefer B, Haase A. Generalized autocalibrating partially parallel acquisitions (GRAPPA). Magn Reson Med 2002;47(6):1202–10.

20. Truong T, Chakeres DW, Beversdorf DQ, Scharre DW, Schmalbrock P. Effects of static and radiofrequency magnetic field inhomogeneity in ultra-high field magnetic resonance imaging. 2006;24:103–12.
21. Fiedler TM, Ladd ME, Bitz AK. SAR Simulations & Safety. Neuroimage 2018;168(March 2017):33–58.
22. Van de Moortele PF, Akgun C, Adriany G, Moeller S, Ritter J, Collins CM, Smith MB, Vaughan JT, Ugurbil K. B1 Destructive Interferences and Spatial Phase Patterns at 7 T with a Head Transceiver Array Coil. 2005;1518:1503–18.
23. Vaughan JT, Garwood M, Collins CM, Liu W, Delabarre L, Adriany G, Andersen P, Merkle H, Goebel R, Smith MB, et al. 7T vs. 4T: RF power, homogeneity, and signal-to-noise comparison in head images. Magn Reson Med 2001;46(1):24–30.
24. Collins CM, Liu W, Swift BJ, Smith MB. Combination of optimized transmit arrays and some receive array reconstruction methods can yield homogeneous images at very high frequencies. Magn Reson Med 2005;54(6):1327–32.
25. Mao W, Smith MB, Collins CM. Exploring the limits of RF shimming for high-field MRI of the human head. Magn Reson Med 2006;56(4):918–22.
26. Orzada S, Maderwald S, Poser BA, Bitz AK, Quick HH, Ladd ME. RF excitation using time interleaved acquisition of modes (TIAMO) to address B1 inhomogeneity in high-field MRI. Magn Reson Med 2010;64(2):327–33.
27. Orzada S, Johst S, Maderwald S, Bitz AK, Solbach K, Ladd ME. Mitigation of

- B1(+) inhomogeneity on single-channel transmit systems with TIAMO. *Magn Reson Med* 2013;70(1):290–4.
28. Katscher U, Börnert P, Leussler C, van den Brink JS. Transmit SENSE. *Magn Reson Med* 2003;49(1):144–50.
 29. Grissom W, Yip C, Zhang Z, Stenger VA, Fessler JA, Noll DC. Spatial domain method for the design of RF pulses in multicoil parallel excitation. *Magn Reson Med* 2006;56(3):620–9.
 30. Orzada S, Maderwald S, Poser BA, Johst S, Kannengiesser S, Ladd ME, Bitz AK. Time-interleaved acquisition of modes: an analysis of SAR and image contrast implications. *Magn Reson Med* 2012;67(4):1033–41.
 31. Murbach M, Cabot E, Neufeld E, Gosselin MC, Christ A, Pruessmann KP, Kuster N. Local SAR enhancements in anatomically correct children and adult models as a function of position within 1.5 T MR body coil. *Prog Biophys Mol Biol Elsevier Ltd*; 2011;107(3):428–33.
 32. Murbach M, Neufeld E, Capstick M, Kainz W, Brunner DO, Samaras T, Pruessmann KP, Kuster N. Thermal tissue damage model analyzed for different whole-body SAR and scan durations for standard MR body coils. *Magn Reson Med* 2014;71(1):421–31.
 33. Christ A, Kainz W, Hahn EG, Honegger K, Zefferer M, Neufeld E, Rascher W, Janka R, Bautz W, Chen J, et al. The Virtual Family--development of surface-based anatomical models of two adults and two children for dosimetric simulations. *Phys Med Biol* 2010;55(2):N23–38.
 34. Rylander T, Ingelström P, Bondeson A. Computational Electromagnetics.

Second Edi. Springer; 2013.

35. Courant R, Friedrichs K, Lewy H. Ueber die partiellen Differenzengleichungen der mathematischen Physik". Math Ann 1928;100(1):32–74.
36. Weiland T. A discretization method for the solution of Maxwell's equations for six-component Fields. Electron Commun AEUE 1977;31(3):116–20.
37. Schuhmann R, Weiland T. Recent Advances in Finite Integration Technique for High Frequency Applications. Proc Sci Comput Electr Eng 2002;
38. Eichfelder G, Gebhardt M. Local specific absorption rate control for parallel transmission by virtual observation points. Magn Reson Med 2011;66(5):1468–76.
39. Bitz AK, Kraff O, Orzada S, Maderwald S, Brote I, Johst S, Ladd ME. Assessment of RF Safety of Transmit Coils at 7 Tesla by Experimental and Numerical Procedures. Proc Intl Soc MRM 19 2011. p. 490.

Chapter 2 Impact of different meander sizes on the RF transmit performance and coupling of microstrip line elements at 7 T*

Purpose

In this work the transmit performance and inter element coupling characteristics of radiofrequency (RF) antenna microstrip line elements are examined in simulations and measurements.

Methods

The initial point of the simulations is a microstrip line element loaded with a phantom. Meander structures are then introduced at the end of the element. The size of the meanders is increased in fixed steps and the magnetic field is optimized. In continuative simulations the coupling between identical elements is evaluated for different element spacing and loading conditions. Verification of the simulation results is accomplished in measurements of the coupling between two identical elements for four different meander sizes. Image acquisition on a 7 T MRI system provides qualitative and quantitative comparison to confirm the simulation results.

Results

Simulations point out an optimum range of meander sizes concerning coupling in all chosen geometric setups. Coupling measurement results are in good agreement with the simulations. Qualitative and quantitative comparisons of the acquired MRI images substantiate the coupling results.

Conclusion

The coupling between coil elements in RF antenna arrays consisting of the investigated element types can be optimized under consideration of the central magnetic field strength or efficiency depending on the desired application.

*published as: Rietsch SHG, Quick HH, Orzada S. Impact of different meander sizes on the RF transmit performance and coupling of microstrip line elements at 7 T. Medical Physics 2015; 42(8): 4542–52

2.1 Introduction

Increasing the static magnetic field strength in magnetic resonance imaging (MRI) leads to higher signal-to-noise ratio (1–3). At ultra-high field with a static magnetic field strength of 7 T and above, higher Larmor frequencies and a reduced wavelength in the object under examination lead to wave effects and inhomogeneities in the radio frequency (RF) transmit field used to excite the spins (1). Additionally, reduced penetration depth and constraints in specific absorption rate impede ultra-high field MRI (4,5). Many technical approaches amongst others for example RF-shimming (6,7), Transmit SENSE (8,9) and TIAMO (10) have been developed to tackle these problems. Most of these techniques require multiple RF transmit elements with distinct transmit patterns. Furthermore, low coupling between the elements is favorable. This is necessary to optimize transmit power transfer to the object under investigation since the RF power is meant to excite the spins in the sample and should not be received by adjacent RF elements. Also, high coupling between transmit elements reduces the effective degrees of freedom when using multichannel transmit methods. Multichannel transmit/receive arrays have successfully been incorporated and evaluated in a broad variety of applications. Possible basic building blocks of those RF transmit/receive arrays can be loops (11–13), ceramic resonators (14), microstrip lines (MSL) (15–18), dipole antennas (19) or meander elements (ME) (20,21). Meander elements are MSL with meander structures located at both ends (Figure 2.1a). These meander structures increase the electrical length of the ME and consequently show enhanced imaging performance as well as low coupling to adjacent antenna elements compared to MSL (20). While the imaging capabilities of ME have been demonstrated in a wide area of applications (21–25), the impact of changing the meander length, especially concerning the low coupling, has only been investigated in conference contributions (20,26) so far.

This work provides a more in-depth study on the impact of changing meander size on RF transmit performance and on the coupling between adjacent elements.

MSL elements and ME with increasing meander size have been modeled in finite difference time domain simulations. At first, a single element loaded by a phantom is modeled to analyze and optimize the magnetic field distribution. In a second step, an identical element is located adjacent to the first one for S-parameter calculation. Investigations include variation in distance between the elements as well as variation in distance to the loading phantom. Four different pairs of elements were constructed on the basis of the simulations for verification of the coupling in the selected geometrical setups. The observations are furthermore inspected in 7 T MRI phantom measurements to verify the simulated coupling levels.

2.2 Methods

Modelling and Simulation

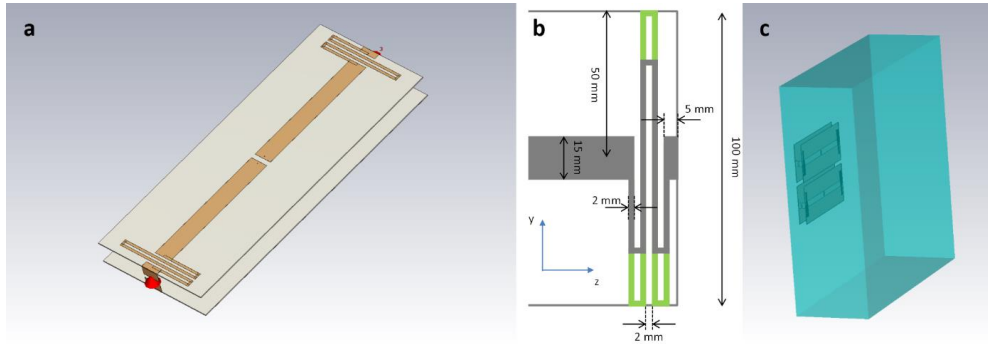


Figure 2.1: a) Microstrip line element with meanders modeled in the simulation software. The conducting structure on the top substrate and the ground plane on the bottom substrate are connected by thin wires in the center and by the end capacitors modeled as ports at both ends. b) Dimensions of the meander structure which is located at both ends of the element in z-direction on the top substrate. c) In all simulations the elements are loaded with the same rectangular phantom consisting of tissue simulating liquid. To examine the coupling an identical element is placed next to the first one in different geometric setups.

Modelling, finite-difference time-domain simulations and post processing is done in CST Microwave Studio (CST AG, Darmstadt, Germany). All modeled

elements (Figure 2.1a) feature identical outer dimensions. Both the top plane and the ground plane (Rogers 4003C carrier substrate, $\epsilon_r = 3.35$, $\tan\delta_{el} = 0.0027$, $\rho = 1790 \text{ kg m}^{-3}$) have a length of 250 mm in z-direction, a width of 100 mm in y-direction, a thickness of 0.8 mm and a 35 μm conductive cladding. Between the ground plane and the top substrate a distance of 18.4 mm is filled with air as dielectric and 3.5 mm gaps for capacitors are symmetrically added on both ends. The simulation domain has a size of 900 mm in z-, 900 mm in y- and 550 mm in x-direction allowing for a distance of at least 150 mm to the ideally absorbing boundary in all directions. On the top substrate meander structures are located at both ends in z-direction (Figure 2.1b). Close to these meander structures the meshing is refined to 0.5 mm isotropic in all simulations performed. The cladding of the ground plane as well as the top plane (meander structures and strip line) and the wires connecting both are modeled as perfect electric conductors. Central feeding is placed on the bottom substrate and simulated in a network co-simulation using a $\lambda/2$ balun (length = 330 mm, attenuation = 0.3 dB m^{-1}) and a matching network (15) with two parallel capacitors and one series capacitor modeled as RF ports. Identical capacitors at both ends of the element (C_{end}) are also modeled as RF ports (Figure 2.1a) to tune the current distribution on the conductor in the post processing. A rectangular phantom (dimensions: 600 mm in z-, 600 mm in y- and 200 mm in x-direction) consisting of tissue simulating liquid ($\epsilon_r = 45.3$, $\sigma = 0.87 \text{ S m}^{-1}$, $\rho = 1210 \text{ kg m}^{-3}$) is placed 30 mm above the element in x-direction as load (Figure 2.1c). Starting with a simple MSL (meander size = 0), the meander size is increased in steps of 2.5 mm until at 50 mm the whole size in y-direction (100 mm) is covered (green in Figure 2.1b).

Post Processing

Changes on the serial and on the two parallel capacitors in the co-simulation are only influencing tuning and matching. By changing C_{end} on both ports located at the

ends of the element, additionally the current distribution in the conducting parts of the top plane can be controlled. In order to determine the best choice for C_{end} for each meander size, a central line plot along the z-direction 30 mm inside the phantom is repeatedly evaluated in a post processing step following the simulation. For different values of C_{end} the single element is tuned and matched by variation of the parallel and matching capacitors to allow for a reflection factor of better than -20.00dB at a center frequency of 297 MHz. The optimum value for C_{end} provides maximum central magnetic field strength 30 mm inside the phantom and is consequently used in all further simulations including elements of the corresponding size. To characterize the safety performance, also the specific absorption rate was evaluated for each element. Specifically the specific absorption rate (SAR) averaged over 10 g ($\text{SAR}_{10\text{g}}$) was calculated (averaging method: IEEE/IEC 62704-1) for all elements and the maximum ($\text{Max SAR}_{10\text{g}}$) was used to evaluate the SAR efficiency.

Field Distribution

Subsequent to the optimization of C_{end} for each meander size in the post processing, the resulting fields were examined. For this purpose, the distributions of both H- and E-field magnitudes were calculated in the z-y-plane of the top substrate. This was performed for single elements of each meander size. To examine the impact of the meander structures simulation templates for a MSL and ME of the sizes 32.5 mm and 50 mm were duplicated. At the positions of the meander structures face ports were introduced instead. After simulation the elements could be tuned and matched by inserting an inductance at each face port in the co-simulation. Then, the fields of these microstrips with end capacitors of the corresponding meander simulations could be compared to the original simulations. Comparability was ensured by using equal input power of 0.5 W for all elements in all examinations. The impact of changing loading conditions was examined in

additional simulations by increasing the distance to the loading phantom to $p = 60$ mm for a MSL element, a 32.5 mm ME and a 50 mm ME.

Coupling in Simulations

For each single meander size the coupling between two neighboring elements was evaluated. If not indicated otherwise, coupling always describes the inter element coupling between transmit elements in this paper. In new simulations an identical element, with the same optimized capacitors C_{end} from the post processing, is placed next to the first one in y-direction so that there is a distance d between the edges of the top planes. By variation of d , the impact of changing spacing between the elements ($d = 10$ mm, $d = 30$ mm, $d = 50$ mm, $d = 100$ mm) on the coupling could be investigated. To evaluate different loading conditions, two further simulation runs were executed for all meander sizes in which the distance p to the phantom was increased to $p = 60$ mm while the spacing between the elements was $d = 10$ mm in the first run and $d = 100$ mm in the second. As previously done for the examination of the field distributions, simulations for pairs of MSL elements, ME with 32.5 mm and ME with 50 mm were performed for $d = 10$ mm and $p = 30$ mm with the only difference that face ports were introduced instead of the meander structures. In the co-simulation an inductance was placed at each face port to achieve tuning to 297 MHz and matching of -20 dB. The coupling between the elements could then be quantified by the S_{12} values.

Coupling Measurements

To verify the simulation results two MSL elements and three pairs of ME with the meander sizes of 27.5 mm, 32.5 mm and 50 mm where constructed according to their simulated model featuring the corresponding values for C_{end} . All elements were tuned to 297 MHz and matched to achieve a reflection factor of at least

$S_{11} = -20$ dB on a two channel network analyzer (Agilent Technologies, Santa Clara, CA, USA). Loading conditions were realized by a rectangular phantom (Figure 2.2) filled with 40 liters of distilled water (37.46 % of the total mass), sugar (56.69 % of the total mass) to control the permittivity and salt (5.85 % of the total mass) to achieve the same conductivity as used in the simulations. Using the network analyzer and a dielectric probe kit both conductivity and permittivity were measured in two time interleaved experiments. The coupling between identical neighboring RF elements was evaluated for a distance of $p = 30$ mm to the phantom and an inter element spacing of $d = 10$ mm, $d = 30$ mm and $d = 100$ mm. Then the distance to the phantom was increased to $p = 60$ mm and the coupling was evaluated for $d = 10$ mm and $d = 100$ mm between all identical elements. Positioning aids for the elements were constructed of thin polycarbonate plates and located directly below the center of the elements to minimize the influence on the field distribution. To quantify the impact of the positioning aids an additional simulation was performed and the resulting central line plot along the z-direction 30 mm inside the phantom was compared to the original simulation without positioning aids.



Figure 2.2: Setup for measurements of coupling between the elements using a rectangular phantom filled with tissue simulating liquid. Two identical transmit elements are located on positioning aids in the same geometrical setup as in the simulations. The network analyzer allows for element specific tuning to 297 MHz and matching to better than -20 dB as well as the determination of the corresponding S_{12} values.

Image Acquisition and Evaluation

In order to visualize the different coupling of the element pairs, the phantom used in the coupling measurements was examined in a 7 T MRI system (Magnetom 7 T, Siemens Healthcare, Erlangen, Germany). Therefore, identical pairs of the constructed elements were positioned in the same way as in the coupling measurements and a gradient echo sequence ($TR = 20$ ms, $TE = 1.74$ ms, flip angle = 23°) was performed with only one element transmitting and both elements

receiving the signal. In this manner, coupling between the elements could qualitatively be visualized by the intensity distributions in axial images. Furthermore, B_1 -maps (based on spin echo and stimulated echo, $TR = 800$ ms, $TE = 14$ ms, flip angle = 90°) were acquired for all pairs of elements to examine the coupling more quantitatively via the flip angle distributions. All measurements were performed with identical input power.

2.3 Results

Modelling and Simulation

In the case of one element, 5.6 million mesh cells led to a total simulation time of 28 minutes on a high performance computing cluster employing four Nvidia Tesla M2090 graphic units for distributed computing. A reflection factor of at least -20.00 dB could be achieved for all meander sizes at a center frequency of 297 MHz.

Post Processing

The values for C_{end} that are necessary to maximize the central H-field for each meander size are depicted in Figure 2.3a. With increasing meander size (increasing electrical length) systematically smaller capacitors C_{end} lead to maximum H-field strength until at a meander size of 50 mm capacitors at the end are not necessary any more. Consequently, the ME with a meander size of 50 mm is a dipole with meanders and a ground plane as shield. This is the reason why ME with large meander sizes are denoted as dipole-like elements further on in this paper. Figure 2.3b illustrates the maximum SAR_{10g} values inside the loading phantom. While the values are comparable for meander sizes between 0 mm and 25 mm, an approximately linear decay can be observed for larger meander sizes.

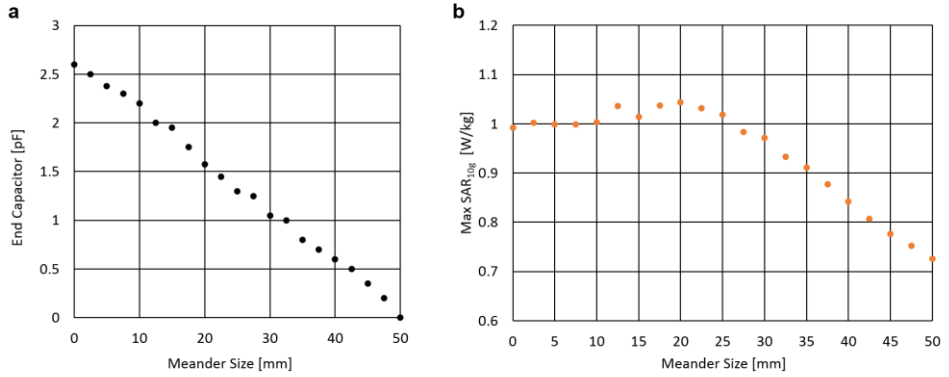


Figure 2.3: a) Values for the end capacitors obtained from H-field maximization for each single meander size. From a capacitance of 2.6 pF for a microstrip line element the values decrease approximately linearly until at a meander size of 50 mm finally no capacitance is required like it is the case for a dipole antenna. b) Plot of the maximum specific absorption rate (SAR) averaged over 10 g (Max SAR_{10g}) demonstrates advantages for larger meander sizes in this context.

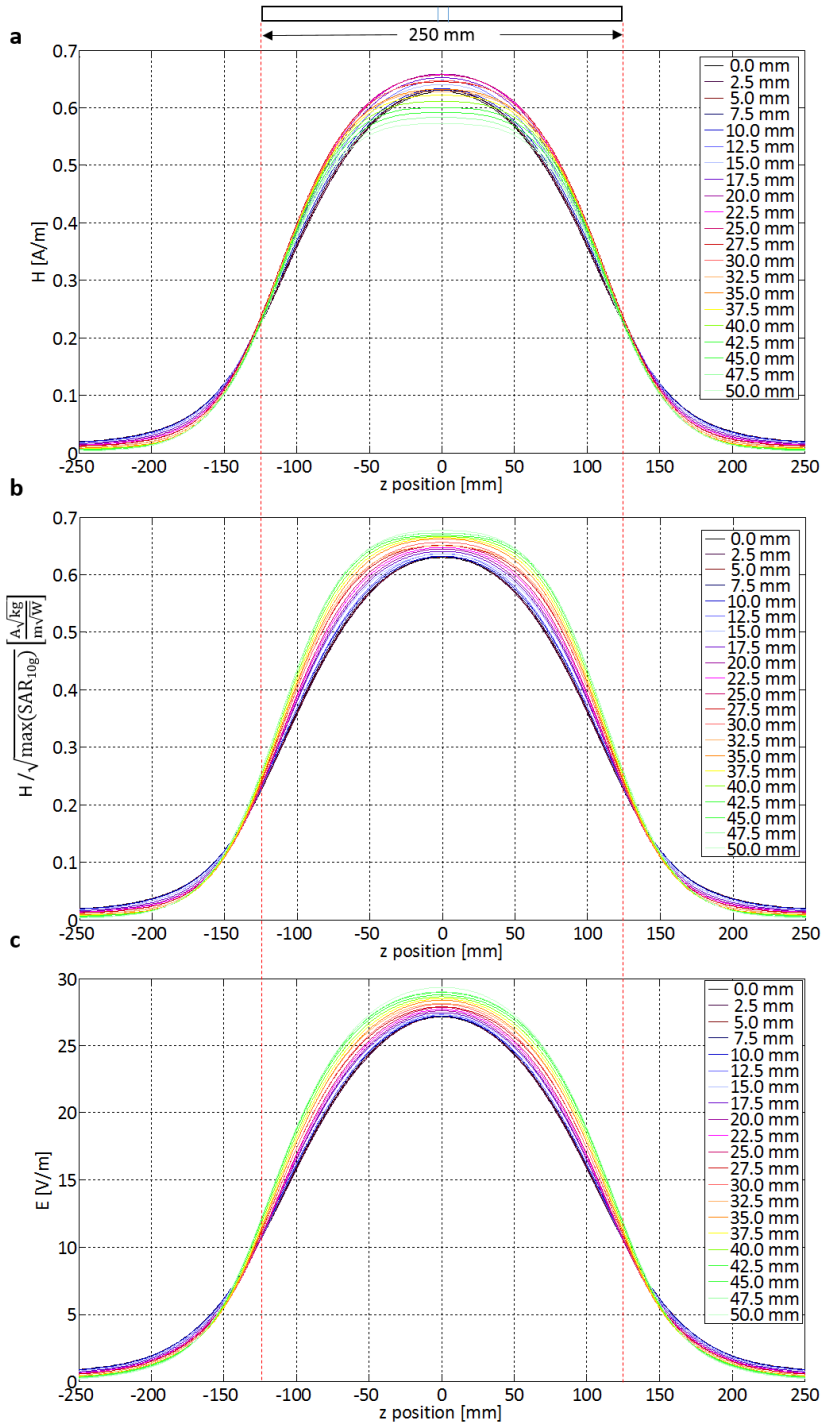


Figure 2.4: a-c) Central line plots along z-direction of the magnetic (a, b) field and electric field (c) evaluated 30 mm inside the phantom. The dimensions of the elements are indicated on top and by the red dashed lines. Medium meander sizes feature maximum central magnetic field magnitude with regard to input power (a,) while elements with large meanders are superior with regard to SAR efficiency (b). Large meander sizes show maximum electric field magnitude 30 mm inside the phantom (c) throughout the element dimensions followed by the other meander sizes in descending order illustrated in Figure 2.4c for z- and in Figure 2.5c for the y-direction.

With regard to input power, medium meander sizes allow for maximum central H-field strength (Figure 2.4a) 30 mm inside the phantom. Each element covers the z-direction from -125 mm to +125 mm which is indicated on top of Figure 2.4a. Beyond these dimensions MSL elements and ME with small meander sizes feature maximum H-field strength followed by ME with ascending meander size. Central line plots in y-direction (Figure 2.5a) 30 mm inside the phantom indicate a smooth decay of the H-field for medium meander sizes. MSL and ME with small meanders show a faster decay at first but then show a pronounced enhancement beginning at $y = -100$ mm and $y = +100$ mm on both sides. Large meander sizes decay slower at the beginning and faster in the periphery. The dimensions of one element cover the y-direction from $y = -50$ mm to $y = +50$ mm, indicated by a projection of a single element on the top of Figure 2.5a. Figures 2.4b and 2.5b show the SAR efficiency, where the H-field is normalized to the square root of the maximum SAR_{10g} . Dipole-like elements show maximum SAR efficiency throughout the element dimensions as well as maximum E-field magnitudes (Figure 2.4c and 5c).

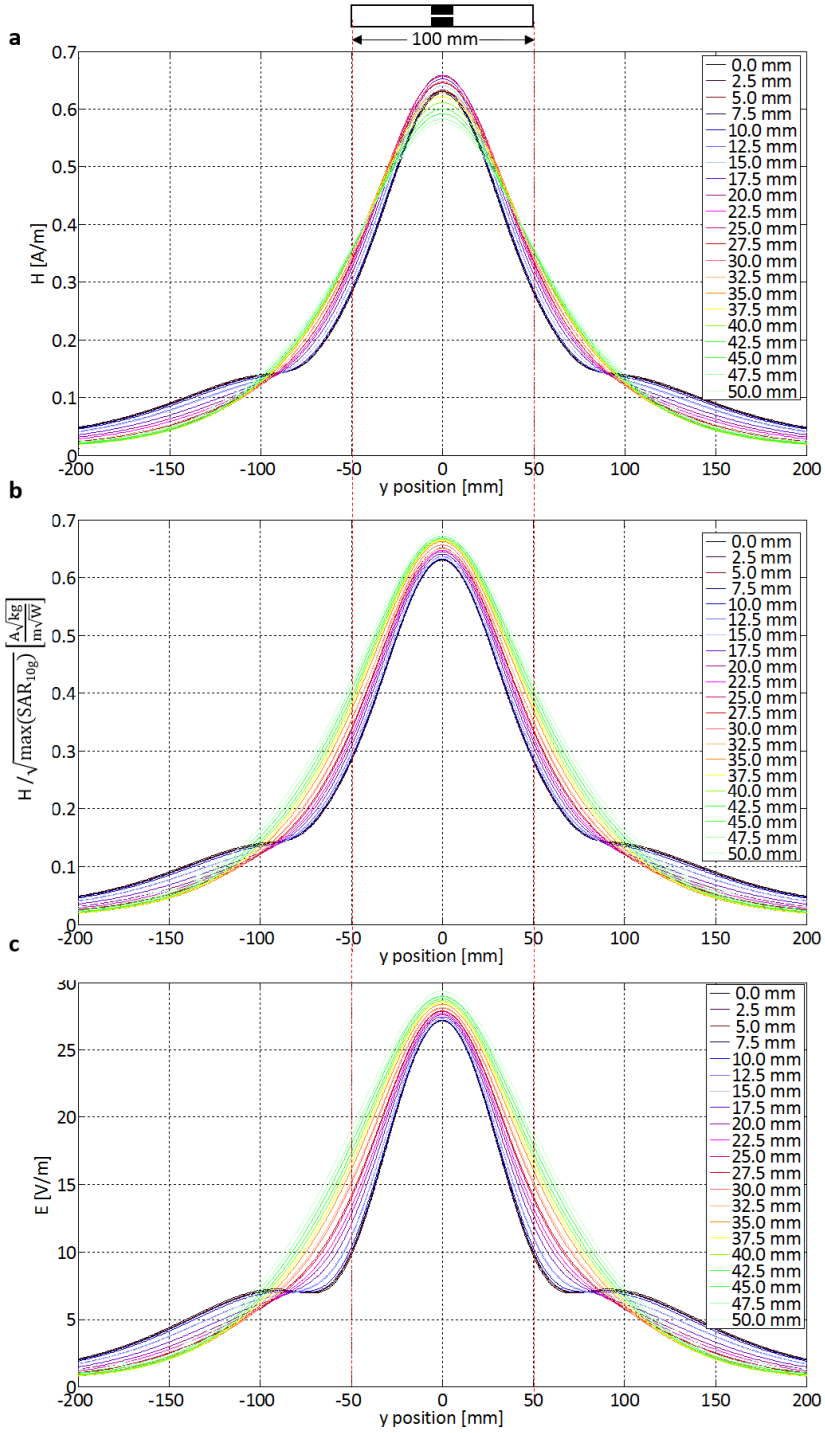


Figure 2.5: a-c) Central line plots along y-direction of the magnetic field (a, b) and electric field (c) evaluated 30 mm inside the phantom. The dimensions of the elements are indicated on top and by the red dashed lines. Medium meander sizes feature maximum central magnetic field magnitude with regard to input power (a) while elements with large meanders are superior with regard to SAR efficiency (b). Large meander sizes show maximum electric field magnitude 30 mm inside the phantom (c) throughout the element dimensions followed by the other meander sizes in descending order.

The central line plot along x-direction (Figure 2.6a) depicts the H-field magnitude inside the phantom, with $x = 0$ mm representing the phantom border near the elements. From $x = 30$ mm where the H-field was maximized a meander size of 32.5 mm features maximum magnitude until at $x = 90$ mm where dipole-like elements perform better. With regard to SAR efficiency dipole-like elements are superior in this area of the phantom followed by the meander sizes in descending order as Figure 2.6b points out. In Figure 2.6 data is only presented for three meander sizes to ensure differentiation. Data of other meander sizes fit between the presented curves.

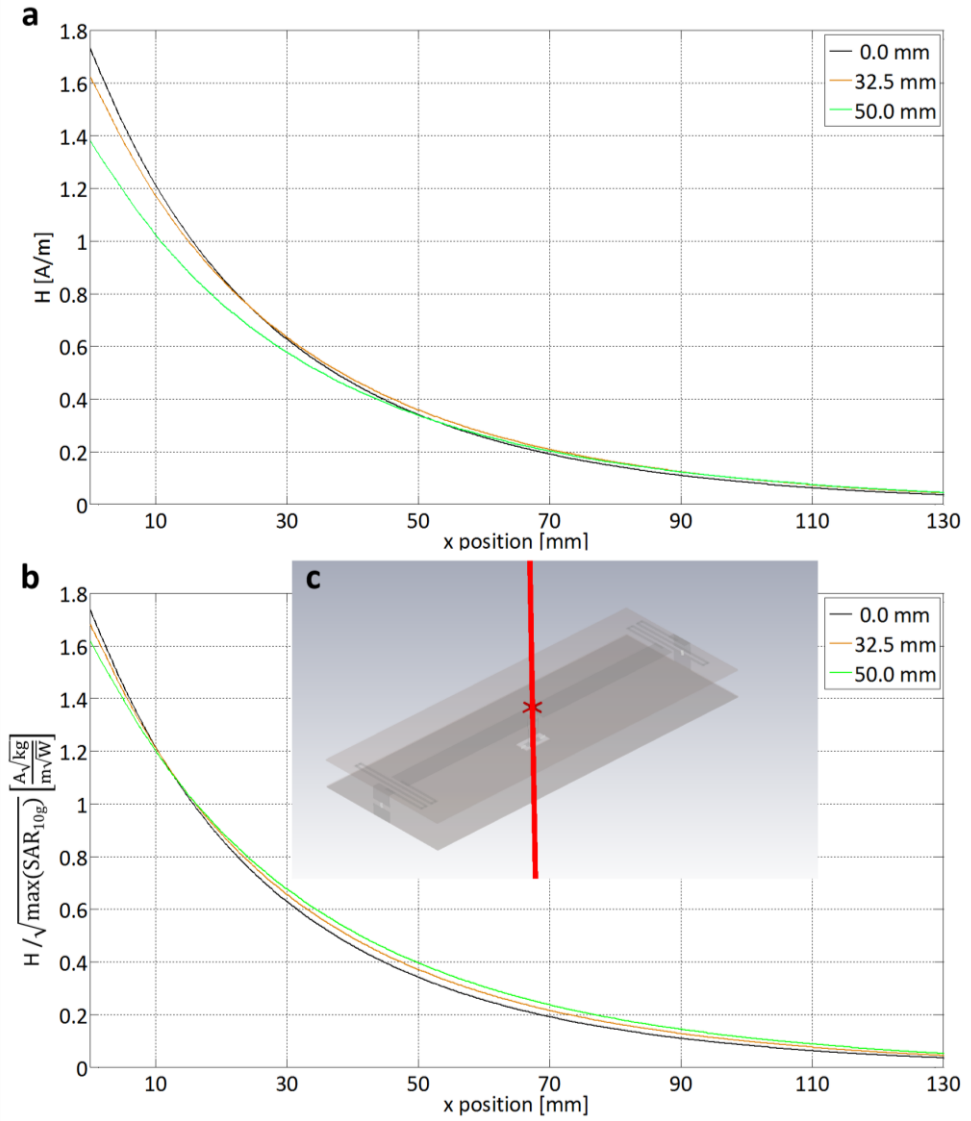


Figure 2.6: a, b) Central line plots along x-direction (illustrated in c) of the magnetic field with regard to input power (a) and with regard to SAR efficiency (b). Although the magnetic field magnitude was chosen to be maximum at $x = 30$ mm by setting

the corresponding end capacitors, in deeper lying regions of the phantom the same element order can be found. The input power is 0.5 W for all elements in all examinations.

Field Distribution

Figure 2.7 illustrates the distributions of the H-field amplitudes (d, e, f) and the E-field amplitudes (g, h, i) in the z-y-plane of the top substrate. As it can be seen regarding the 30 V m^{-1} isoline, both MSL (Figure 2.7 top row) and ME with a meander size of 50 mm (Figure 2.7 bottom row) cause higher E-field amplitudes in both directions compared to a ME with a meander size of 32.5 mm (Figure 2.7 middle row). Identical MSL elements and ME with a meander size of 50 mm that are placed directly adjacent to the ones in Figure 2.7 are consequently exposed to higher E-field amplitudes (g, i) than ME with a meander size of 32.5 mm (h). Comparable behavior is also observed for the H-field in y-direction. Here, the MSL element and the ME with a meander size of 50 mm again generate higher field amplitudes. If the H-field is examined in z-direction, the field amplitudes decrease with increasing meander size, starting with the MSL element first, followed by the ME with a meander size of 32.5 mm and the ME with a meander size of 50 mm. Therefore, the H-field of the dipole-like element with a meander size of 50 mm resembles the magnetic field of a real dipole antenna, with no field magnitude in the regions that extend beyond the conductor in the longitudinal z-direction. Field characteristics of the other meander sizes systematically lie in between the three sizes described above. Different meander sizes with their specific H- and E-field distributions also show special coupling characteristics to identical elements adjacently placed in y-direction as will be demonstrated in the following section. Figure 2.7 also shows the H (a-c) and E-field (j-l) magnitudes for the simulations with inductance implemented at the face ports which replaced the meander structures. The inductance necessary to achieve the same tuning and matching as in the original simulations with meanders was -0.2 nH for the MSL, 78.4 nH to replace 32.5 mm meanders and 177.3 nH to replace 50 mm meanders.

Consequently, the inductance increases approximately linear. In the first row of Figure 2.7 no changes occur as it can be expected. Both H (compare Figure 2.7b and e) and E-fields (Figure 2.7h and k) are optimized by introducing 32.5 mm meander structures for this element, meaning that smaller field amplitudes are observable at y-positions close-by to the element dimensions. The last row of Figure 2.7 suggests that this is exactly the other way around when elements with 50 mm meanders are examined. Here, the meander structures have a negative impact on H-field (compare Figure 2.7c and f) and E-field (Figure 2.7i and l) distributions. Lateral meander structures consequently have different influence on the fields. From the top to the bottom row in Figure 2.7 both H (a-c) and E-field amplitudes (j-l) are decreasing at y-positions close-by to the elements if an inductance is implemented. This may be redirected to the size of C_{end} since high E-fields are generated due to high voltage at high capacitor values. When meanders are introduced especially the E-field is enhanced near the 50 mm meanders. Thus, the element with 32.5 mm meanders is optimal concerning the field distributions.

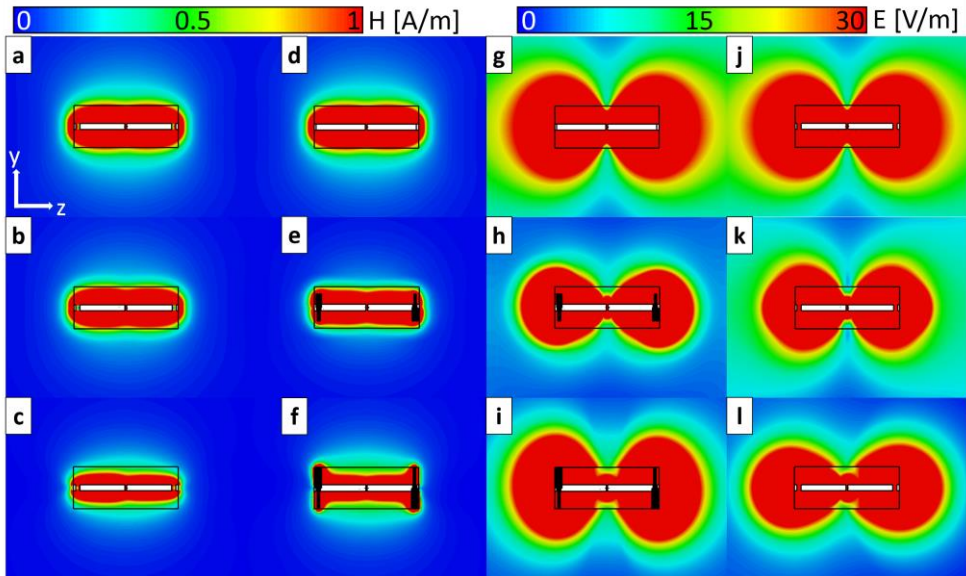


Figure 2.7: Amplitudes of H-field (a-f) and E-field (g-l) in the y-z-plane of the top substrate. Equal input power of 0.5 W was used for all experiments and scales are truncated at their maximum value. (d-i): MSL (top) and ME with sizes of 32.5 mm (middle) and 50 mm (bottom). Minimum magnitude for both H- and E-fields in y-direction can be observed for 32.5 mm indicating why coupling to close-by located elements in y-direction is minimum for medium meander sizes. (a-c, j-l): For the same elements the meander structures were substituted by ports and equipped with the inductance necessary for tuning and matching. While the first row remains unchanged, the positive effect of the meander structures can be observed in the middle row where both H (e) and E-field (h) magnitudes near the element in y-direction are smaller when meanders are used compared to H (b) and E-field (k) when an inductance is used. Considering this, the bottom row shows that introducing meander structures (50 mm) for a dipole effects the field distributions negatively.

Simulations with increased distance to the loading phantom $p = 60$ mm revealed changes regarding the power flow (absolute value of the Poynting vector S) which are shown in Figure 2.8. In the left column the power flow for the MSL element is shown followed by the ME with 32.5 mm meanders in the middle column and the ME with 50 mm meanders on the right. Figure 2.8a-f shows the power flow at the center position normal to the conductor for $p = 30$ mm (a-c) and $p = 60$ mm (d-f). Below the corresponding power flow is illustrated for $p = 30$ mm (g-i) and $p = 60$ mm (j-l) on a slice located at the end of the elements. The power flow at close-by y-positions is increased for all elements when the distance to the phantom is enhanced, yet this effect is least prominent for the ME with 32.5 mm meanders. This is true for the fields at the center position as well as for the fields at the end of the elements. Figure 2.8a-c indicates that ME exhibit power flow primary towards the phantom compared to the MSL. Especially the ME with 32.5 mm meanders seems to be favorable. This can also be observed at the end of the element (Figure 2.8g-i). In Figure 2.8a-f the Q-factors are included which were calculated from the 3 dB bandwidth. For all elements the Q-factor increased with increasing distance to the loading phantom. This effect is most prominent for the ME with 32.5 mm meanders followed by the MSL and the ME with 50 mm meanders. The distribution of the power flow in y-direction is qualitatively comparable to the power flow at

the end of the element for each element type both at $p = 30$ mm and $p = 60$ mm. As the Poynting vector is the product of H- and E-field it is important to note that absolute values of both H- and E- field (which were investigated but are not shown here) behave equally, meaning for example that the high power flow on y-positions close-by to the element in Figure 2.8j is due to both higher H- and E-fields compared to the other element types.

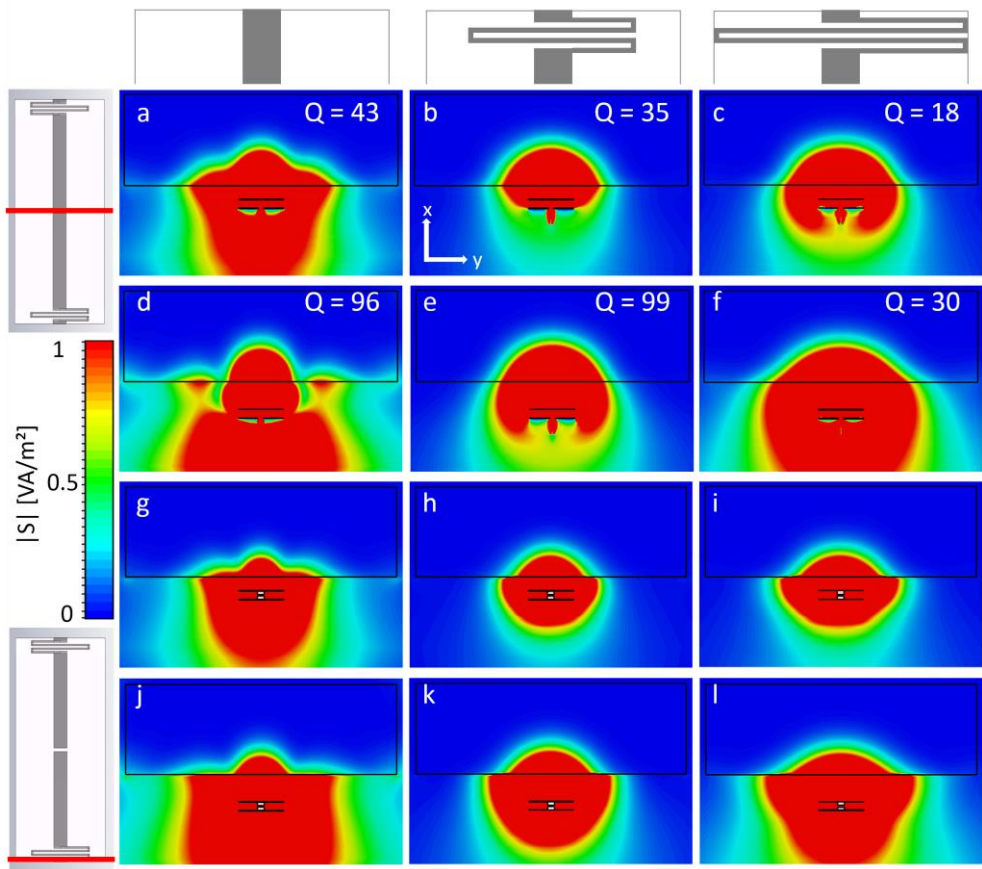


Figure 2.8: Power flow (absolute value of the Poynting vector S) in the center of the element (a-f) and at the end of the element (g-l). The position of the slices is indicated on the left, the element size on the top. When the distance of the element to the phantom is increased from $p = 30$ mm (a-c, g-i) to $p = 60$ mm (d-f, j-l) the

power flow is spreading further in the y -direction, at both the center and the position at the end of the elements, for the MSL (left column) and the ME with 50 mm meanders (right column) compared to the ME with 32.5 mm meanders (middle column). For the ME with 32.5 mm the power flow is focused in an optimum way towards the loading phantom at $p = 30$ mm. The Q-factors increase when the distance to the phantom is increased (a-f). The scale is truncated at the maximum.

Coupling in Simulations

For the simulation of two elements a gridded mesh with 10 million mesh cells necessitated a total simulation time of 73 minutes on the system described above. Again, the meshing was refined near the meander structures to 0.5 mm. With only slight adjustments on the parallel and matching capacitors, tuning to a center frequency of 297 MHz and a reflection factor S_{11} of at least -20.00 dB could be achieved without changing the capacitors at the end. In Figure 2.9 the transmission S_{12} between adjacent elements with identical meander size is illustrated. Starting with two MSL elements, for a spacing between the elements of $d = 10$ mm at first the coupling decreases when the meander size is increased until an optimum at 27.5 mm is reached. Further increasing the meander size subsequently leads to increased coupling for dipole-like elements. Basically, the main features of this behavior are preserved when the spacing between the elements is increased to $d = 30$ mm, $d = 50$ mm and $d = 100$ mm, with the difference that the minimum is shifted to elements featuring larger meander size. Also, it should be noted that dipole-like elements benefit most from increased distance between the elements compared to ME with small and medium meander sizes alike. In fact, for the meander sizes 22.5 mm, 25.0 mm and 27.5 mm the coupling is lower for $d = 10$ mm than it is for $d = 30$ mm and $d = 50$ mm. For all other sizes coupling is lower for higher distances d . Advantages for dipole-like elements compared to small meander sizes when the inter element spacing is increased, can be explained by the field distributions in Figure 2.7. While the fields are comparable in the regions close

to the elements in y-direction, the field amplitudes are higher for small meander sizes in more distant regions.

Replacing meander structures with an inductance located at both ends of the element results in different coupling behavior. Simulations with an inductance resulted in $S_{12} = -10.10$ dB for the MSL (original with meanders $S_{12} = -10.08$ dB), $S_{12} = -16.66$ dB for elements which first had 32.5 mm meanders (original with meanders $S_{12} = -21.31$ dB) and $S_{12} = -18.62$ dB for elements which had 50 mm before (original with meanders $S_{12} = -8.90$ dB). Consequently, a positive impact can be stated for the medium meander size while the contribution of the lateral meanders is negative for large meander size. This was basically expected from the results illustrated in Figure 2.7.

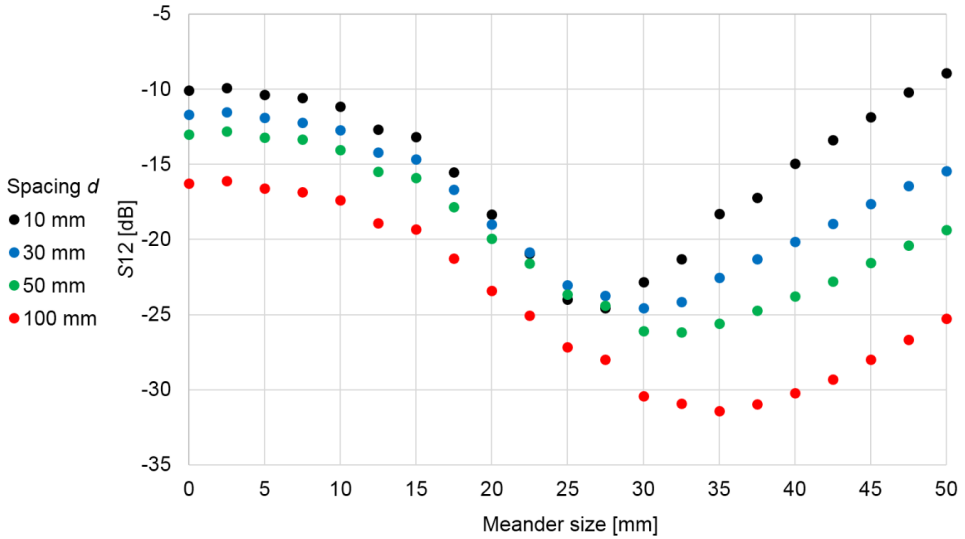


Figure 2.9: Impact of changing spacing d between the top planes of identical elements on the transmission S_{12} in the simulations. Increasing the spacing leads to a shift of the optimum values for S_{12} to larger meander sizes. While medium meander sizes overall feature minimum coupling, dipole-like elements benefit most

from increased spacing at these loading conditions with a distance of $p = 30$ mm to the phantom.

Different loading conditions influence the performance of an RF antenna as well as the coupling to neighboring antenna elements. Consequently, simulations including two identical elements with an increased distance $p = 60$ mm to the phantom were executed for all meander sizes. After tuning to 297 MHz and element dependent matching to better than -20 dB, the S_{12} values could be compared to the values of simulations with $p = 30$ mm. Figure 2.10a presents the transmission S_{12} for $p = 60$ mm and $p = 30$ mm both for a spacing $d = 10$ mm between the elements. Minimum coupling is achieved for a meander size of 27.5 mm in both cases. Coupling is lower for $p = 30$ mm throughout all meander sizes, yet, the difference of the two values is minimum for a meander size of 27.5 mm. Thus, 27.5 mm is the optimum meander size independent of the distance p to the loading phantom for an inter element spacing $d = 10$ mm. In another simulation run the distance to the loading phantom was kept $p = 60$ mm but the inter element spacing was increased to $d = 100$ mm. An unchanged minimum coupling independent of the element spacing is pointed out for a meander size of 27.5 mm in Figure 2.10b. Coupling is decreasing for all meander sizes when the spacing is increased to $d = 100$ mm, however, the gain is maximum for a meander size of 27.5 mm, and much higher for dipole-like elements compared to MSL elements and ME with small meander sizes.

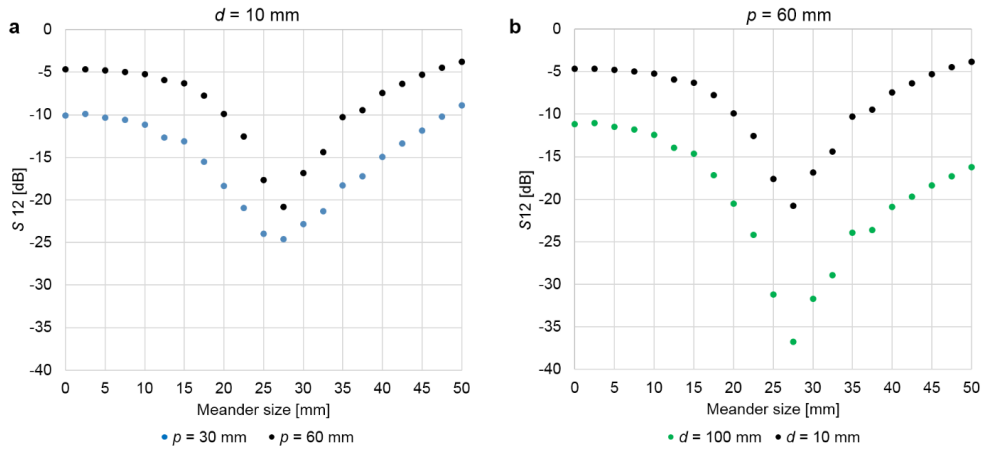


Figure 2.10: Evaluation of the transmission S_{12} for different loading conditions. a) For a fixed inter element spacing of $d = 10$ mm, increasing the distance to the loading phantom from $p = 30$ mm to $p = 60$ mm maximizes the coupling for all simulated meander sizes. b) Changing the inter element spacing from $d = 10$ mm to $d = 100$ mm at a fixed distance of $p = 60$ mm to the loading phantom leaves the optimum meander size of 27.5 mm unchanged.

Coupling Measurements

Tuning to a center frequency of 297 MHz and a matching of better than -20 dB was achieved for all elements using fixed capacitors and trimming capacitors for fine tuning in parallel. In contrast to elements with a medium meander size, MSL elements and ME with a size of 50 mm necessitated the use of cable traps (BalUn with discrete inductance and trimmer in parallel on the shield of the coaxial cable) because tuning, matching and inter element coupling of those elements was sensitive to cable positioning. Simulations point out that the impact of the positioning aids is negligible since they do not alter the overall H-field distribution in the central line plot 30 mm inside the phantom and the change in maximum central H-field strength is below 1 %. Two measurements of the phantom fluid on the network analyzer described above, resulted in a permittivity of $\epsilon_r = 47.93 \pm 0.75$

and a conductivity of $\sigma = 0.68 \pm 0.02 \text{ S m}^{-1}$. Table 2.1 illustrates the transmission S_{12} between identical elements in the measurements for all chosen geometric setups.

Table 2.1: Experimental validation of the transmission S_{12} from simulations for four pairs of elements with the meander sizes 0 mm (microstrip line element), 27.5 mm, 32.5 mm and 50 mm (dipole with meanders). The coupling measurements show good agreement to the simulated results in all tested geometric setups with changing both the distance to the phantom p and the inter element spacing d .

p [mm]	d [mm]	Meander Size [mm]	S_{12} [dB] Measurement	S_{12} [dB] Simulation
30	10	0	-10.1	-10.08
30	10	27.5	-27.0	-24.58
30	10	32.5	-26.4	-21.31
30	10	50.0	-7.1	-8.90
30	30	0	-11.6	-11.70
30	30	27.5	-26.0	-23.73
30	30	32.5	-29.0	-24.16
30	30	50.0	-12.6	-15.43
30	100	0	-19.0	-16.27
30	100	27.5	-28.6	-27.98
30	100	32.5	-28.6	-30.91

30	100	50.0	-21.0	-25.25
60	10	0	-7.0	-4.64
60	10	27.5	-18.1	-20.80
60	10	32.5	-20.9	-14.40
60	10	50.0	-2.5	-3.81
60	100	0	-14.5	-11.19
60	100	27.5	-29.1	-36.74
60	100	32.5	-31.7	-28.90
60	100	50.0	-17.6	-16.20

Image Acquisition and Evaluation

Axial views of a gradient echo sequence (Figure 2.11a-d) qualitatively show enhanced coupling for MSL elements (a) and ME with a meander size of 50 mm (d) compared to ME with meander sizes of 27.5 mm (b) and 32.5 mm (c). In all cases (Figure 2.11a-h) the left element is used for transmission and both elements are used for receiving. Equal coupling characteristics are also indicated in coronal B_1 -maps, illustrating the flip angle distributions for all constructed element pairs, 10 mm inside the phantom liquid (Figure 2.11e-h). ME with meander sizes of 27.5 mm (f) and 32.5 mm (g) feature a comparable homogeneity below the transmitting element and no excitation below the other element can be observed, as it can be expected. This is not true for MSL elements (e) and ME elements with a meander size of 50 mm (h) alike, which both show an excitation pattern underneath the element on the right side which is not used for transmission. Additionally, MSL elements (e) only excite a smaller region in the left-right direction when compared to medium meander sizes (f,g), while the ME with a meander size of 50 mm excite a broader area in this coronal slice.

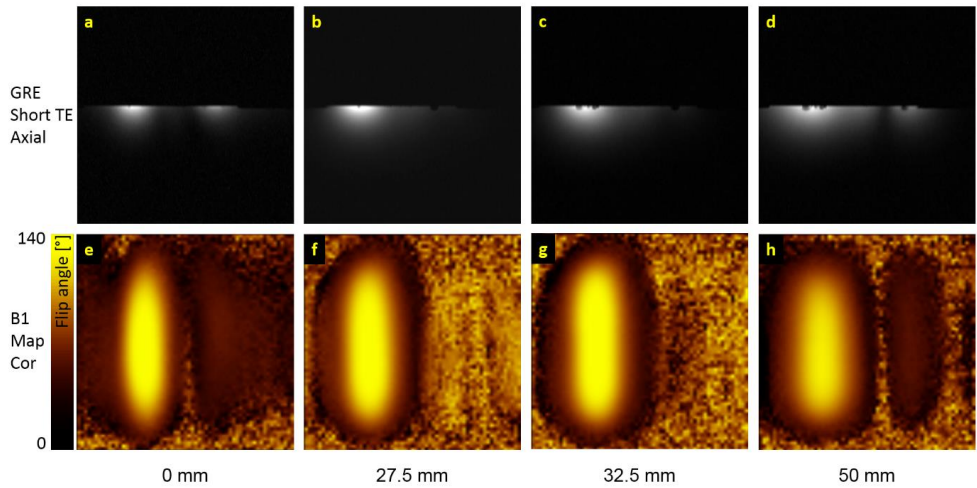


Figure 2.11: Examinations of the phantom used for the coupling measurements and the different pairs of transmit elements on a 7 T MRI system. In all images only the left element was used for transmitting while both elements are receiving the signal. In axial views of a gradient echo sequence (a-d) higher intensity below the right element points out enhanced coupling for MSL elements (a) and ME with a meander size of 50 mm (d) compared to ME with meander sizes of 27.5 mm (b) and 32.5 mm (c). B1-maps (e-h) illustrating the flip angle distributions in a coronal slice 10 mm inside the phantom liquid quantitatively illustrate the different coupling observed in a-d.

2.4 Discussion

In this work, the influence of different meander sizes on the RF transmit performance and coupling between identical microstrip line elements at 7 T was systematically evaluated. Good agreement between the trends of the S_{12} values in both simulations and subsequent measurement was achieved.

Field optimization by variation of the end capacitors showed an inverse linear dependency between the meander size and the end capacitors. This gives rise to the assumption that increasing the geometric dimensions of the meander structure simply introduces additional electrical length which is compensated by a lower capacitance. Indeed the inductance necessary to replace meander structures increases approximately linear with increasing meander size. Maximum central H-field strength with regard to equal input power 30 mm inside the loading phantom could be observed for ME with medium meander sizes. Concerning SAR efficiency dipole-like elements are superior. MSL elements and ME with small meanders are least efficient in both cases. ME with medium meander sizes feature low H-field strength at both y-positions and z-positions that are not covered by the dimensions of the element.

Examinations of the coupling between identical RF elements in the simulations primarily point out that minimum coupling is a function of the meander size. Thereby, ME with medium meander size, which also show maximum central H-field strength with regard to input power in a homogeneous phantom, perform best. With simultaneous consideration of real antenna arrays, where two or more elements are directly neighboring each other, this advantage becomes even more fundamental. The distributions of H- and E-fields have been identified as the main cause for the improved coupling characteristics of medium meander sizes compared to MSL elements, ME with small meanders, and dipole-like elements. We assume minimum field amplitudes to cause less power transfer to adjacent elements. This assumption could be bolstered by the examinations of the power flow. As only C_{end} and the lateral extension of the meanders is changing among the

elements, one or both aspects maybe responsible for the different coupling behavior. The investigations suggest that indeed both effects seem to contribute. The first reason is that MSL elements with low inductance and high C_{end} show enhanced coupling compared to higher inductance combined with smaller C_{end} . Introducing meander structures is changing the H- and E-field distribution and consequently the coupling behavior. As second reason the qualitatively comparable shaping of the power flow at both center and end position of each element can be considered. If the coupling would only occur due to the fields of the meander structures, the differences in power flow should primary occur at the end of the element.

Variation of spacing between the elements in the range from $d = 10$ mm to $d = 30$ mm and $d = 50$ mm leaves the coupling between elements with medium meander sizes almost unchanged. For MSL elements and elements with small meanders the coupling decreases with increasing distance d . This can also be observed for dipole-like elements. The coupling between dipole-like elements benefits most from increased inter element spacing. A distance between the elements of $d = 100$ mm minimizes the coupling for all sizes even further. Field examinations with inductance showed that meander structures basically have a positive impact on the inter element coupling, but this positive effect is diminished when the meander structures of adjacent elements come too close. This can explain the shift of the minimum S_{12} value towards larger meander sizes with increased inter element spacing for the loading conditions at $p = 30$ mm.

This shift of the minimum S_{12} value for varying d could not be reproduced as the loading conditions were changed by increasing the distance to the phantom from $p = 30$ mm to $p = 60$ mm. In contrast to $p = 30$ mm for $p = 60$ mm the lowest coupling is achieved with a meander size of 27.5 mm for both $d = 10$ mm and $d = 100$ mm. This could be due to reduced coupling between meander structures while inductive coupling is enhanced (since the Q-values increase). What could be reproduced is the larger benefit concerning S_{12} for dipole-like elements compared

to small meander sizes when the inter element spacing d is enlarged. Accordingly, this behavior seems to be independent of the loading conditions. Increasing the distance to the loading phantom leads to higher S_{12} values for all meander sizes. The most probable reason is reduced coupling to the phantom. Consequently, radiation of the elements is increased since the setup with a distant phantom approaches the case of two adjacent antennas in free space. This can be explained by the investigations of the power flow which showed that more power is radiated to the side and to the back in direction of the ground plane when the distance to the loading phantom is increased.

The measurements of the coupling showed that ME with medium meander size do not necessitate the use of cable traps. The direct comparison of S_{12} values in simulations and measurements largely confirm the simulation results. However, the measurements are not perfectly identical to the simulations since cables and cable traps are not included in the simulations and, furthermore, geometric dimensions of the tuning and matching circuit are not exactly represented in the same way in the simulations. Additionally, tolerances of capacitor values, and slight differences in permittivity and conductivity of the phantom liquid cause errors. To evaluate the impact of different conductivity in simulations ($\sigma = 0.87 \text{ S m}^{-1}$) and measurements ($\sigma = 0.68 \text{ S m}^{-1}$) additional simulation runs with $\sigma = 0.68 \text{ S m}^{-1}$ were performed for the meander sizes 0, 32.5 and 50 mm. The resulting coupling values are $S_{12} = -10.59 \text{ dB}$ for 0 mm, $S_{12} = -20.29 \text{ dB}$ for 32.5 mm and $S_{12} = -9.01 \text{ dB}$ for 50 mm. Consequently, the differences between the different conductivities in the simulations are small compared to the differences between measurement and original simulation. After all, good agreement between the trends of measurements and simulations and even distribution of discrepancies among the measured S_{12} values confirm the results of the measurements and of the simulations.

Close agreement between measurements and simulations of inter element coupling could also be substantiated by image acquisition on the 7 T MRI system. Axial views acquired with a gradient echo sequence show minimum coupling for

ME with medium meander size. It has to be taken into account that transmit and receive field are both contributing to the overall image intensities which are the basis of this comparison. However, this is not an issue for the presented B_1 -maps since the receive field is cancelled out in the calculation of these flip angle distributions. Consequently, the B_1 -maps are a reliable indication of the improved coupling characteristics medium sized ME inherently show.

2.5 Conclusion

In this work it could be shown that medium sized meander structures minimize coupling between identical adjacent ME compared to ME with enlarged meander size, which approximates a shielded dipole antenna, and to ME with reduced size, which converges to the case of a MSL. Simulations featuring varying loading conditions and inter element spacing substantiate these coupling characteristics in the examined element setups. Furthermore, phantom measurements of the coupling between identical elements and the measured 7 T B_1 -maps confirm the simulation results. While the differences in the magnitude of the H-fields inside the phantom are moderate, it can be stated that medium sized ME feature optimum H-field strength and distribution with regard to input power throughout the dimensions of the phantom. With regard to SAR efficiency they show average performance while dipole-like elements are advantageous in this context. Considering this, RF transmit-arrays consisting of side-by-side located elements with the presented geometry can be optimized depending on the desired application by balancing inter element coupling, field and SAR characteristics.

Acknowledgements

The authors wish to thank Andreas K. Bitz, DKFZ Heidelberg, Germany, for his support with the realization of the RF simulations and Tristan Mathiebe from the Erwin L. Hahn Institute in Essen, Germany, for his help with antenna element construction.

The research leading to these results has received funding from the European Research Council under the European Union's Seventh Framework Programme (FP/2007-2013) / ERC Grant Agreement n. 291903 MRexcite.

References

1. Hoult DI, Phil D. Sensitivity and Power Deposition in a High-Field Imaging Experiment. *J Magn Reson Imaging* 2000;67:46–67.
2. Wiesinger F, Boesiger P, Pruessmann KP. Electrodynamics and ultimate SNR in parallel MR imaging. *Magn Reson Med* 2004;52(2):376–90.
3. Ohliger MA, Grant AK, Sodickson DK. Ultimate intrinsic signal-to-noise ratio for parallel MRI: electromagnetic field considerations. *Magn Reson Med* 2003;50(5):1018–30.
4. Vaughan JT, Garwood M, Collins CM, Liu W, Delabarre L, Adriany G, Andersen P, Merkle H, Goebel R, Smith MB, et al. 7T vs. 4T: RF power, homogeneity, and signal-to-noise comparison in head images. *Magn Reson Med* 2001;46(1):24–30.
5. Yang QX, Wang J, Zhang X, Collins CM, Smith MB, Liu H, Zhu X-H, Vaughan JT, Ugurbil K, Chen W. Analysis of wave behavior in lossy dielectric samples at high field. *Magn Reson Med* 2002;47(5):982–9.
6. Collins CM, Liu W, Swift BJ, Smith MB. Combination of optimized transmit arrays and some receive array reconstruction methods can yield homogeneous images at very high frequencies. *Magn Reson Med* 2005;54(6):1327–32.
7. Mao W, Smith MB, Collins CM. Exploring the limits of RF shimming for high-field MRI of the human head. *Magn Reson Med* 2006;56(4):918–22.
8. Katscher U, Börnert P, Leussler C, van den Brink JS. Transmit SENSE. *Magn Reson Med* 2003;49(1):144–50.
9. Grissom W, Yip C, Zhang Z, Stenger VA, Fessler JA, Noll DC. Spatial domain

- method for the design of RF pulses in multicoil parallel excitation. *Magn Reson Med* 2006;56(3):620–9.
10. Orzada S, Maderwald S, Poser BA, Bitz AK, Quick HH, Ladd ME. RF excitation using time interleaved acquisition of modes (TIAMO) to address B1 inhomogeneity in high-field MRI. *Magn Reson Med* 2010;64(2):327–33.
 11. Avdievich NI. Transceiver-Phased Arrays for Human Brain Studies at 7 T. *Appl Magn Reson* 2013;41:483–506.
 12. Gräßl A, Winter L, Thalhammer C, Renz W, Kellman P, Martin C, von Knobelsdorff-Brenkenhoff F, Tkachenko V, Schulz-Menger J, Niendorf T. Design, evaluation and application of an eight channel transmit/receive coil array for cardiac MRI at 7.0 T. *Eur J Radiol Elsevier Ireland Ltd*; 2013;82(5):752–9.
 13. Kraff O, Bitz AK, Kruszona S, Orzada S, Schaefer LC, Theysohn JM, Maderwald S, Ladd ME, Quick HH. An eight-channel phased array RF coil for spine MR imaging at 7 T. *Invest Radiol* 2009;44(11):734–40.
 14. Aussenhofer SA, Webb AG. An eight-channel transmit/receive array of TE01 mode high permittivity ceramic resonators for human imaging at 7T. *J Magn Reson Elsevier Inc.*; 2014;243:122–9.
 15. Brunner DO, De Zanche N, Froehlich J, Baumann D, Pruessmann KP. A symmetrically fed microstrip coil array for 7T. *Proc Intl Soc MRM* 15 2007. p. 448.
 16. Metzger GJ, Snyder C, Akgun C, Vaughan T, Ugurbil K, Van de Moortele P-F. Local B1+ shimming for prostate imaging with transceiver arrays at 7T based on subject-dependent transmit phase measurements. *Magn Reson*

- Med 2008;59(2):396–409.
17. Snyder CJ, DelaBarre L, Metzger GJ, van de Moortele P-F, Akgun C, Ugurbil K, Vaughan JT. Initial results of cardiac imaging at 7 Tesla. *Magn Reson Med* 2009;61(3):517–24.
 18. Vaughan JT, Snyder CJ, DelaBarre LJ, Bolan PJ, Tian J, Bolinger L, Adriany G, Andersen P, Strupp J, Ugurbil K. Whole-body imaging at 7T: preliminary results. *Magn Reson Med* 2009;61(1):244–8.
 19. Raaijmakers AJE, Ipek O, Klomp DWJ, Possanzini C, Harvey PR, Lagendijk JJW, van den Berg CAT. Design of a radiative surface coil array element at 7 T: the single-side adapted dipole antenna. *Magn Reson Med* 2011;66(5):1488–97.
 20. Orzada S, Bahr A, Bolz T. A novel 7 T microstrip element using meanders to enhance decoupling. *Proc Intl Soc MRM* 16 2008. p. 2979.
 21. Orzada S, Bitz AK, Schäfer LC, Ladd SC, Ladd ME, Maderwald S. Open design eight-channel transmit/receive coil for high-resolution and real-time ankle imaging at 7 T. *Med Phys* 2011;38(3):1162–7.
 22. Maderwald S, Orzada S, Schäfer LC, Bitz AK, Brote I, Kraff O, Theysohn JM, Ladd ME, Ladd SC, Quick HH. 7T Human in vivo Cardiac Imaging with an 8-Channel Transmit/Receive Array. *Proc Intl Soc MRM* 17 2009. p. 822.
 23. Orzada S, Kraff O, Schäfer LC, Brote I, Bahr A, Bolz T, Maderwald S, Ladd ME, Bitz AK. 8-channel transmit/receive head coil for 7 T human imaging using intrinsically decoupled strip line elements with meanders. *Proc Intl Soc MRM* 17 2009;3010.
 24. Theysohn JM, Kraff O, Orzada S, Theysohn N, Classen T, Landgraeber S,

- Ladd ME, Lauenstein TC. Bilateral hip imaging at 7 Tesla using a multi-channel transmit technology: initial results presenting anatomical detail in healthy volunteers and pathological changes in patients with avascular necrosis of the femoral head. *Skeletal Radiol* 2013;42(11):1555–63.
25. Orzada S, Maderwald S, Kraff O, Brote I, Ladd ME, Solbach K, Yazdanbakhsh P, Bahr A, Fautz H-P, Bitz AK. 16-channel Tx / Rx body coil for RF shimming with selected Cp modes at 7T. *Proc Intl Soc MRM* 18 2010;50.
26. Chen Z, Solbach K, Erni D, Rennings A. Coupling Investigation of Different RF Coil Elements for 7-Tesla Magnetic Resonance Imaging based on Characteristic Mode Analysis. *IEEE Int Microw Symp* 2014;1050.

Chapter 3 Parallel Transmit Capability of Various RF Transmit Elements and Arrays at 7T MRI*

Purpose

In this work, 22 configurations for remote radiofrequency (RF) coil arrays consisting of different transmit element designs for 7T ultrahigh field MRI are compared by numerical simulations.

Methods

Investigated transmit RF element types are rectangular loops, micro striplines (MSL), micro striplines with meanders (ME), 250 mm shielded dipoles with meanders (SDM), and lambda over two dipoles with and without shield. These elements are combined in four different configurations of circumferential RF body arrays with four or eight transmit elements each. Comparisons included coupling behavior, degrees of freedom (DOF) offered by the individual transmit patterns, and metrics like power and specific absorption rate (SAR) efficiency.

Results

Coupling between neighboring RF elements is elevated (up to -7 dB) for all arrays with eight elements, while it is below -25 dB for arrays with only four elements. The cumulative sum of singular values points out highest DOF for the central transversal, reduced values in the central coronal and minimum values in

the sagittal slice. Concerning power and SAR efficiency, eight λ over two dipoles are most advantageous.

Conclusion

Among the investigated remote arrays and parameters, a combination of eight dipoles seems to be most favorable for potential use in 7T body MRI.

*published as: Rietsch SHG, Orzada S, Bitz AK, Gratz M, Ladd ME, Quick HH. Parallel Transmit Capability of Various RF Transmit Elements and Arrays at 7T MRI. Magnetic Resonance in Medicine 2018, 79(2):1116-1126

3.1 Introduction

Magnetic Resonance Imaging (MRI) at ultrahigh field strengths (UHF) like 7 tesla (T) and above offers higher signal-to-noise ratio (SNR) (1–3) and potentially improved soft tissue contrast when compared to the clinically used lower field strengths of 1.5 T and 3 T. Body MR imaging at 7 T, however, is impeded by highly inhomogeneous radiofrequency (RF) excitation (1,4). This is due to the higher Larmor frequency and associated reduced wavelength in human tissue that leads to wave effects (constructive and destructive interference of the channel-dependent B_1^+ transmit fields in multichannel RF arrays) and limited penetration depth into the human body. Consequently, the achievable flip angle distribution is not only inhomogeneous but also decays toward the center of the body, which is a fundamental limitation of UHF body MRI. Several approaches to compensate for these inhomogeneities have been presented (5–9). However, the performance of all of these approaches substantially benefits from RF transmit coil designs fulfilling particular requirements, such as low coupling between individual RF elements and sufficient coupling to the object to allow for high power efficiency. High coupling between coil elements also impedes the transmit field shaping capabilities of the RF array (10).

For 7 T body applications, as for example demonstrated in references (11–18), almost exclusively close-fitting RF coil arrays are used. A fixed and small distance of the transmit/receive coil to the subject under investigation is one of the advantages of these close-fitting RF arrays. A second advantage is the limited amount of radiated RF due to the strong coupling to the body tissue. Nevertheless, the space inside of the magnet bore is limited since the inner bore diameter of 7 T systems is normally 60 cm, and both patient and close-fitting local RF coil arrays which can be bulky have to fit into this constrained space. This spatial constraint limits the maximum patient size for 7 T MRI body imaging. Furthermore, the local transmit/receive RF coil has to be positioned and fixed on the patient, which prolongs preparation times. Using remote RF coil arrays instead

(4,19), where the RF coil is mounted behind the inner bore liner, avoids these spatial constraints and associated drawbacks and progresses the UHF MRI examination of patients to a more clinic-like workflow. Also, the achievable transmit field-of-view (FOV) in the z-direction (B_0 direction) can be readily increased up to 50 cm (19), which, especially in the context of body MRI, can be considered a precondition when imaging large organs and body regions or when performing multi-station examinations.

Previous work on remote RF coil arrays is primarily focused on lower field systems. Guérin et al. (10) simulated different 3 T remote arrays with 4, 8, 16 and 32 loop RF elements that were arranged on up to four rings. The work by Guérin showed that the cumulative sum of singular values resulting from the complex B_1^+ transmit fields of the different transmit elements can be used as a measure to compare the available degrees of freedom (DOF) for RF manipulation among different RF coil arrays. Arrays with an increasing number of elements showed a trend to better performance concerning power and specific absorption rate (SAR) efficiency as well as homogeneity.

Regarding 7 T UHF MRI, Flöser et al. (20) investigated a comparison between an 8-channel close-fitting (12) RF array, a 16-channel rigid RF coil (21), which can be seen as a hybrid between close-fitting and remote, an 8-channel remote RF coil array (19), a 16-channel remote array with all elements on one ring, and a 16-channel remote RF array with two rings. In this work, which was focused on RF pulse calculation, close-fitting arrays performed best regarding homogeneous excitation in transversal slices, while in coronal slices remote coils were superior. However, the five RF arrays in that study (20) were ideally decoupled, limiting the comparability to a real coil setup. To our knowledge no further publications on 7 T (or higher field) remote RF coil arrays are currently available.

While the two studies cited above (10,20) were constrained to one specific type of RF coil element each, work in the present study is focused on simulation and investigation of remote RF transmit coil arrays using different types of RF coil

elements, namely loops, micro striplines (MSL), meander elements (ME), shielded dipoles with meanders (SDM) that were previously compared for close-fitting coils in (22), lambda over two dipoles and shielded lambda over two dipoles (SD). These six RF element types were either arranged in RF arrays using exclusively a single element type or as combinations of each RF element type with loops. Altogether, 22 remote RF arrays were simulated and compared with regard to inter-element coupling, power balance, DOFs achievable with the B_1^+ transmit patterns, power efficiency, and SAR efficiency. Care is taken to incorporate loss mechanisms and to approach a realistic RF coil array setup that could be mounted inside the bore liner of a 7 T human UHF MRI system.

3.1 Methods

Simulation

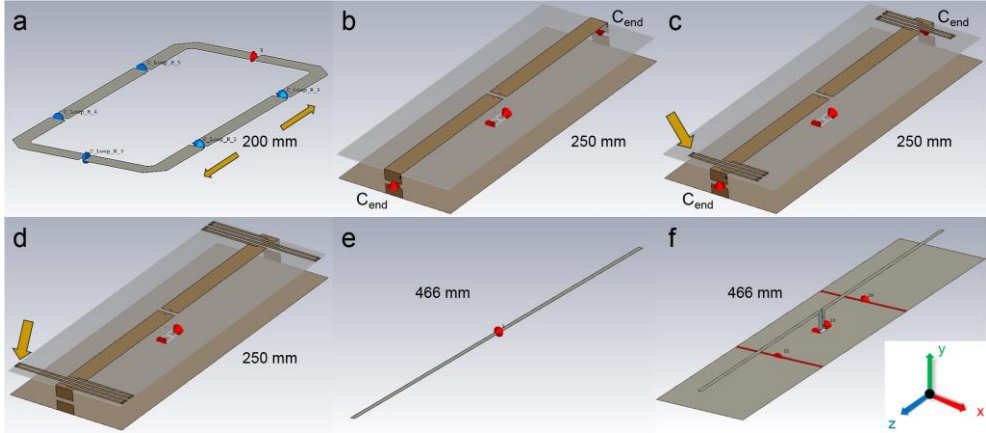


Figure 3.1: Depiction of the 6 investigated elements: rectangular loop (a), microstrip line (MSL) (b), meander element (ME) obtained by introducing meander structures (arrow) at the end of the microstrip line (c), shielded dipole with larger (arrow) meanders (SDM) and without end capacitors (d), lambda over two dipole (e), and shielded (SD) lambda over two dipole (f). The coordinate system is indicated on the bottom right. Tuning and matching is accomplished via RF ports in the network simulation for all elements.

Modelling and simulations using the finite integration technique were performed in CST Microwave Studio (CST AG, Darmstadt, Germany). Six different RF element types were investigated (Figure 3.1). In the following, left-right is considered to be the x-direction, up-down is referred to as the y-direction, and the z-direction is aligned with the main magnetic field (see Figure 3.1).

The first element type is a rectangular loop (Figure 3.1a) with 200 mm length in z-direction, 100 mm in x-direction, 0.1 mm thickness in y-direction and chamfered edges. Six capacitors are equally distributed around the loop, with five modelled as lumped elements and the remaining capacitor modelled as the RF port used for excitation in the network simulation (CST Design Studio).

Micro stripline (MSL) elements (Figure 3.1b) have a length of 250 mm in z-direction and a width of 100 mm in x-direction. The top plane and the ground plane (Rogers 4003C carrier substrate, $\epsilon_r = 3.35$, $\tan\delta_{\text{electric}} = 0.0027$) have a thickness of 0.8 mm and a separation of 18.4 mm in y-direction. Conducting parts are modelled as 35 μm cladding (perfect conductor), and identical capacitors ($C_{\text{end}} = 2.6 \text{ pF}$) bridge the 3.5 mm gaps between the top and ground planes at both ends of the element. Central feeding via two RF ports is achieved centrally on the ground plane and simulated in the network simulation using a $\lambda/2$ balun (RG223 cable modelled as transmission line, velocity factor = 0.66, attenuation = 0.23 dB m^{-1}) and a matching network (23) with two identical parallel capacitors and one series capacitor.

Meander elements (ME) are based on the MSL but with meander structures (65 mm in x-direction, 2 mm spacing, 2 mm width) introduced at both ends on the top plane (Figure 3.1c). Near the meander structures the meshing is refined to 0.5 mm. Since the meanders increase the electrical length of the two legs, the capacitors C_{end} were reduced to 1 pF to optimize the current distribution.

By increasing the meander size to 100 mm in x-direction the capacitors at both ends can be removed (Figure 3.1d), and the element represents a SDM.

In comparison to the dipole structures which are often shortened for 7T applications (24,25), in this work we investigate a $\lambda/2$ dipole with a length of 466 mm and a centrally located RF port for excitation (Figure 3.1e).

The last element (Figure 3.1f) is a shielded lambda over two dipole (SD) with central feeding identical to the MSL, ME and SDM.

All capacitors used for these six element types included a corresponding equivalent series resistance (ESR) depending on their capacitance to incorporate loss mechanisms. The capacitors are based on the C17 series (Voltronics Corporation, Denville, NJ, USA) with values of e.g. $Q = 4000$ for 1.8 pF and $Q = 190$ for 56 pF at 297 MHz. The formula for the equivalent series resistance

ESR = $(\omega CQ)^{-1}$ and the fit parameters of a power function $Q = a \cdot C^b$ to the values of Q and C from the datasheets ($a = 6588$, $b = -0.8475$) was used to derive the ESR for the capacitors in the simulations. Consequently, the values for the capacitors used from 1 pF to 45.5 pF yielded ESR values in the range 0.08 to 0.045 Ω , respectively.

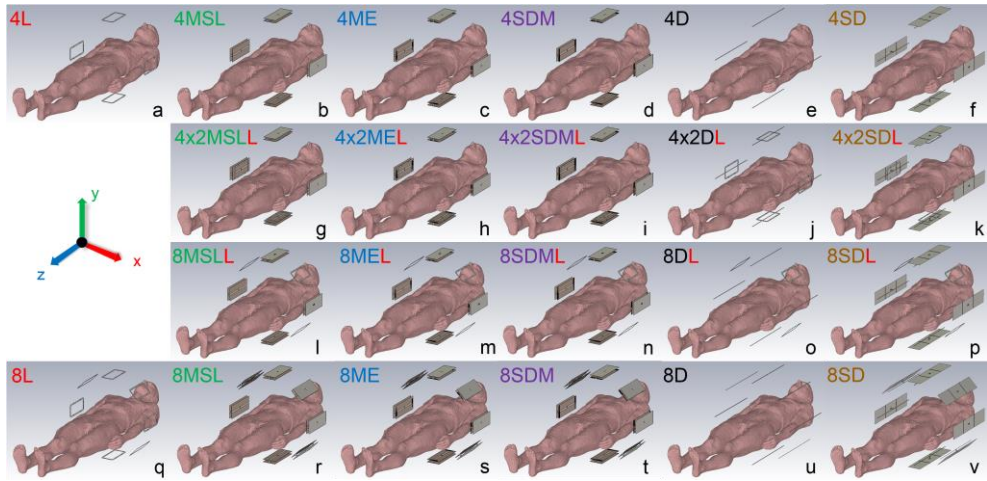


Figure 3.2: The four investigated array topologies with four identical elements (a-f), a hybrid of four loops and four other elements of one type (g-k) where elements of different types are located at the same position, a hybrid of four elements of one type combined with four loops in between (l-p) termed an interleaved design, and eight identical elements (q-v) combined on a circumferential ring. Consequently, 22 different remote RF coil arrays were simulated using the body model Duke (26) as load. Please note the abbreviations in the top left of each subfigure.

Four different RF array topologies were simulated (Figure 3.2). Figures 3.2a-f show the first array design featuring four identical elements. The second design (Figures 3.2g-k) is a combination of four loops and four elements of another position (MSL, ME, SDM, dipole, SD) with different elements located at the same position. The third design (Figures 3.2l-p) combines four loops and four elements of

another kind in an interleaved arrangement. The fourth design included eight identical elements (Figures 3.2q-v) circumferentially arranged in a single ring. These 22 arrays were loaded with the body model Duke (70 kg, 174 cm, 2 mm isotropic voxel size) from the Virtual Family (26). Figure 3.2 includes abbreviations for further use.

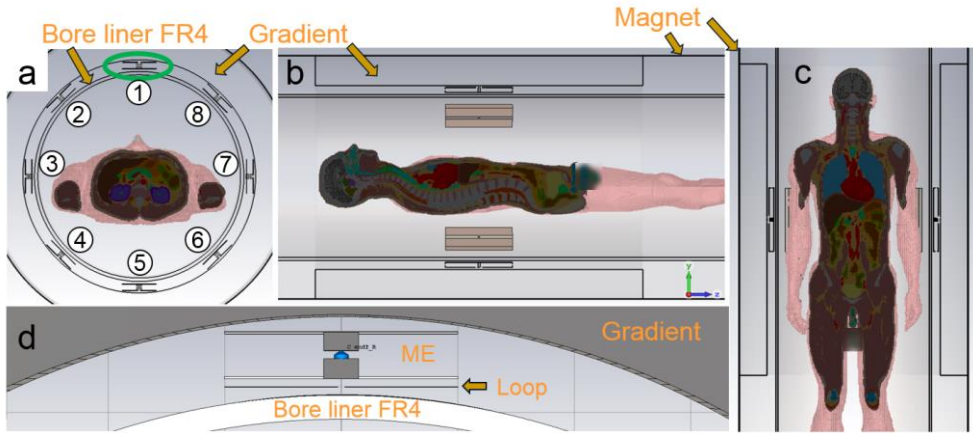


Figure 3.3: Central transversal (a), sagittal (b), and coronal (c) slices of the simulation setup. The body model is oriented along the z-direction and centered on the kidney region (a). RF coil elements (green) are located between the bore liner (FR4 material, $\epsilon_r = 4.3$, $\tan\delta_{\text{electric}} = 0.025$, thickness 10 mm, 60 cm inner diameter) and the gradient coil (a-c), which is modelled as a perfect electric conductor (1 m length in z-direction) and thus forms a shield for the array. To model the magnet itself, an additional circumferential perfect electric conductor (2 m length in z-direction) surrounds the gradient shield (b,c). Close proximity between the arms and the coil elements can be appreciated (c). The space between bore liner and gradient coil is limited to 34 mm and the distance of the elements to the bore liner is 7 mm except for the loops, for which the distance is 3.5 mm (d).

Figure 3.3 shows the central transversal (A), sagittal (B) and coronal (C) slices of the simulation setup. The body model is centered on the kidney region (A). Figures 3.3b,c show the gradient shield (1 m in z-direction) that is enclosed by the magnet (2 m in z-direction). Both are modelled as perfect electric conductors and

act as shields for the array. Absorbing boundaries around the magnet terminate the simulation domain in all directions.

Power Balance

Power distribution depends on the excitation vector (27). For a comparison among the different RF arrays, the circular polarized mode (CP*) was evaluated, i.e. a 90° phase offset was applied to the excitation signals of the ports for four element arrays and 45° for eight elements. Furthermore, a dedicated phase-only shim was calculated for an oval (5.3 cm in x-direction, 3.4 cm in y-direction) between the kidneys in transversal orientation. In the CST simulations the power balance (Figure 3.4) can be extracted as follows. A portion of the external applied power P_{External} is lost due to inter-element coupling and a very small amount of reflection (below 1% if $S_{11} < -20$ dB). Parts of the stimulated power $P_{\text{Stimulated}}$ is dissipated in the ESR of capacitors used in the tuning and matching network. The rest, P_{Accepted} , goes to the simulation domain and can be subdivided into radiated power and volume losses. Volume losses can be power dissipated in the body model, the ESR of lumped elements, the bore liner, or the element substrate (Rogers 4003C). An aim of RF array construction is to minimize coupling between elements, radiation, material losses and losses in capacitors and to allow the power to be used for spin excitation in the subject under examination (body model).

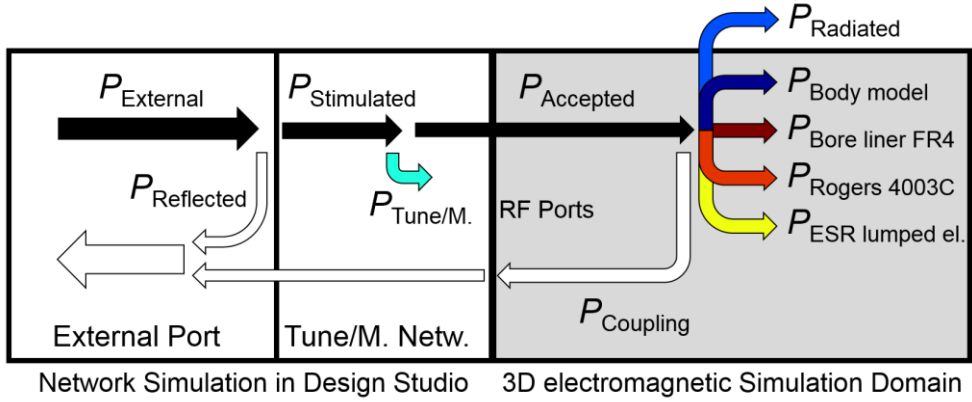


Figure 3.4: Illustration of the power balance in CST. The difference between the externally applied power P_{External} and the stimulated power $P_{\text{Stimulated}}$ corresponds to the losses due to coupling and reflection. A specific portion $P_{\text{Tune/m}}$ of $P_{\text{Stimulated}}$ is dissipated in the ESR of capacitors used for tuning and matching. The remaining power P_{Accepted} is fed into the simulation domain via RF ports, where it can be lost due to radiation (P_{Radiated}), volume losses, or losses in the ESR of lumped elements ($P_{\text{ESR Lumped el.}}$). Volume losses can be subdivided into losses in the body model ($P_{\text{Body model}}$), bore liner ($P_{\text{Bore liner}}$), and substrate material ($P_{\text{Rogers 4003C}}$).

Cumulative Sum of Singular Values

To evaluate the DOFs within the complex B_1^+ transmit fields, an approach based on the investigations in the work by Guérin et al. (10) was utilized. The complex B_1^+ transmit fields of the N transmit channels were reshaped to form a column vector with P entries (where P is the number of pixels) and those column vectors were then concatenated to an $N \times P$ matrix that was subjected to singular value decomposition. After normalizing the resulting singular values to the highest value, the cumulative sum of the N singular values was plotted in descending order of the values as a measure for the DOFs within the input data. If the individual channels are totally independent, the cumulative sum of the normalized singular values would be equal to the total number of channels N . If the patterns

provided by the N individual channels are not independent, the cumulative sum C is lower than N and the array effectively only provides C independent channels and, thus, it provides only limited DOFs for RF manipulation in pTx applications, e.g. for RF shimming etc. In contrast to reference (10) where the 3D B_1^+ transmit fields were investigated, in this work the cumulative sum of singular values is evaluated for single central slices in transversal, sagittal and coronal orientation.

Voxelwise Power Efficiency

To evaluate the power efficiency a total peak power of 8 kW was used. This power was equally distributed among the available RF channels. Then, the maximum achievable B_1^+ amplitude for each voxel in the central slices on an isotropic 128x128 grid was calculated by summing the absolute values of the B_1^+ of each RF channel. In this way it is possible to investigate the maximum amplitude in the slices and compare each voxel for the different RF arrays.

Voxelwise SAR Efficiency

In order to evaluate the SAR efficiency, first the local SAR averaged over 10 g (28) was calculated (averaging method: IEEE/IEC 62704-1) for all simulations. Then, these SAR matrices were compressed using the virtual observation point (VOP) method (28) with a maximum SAR overestimation of 5%. These VOPs and the B_1^+ fields (isotropic 128x128 grid) were subsequently imported into Matlab (The MathWorks, Inc., Natick, MA, USA) for further processing. In Matlab, 60 RF shims were calculated (2x Intel Xeon X5690, 12 cores in total) for each voxel (19) in the central slices using non-linear optimization (Nelder-Mead simplex search method) with arbitrary starting points in order to maximize the SAR efficiency ($B_1^+ \cdot \max(\text{SAR}_{10g})^{-0.5}$). To compare the performance among the arrays, a voxelwise comparison was performed as was done for the voxelwise power efficiency. For

the calculation of the RF shims in the three orthogonal central slices, the arms of the body model were excluded from the ROI. However, the utilized VOP data set still included VOPs located in the arms.

3.2 Results

Simulation

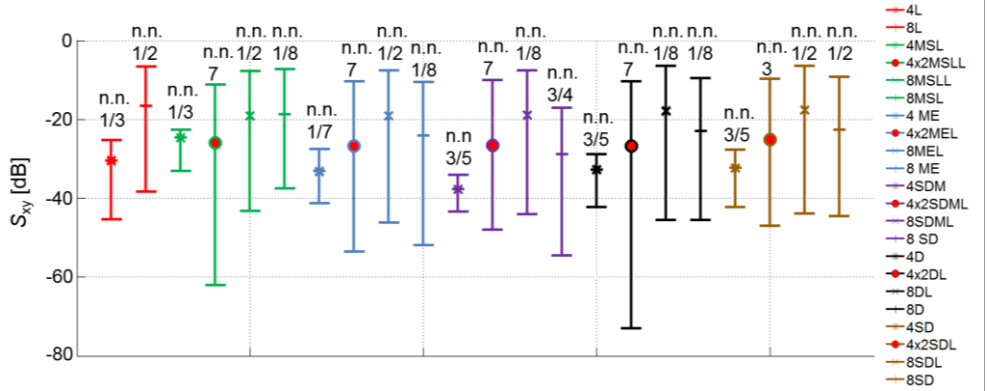


Figure 3.5: Average coupling values S_{xy} for the 22 simulated remote coil arrays. Minimum and maximum values are indicated by the error bar. The position (see Figure 3.3a) of the two elements with the highest coupling is shown above the error bar, indicating whether or not this coupling was between next neighbors (n.n.) in the array. For all element types, arrays with four identical elements perform better than arrays with eight identical elements regarding average and maximum coupling values. Combined arrays with four loops and four elements of another kind with the 4x2 design show comparable (ME), lower (MSL, dipole and SD), or higher (SDM) coupling than their counterparts with eight identical elements. Combined arrays in interleaved design show higher coupling values in comparison to the 4x2 design and also higher coupling values in comparison to the arrays with eight identical elements (except for the 8MSL and 8L arrays).

Simulations using the finite integration technique in CST were performed on a high performance computing cluster employing four Nvidia Tesla M2090 (Santa Clara, CA, USA) graphic units for distributed computing. On average 80 million mesh cells were used which necessitated a computation time of about 14 hours (2 ports in parallel) for simulation of each of the 22 RF array configurations. All elements in all RF arrays could be tuned and matched to achieve a matching S_{11} of better than -20 dB at 297 MHz. Figure 3.5 shows the average coupling S_{xy} for the 22 arrays. As can be seen, arrays with four identical RF elements always provide

lower average coupling when compared to corresponding arrays with eight identical RF elements of the same element type. The higher coupling is evidently due to the smaller element spacing in the eight-element arrays and is especially prominent for loops, whereas it is least prominent for shielded dipoles. Even more severe is the increase of the maximum coupling S_{xy} from four to eight elements, which can be observed for all element types. In general, maximum coupling values are present between next neighboring (n.n.) elements in the investigated arrays (positions are indicated in Figure 3.3a). The maximum coupling in the arrays with eight identical elements and in the interleaved design is predominantly present between the upper elements, which are most distant from the body model. For combined RF arrays of loops and other element types in the 4x2 design, the maximum values are present between the element pairs near the arms. The performance of these arrays regarding mean and maximum coupling is better compared to the array with eight identical elements except for shielded dipoles with meanders (8SDM) and loops (8L). Arrays with the interleaved design show increased coupling compared to the 4x2 design and also increased coupling when compared to eight identical elements except for 8L and 8MSL. Overall, the average values are predominantly below -20 dB, while maximum values can be above -10 dB for eight-element arrays.

Power Balance

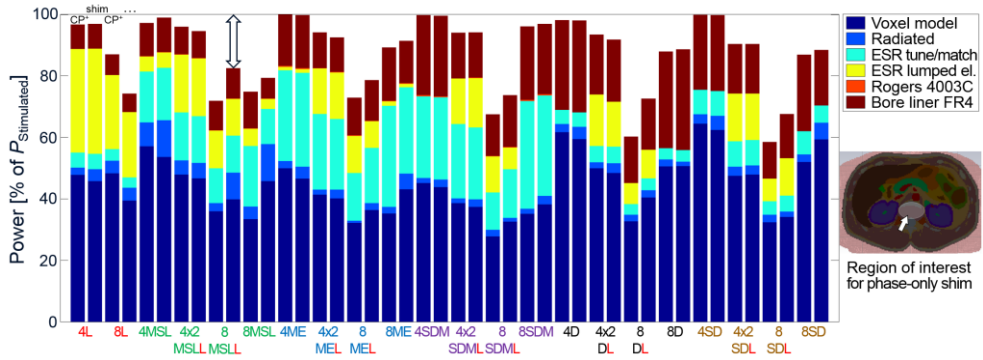


Figure 3.6: Power balance for the CP+ mode and the phase-only shim weights for each of the 22 arrays indicating the percentage distribution of the stimulated power. The difference between the top of the bar and 100% (double-ended arrow) is lost due to inter-element coupling and reflection. Power can be dissipated in the bore liner (especially for dipoles), in the tuning/matching network (especially ME and SDM), radiated (maximum for MSL arrays with about 10%), or lost in lumped elements (especially loops). Even though the losses are unevenly distributed, in all cases between 40% and 60% of the power is dissipated in the body model where it can be used for spin excitation. The difference between CP+ mode and the phase-only shim weights is small, especially for arrays with low losses due to coupling while for arrays in the interleaved design the difference is more remarkable. Interestingly, the CP+ mode performs better for the 8L array, while the phase-only shim performs better for all other interleaved arrays.

Figure 3.6 depicts the power balance for the simulated RF arrays for the CP+ mode and the phase-only shim weights. The maximum of 100% on the y-axis represents the full stimulated power, and the difference to the top of the colored bar is the amount of power that is lost due to inter-element coupling and the comparably small amount of reflection. Depending on the RF element type, up to 30% of the power is lost in the bore liner. The rest is dissipated in the lumped elements, capacitors in the tuning and matching network, radiated, or absorbed in the body model. The losses in the substrate Rogers 4003C can basically be neglected. Arrays with only MSL elements show highest radiation ($\approx 10\%$). On the

one hand, loops have high losses in the capacitors, which can also be seen in the arrays featuring a combination of loops and other element types. On the other hand, comparably low losses due to radiation or power dissipation in the bore liner or the tuning/matching network can be observed in loop-only arrays. Arrays with ME and SDM have high losses ($\approx 30\%$) in the tuning/matching network. Even though the losses are quite unevenly distributed, the power going to the body model is quite similar in all cases: between 40% and 60% is dissipated in the body model. Arrays with only four elements in general show low losses due to coupling independent of the excitation mode, and the difference between CP⁺ mode and the phase-only shim weights is comparably small. Higher differences between the two shim modes can be observed for eight-element arrays with the interleaved design.

Cumulative Sum of Singular Values

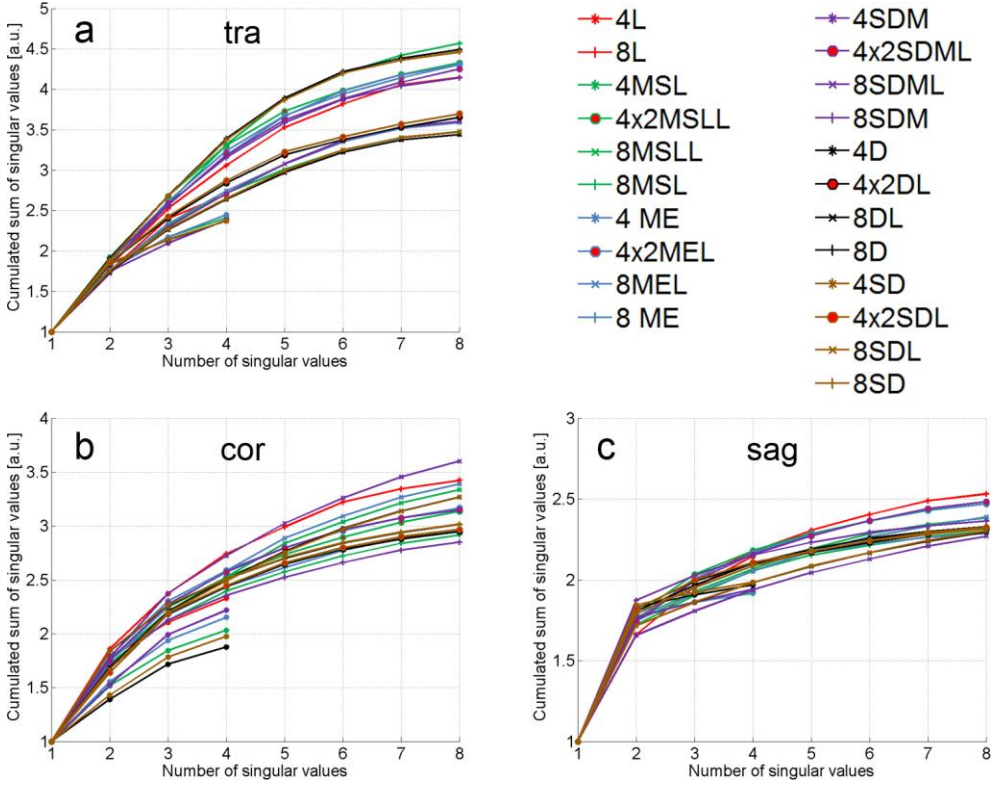


Figure 3.7: Cumulative sum of singular values for the three central slices. In the central transversal slice (a) the 8MSL array features maximum DOFs followed by the 8D and the 8SD array. In coronal orientation (b) the maximum values are reduced and only the 8SDM array reaches a sum of 3.5. Similar behavior can be observed in the sagittal orientation (c), where only values of 2.5 are achieved by the 8L array. Consequently, the encoding capabilities are optimum in the transversal slice followed by the coronal and the sagittal orientations.

In the following investigations the volume of interest was limited to a 40x40x40 cm field of view excluding the arms. Figure 3.7 shows the cumulative sum of singular values obtained from the B_1^+ maps (see Supporting Figures 3S1-S6). Depending on the arrays' DOFs, the subsequent singular values add an amount that is almost 1 (for independent transmit fields) or close to 0 (basically

no additional contribution by adding another transmit channel). Toward higher numbers of singular values, the cumulative sum saturates. In the central transversal slice (Figure 3.7a), the 8MSL array has the highest cumulative sum of singular values (about 4.5) followed by the 8D and 8SD arrays. In the central coronal slice (Figure 3.7b), the maximum values decrease for all the arrays, and the maximum cumulative sum of about 3.5 is achieved by the 8SDM array. This means that the encoding capabilities for all the arrays are higher for the central transversal slice and reduced in the coronal plane. These values are again decreased if the central sagittal plane (Figure 3.7c) is investigated. Here, the 8L array performs best but it only reaches a value of about 2.5. As can be seen for all three planes, in no case is a four-element array able to achieve performance equal to the worst eight-channel array except for four loops in the central sagittal plane.

Voxelwise Power Efficiency

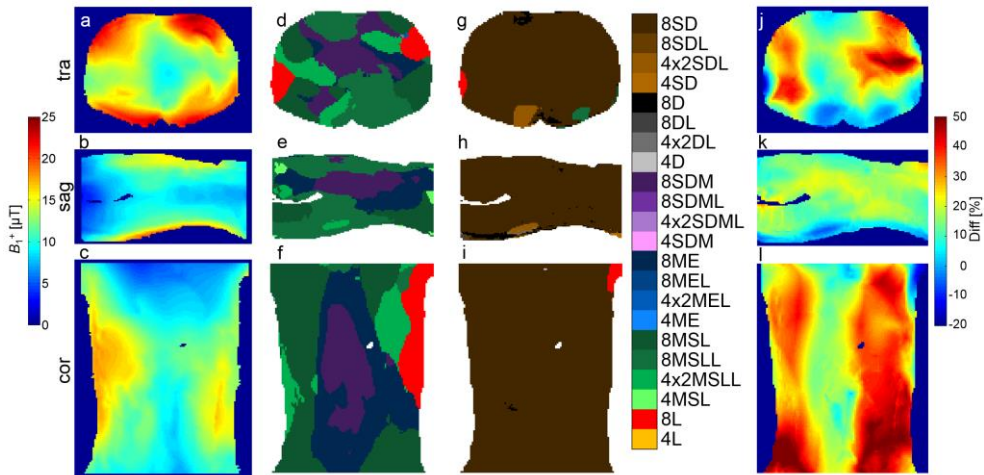


Figure 3.8: Power efficiency in the central slices (transversal top row, sagittal mid row, coronal bottom row) for 8 kW peak power distributed equally among the channels of the 8D array (a-c). If the arrays are compared pixelwise excluding dipoles and shielded dipoles (d-f), the 8SDM array performs best in the center. In

the surrounding regions the 8ME array seems preferable while the border regions are dominated by MSL arrays. If dipole arrays are included (g-i), it becomes obvious that the 8SD array is most power efficient in this context. Yet, the 8D array shows almost the same performance with values only about 2% less than the 8SD array. The last column (j-l) quantifies by how much the 8SD array outperforms the second-best array (excluding the 8D array) if the 8SD is the best-performing array (positive values) or by how much 8SD underperforms the best array (negative values). Scales in all figures are cropped.

Investigations of the voxelwise power efficiency under a realistic power budget of 8 kW are depicted in Figure 3.8. The results in the three central slices are shown in Figures 3.8a-c for eight dipoles. While in the border regions up to 25 μT can be achieved, in the center values of 10 μT are possible. Also, it can be observed that the power efficiency drops slowly toward the end of the field of view in z-direction but heavily toward the center of the body. Furthermore, the influence on the power efficiency in the torso due to the arms can be appreciated especially in the transversal orientation (Figure 3.8a), where the power efficiency is comparably low on the right and on the left side of the torso. Figures 3.8d-f indicate which RF array configuration is superior when comparing the arrays pixel-wise in the three central slices if dipole arrays are not considered. The 8SDM array performs best in the central region in transversal orientation followed by the 8ME array in the surrounding regions. MSL arrays dominate the outer regions in all orientations. Some regions are also dominated by the 4MSL array. This is possible since arrays with four elements have 2 kW per channel available.

If dipole arrays are included in the comparison (Figures 3.8g-i), it becomes obvious that the 8SD array is most power efficient in this context. However, it is closely followed by the 8D array which shows very comparable behavior and on average achieves values of only 2% less. Figures 3.8j-l indicate quantitatively how much more power efficient 8SD are compared to the second-best performing array in each voxel. Here, the 8D array which is basically similar to the 8SD array is excluded. In areas in which a positive percentile value is displayed, the 8SD array is accordingly better and in areas in which a negative percentile value is displayed,

the 8SD array is worse compared to the best performing array. In the transversal orientation, the 8SD array on average performs 19.0% better than the next best array, in the sagittal orientation this value is 13.9%, and in the coronal orientation it is 29.0%. If the best and the worst array are compared, the average factor of max/min is 2.88 in the transversal, 3.97 in the sagittal, and 3.19 in the coronal orientation.

Voxelwise SAR Efficiency

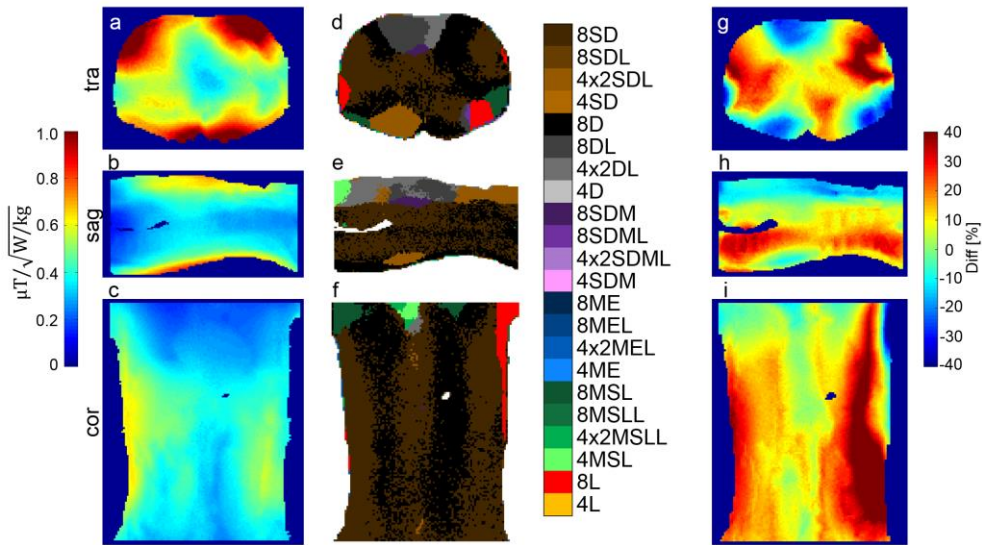


Figure 3.9: Results of the voxelwise SAR efficiency for the 8D array (a-c). Each pixel in the central transversal (a), sagittal (b), and coronal (c) planes represents one shim with optimized SAR efficiency for this pixel. As can be seen, the SAR efficiency is lower in the center of the body model (a). If all arrays are compared (d-f), the 8D and the 8SD array show the highest SAR efficiency in most of the areas, especially in the center of the body model. The right column (g-i) shows by how much the 8SD array outperforms the second-best array (excluding the 8D array) if 8SD are the best performing array (positive values) or by how much 8SD underperform the best array (negative values). Scales in all figures are cropped.

Due to the increased complexity of more elements for the non-linear optimization, the calculation time was about 20 hours for arrays with eight elements and 5 hours for arrays with four elements for a single orientation. Results of the voxelwise SAR efficiency are presented in Figure 3.9. The first column (Figure 3.9a-c) shows the calculated voxelwise SAR efficiency for the 8D array. As can be seen, a qualitative comparison to the results for the voxelwise power efficiency (Figure 3.8a-c) is possible. The voxelwise SAR efficiency drops quite heavily toward the center, which seems reasonable since high B_1^+ in the center might go along with high local SAR values in the outer regions.

Again, the performance among the arrays was compared (Figure 3.9d-f). In most of the areas of the central transversal slice (Figure 3.9d), 8SD and 8D achieve the maximum voxelwise SAR efficiency. This is especially important in the center of the body where deep-lying organs and structures are located. The arrays 8SD and 8D also show the best performance throughout large regions in the coronal and sagittal planes, which may be explained by the geometrical length. Toward the border regions in z-direction, RF arrays with MSL elements perform best.

Intuitively, arrays with four elements should not be able to perform best in any region since every such excitation could also be applied by an eight-element array of the same elements. Yet, this is only true in the absence of coupling between individual RF elements. As soon as coupling is regarded, arrays with four elements can outperform arrays with eight elements in a specific region.

Figure 3.9g-i indicates quantitatively how much more SAR-efficient the 8SD array is in comparison to the next-best array (same approach as performed for the voxelwise power efficiency above) again with the 8D array excluded. This makes sense since 8D and 8SD perform very similar in the context of this investigation. On average the 8SD array is only 0.35% more SAR efficient than the 8D array in this voxelwise comparison. In the transversal orientation, the 8SD array on average performs 7.7% better than the next-best array (excluding the 8D array), in the sagittal orientation this value is 7.1%, and in the coronal orientation it is

15.6%. Comparing the best and the worst array (8D array included) yields an average factor of 3.04 (max/min) in the transversal, 4.07 in the sagittal, and 4.05 in the coronal orientation.

To quantify the convergence, the percentage difference for each pixel between the final value and the next-to-last value for each of the 60 shims was calculated. The worst case value was 6.7% in transversal, 6.0% in coronal, and 7.2% in sagittal orientation. These values can explain why noisy regions can occur when one array starts to outperform the other (e.g. Figure 3.9f in the center). The values averaged for arrays with eight elements are 0.44% in transversal, 0.46% in coronal, and 0.44% in sagittal orientation, while they are below 0.01% for arrays with four elements in all orientations. It should be noted that in addition, the VOP compression intrinsically can lead to a 5% overestimation of the SAR in these investigations.

3.3 Discussion

All investigated RF transmit arrays with eight elements show high coupling between elements if they are compared to close-fitting arrays such as a close-fitting array with eight ME (12), which achieves an inter-element coupling below -20 dB. No additional decoupling approaches were investigated in this work, as it would be desirable to find an element and RF transmit array configuration that is intrinsically well decoupled. First, this target is reasonable due to the additional effort (construction time, space, error-proneness, and cost) necessary for practical implementation of decoupling networks. Second, decoupling networks can impede power efficiency to a certain extent simply because power is dissipated in the associated networks and these power losses reduce the impact of lower inter-element coupling.

Investigations of the power balance for the CP⁺ mode and the phase-only shim weights revealed several interesting aspects of the remote coils' loss mechanisms. The losses for the different arrays are unevenly distributed. Power dissipated in the bore liner is increased for element types with increased conductor length (dipoles and SD > SDM > ME > MSL). Loops have the lowest loss in the bore liner. This could be explained by the distribution of capacitors along the element which lead to a homogeneous current distribution and reduced peak E-fields. ME and SDM have especially high losses in the tuning/matching network that could be reduced by using transmission lines for tuning and matching. The losses in the capacitors along the loops could be reduced by capacitors with even lower losses or by changing the number of capacitors.

The results can also serve as starting point to improve the power efficiency, e.g. for ME and SDM elements by changing their design. Yet, these investigations of the power balance only include two shim modes, and with other excitation vectors the behavior might theoretically change.

As expected, the eight-element arrays perform better concerning the cumulative sum of singular values compared to the four-element arrays. Also, the decreasing performance from transversal to coronal and finally sagittal orientation seems plausible. The results from (10) indicate that arrays with more DOFs show a trend to better performance, which can justify the employment of the cumulative sum of singular values to compare arrays; nevertheless, it should be noted that the ultimate performance (e.g. concerning excitation fidelity) depends on the exact final configuration concerning both application and pulse sequence.

The results from the voxelwise power efficiency investigations match the investigations of the power balance distribution for the CP⁺ mode. Arrays with dipoles dissipate most of the power in the body model and this consequently can explain the high voxelwise power efficiency. Overall, the 8SD array performs best in the context of this evaluation. The results show that the power is not dissipated locally but over the entire extent of the chosen FOV, which allows a high voxelwise power efficiency for the 8SD and 8D arrays in most of the evaluated regions. Especially in the center of the body, this is important for imaging deep-lying organs.

Observations that MSL arrays radiate a high amount of power on the one hand and that the voxelwise power efficiency of MSL arrays in regions that are most distant in z-direction from the center is high, on the other hand, fit well to each other. The power that is radiated toward the end of the bore can partly still be used for spin excitation in the outer regions in z-direction. The high power efficiency even in the border regions in z-direction of the 40-cm FOV also fits first experimental results from reference (19) where MR images with 50 cm FOV in z-direction are demonstrated.

Concerning SAR efficiency, the 8SD array is again are most favorable in the context of these investigations. Yet, the differences are less prominent compared to the voxelwise power efficiency. Reducing the losses in the bore liner and in the

tuning/matching network might make other RF arrays like the 8ME or 8SDM array more favorable. In comparison to the estimated measurement for the convergence, the differences among the arrays are comparably high in most of the regions. This supports confidence in the way the comparison is performed in the first place. An interesting point is that the difference between the best and the worst performing array is higher for SAR efficiency than it is for power efficiency in all orientations, while the dominance of the 8SD array is less for SAR efficiency than for power efficiency. A voxelwise comparison for both SAR and power efficiency is independent of the final pTx application, which in principle allows a general comparison of the RF arrays.

Two of the six elements types investigated (loops and dipoles) do not have their own RF shield and only the gradient shield acts as a shield for these elements, while the other four element types (MSL, ME, SDM, SD) have a ground plane as RF shield in addition to the gradient coil. This might influence the energy stored in the system and thus impact the power balance and power efficiency, while the impact was lower than expected between the 8D and the 8SD array. Also, it would be difficult in a real implementation to tune and match an array with loops or dipoles without an additional shield outside of the magnet. Additionally, cables that were neglected in these simulations would also be a source of possible problems since shield currents could occur. Furthermore, an implementation without a shield fixed to the individual RF elements themselves might prove difficult, since the distance between elements and gradient shield can vary due to technical difficulties in mounting the array in the exact center of the gradient coil.

3.4 Conclusion

In this work 22 remote RF coil arrays were investigated. Six different RF coil elements, namely loops, MSL, ME, SDM, dipoles and SD were combined to form four different array topologies, the first consisting of four identical elements, the second of four loops and four other elements of a single type in a 4x2 design, the third of four loops and four other elements in an interleaved design, and the fourth of eight identical elements, all arranged on a circumferential ring. The results indicate that the 8SD array is most power and SAR efficient in the context of the investigations. Also, as the evaluation of the cumulative sum of singular values showed, they feature high encoding capabilities (DOFs) in the transversal central plane. In the absence of additional decoupling methods, coupling was found to be a problem for all arrays with eight elements; thus, investigations of decoupling strategies could be a field of further research, although it should be noted that decoupling networks could impede power balance and efficiency. Even if the 8SD array seems to be preferable, this element type would make the construction and practical implementation of multi-ring RF transmit arrays difficult due to their long physical length at 7T. Consequently, it could be constructive to investigate modifications of ME or SDM to make them more power and SAR efficient, since these element types are much smaller in the z-direction and thus allow for a higher element density in highly parallel transmit arrays with multiple rings.

Acknowledgements

The authors wish to thank Thomas Fiedler from the DKFZ Heidelberg, Germany for his support. The research leading to these results has received funding from the European Research Council under the European Union's Seventh Framework Programme (FP/2007-2013) / ERC Grant Agreement n. 291903 MRexcite.

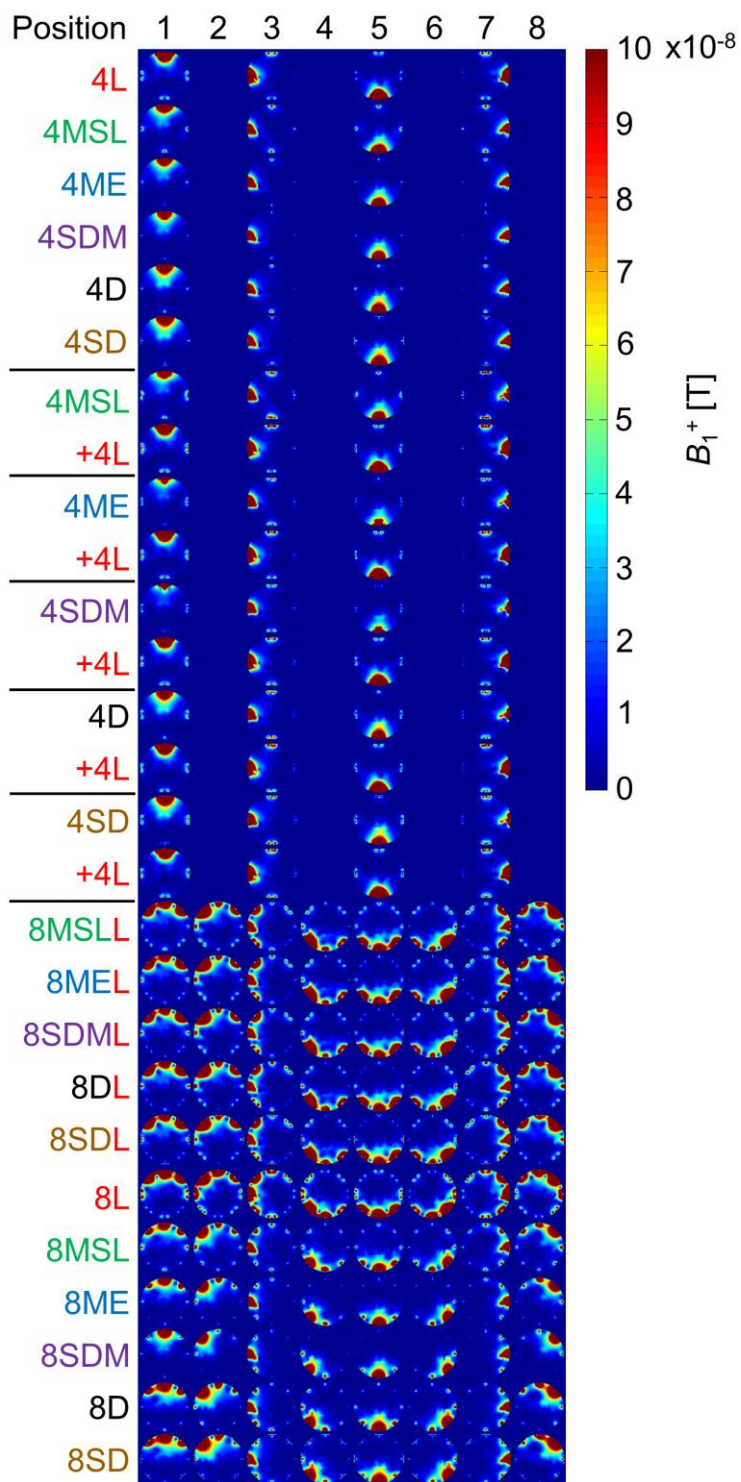
References

1. Hoult DI, Phil D. Sensitivity and Power Deposition in a High-Field Imaging Experiment. *J Magn Reson Imaging* 2000;67:46–67.
2. Wiesinger F, Boesiger P, Pruessmann KP. Electrodynamics and ultimate SNR in parallel MR imaging. *Magn Reson Med* 2004;52(2):376–90.
3. Ohliger MA, Grant AK, Sodickson DK. Ultimate intrinsic signal-to-noise ratio for parallel MRI: electromagnetic field considerations. *Magn Reson Med* 2003;50(5):1018–30.
4. Vaughan JT, Snyder CJ, DelaBarre LJ, Bolan PJ, Tian J, Bolinger L, Adriany G, Andersen P, Strupp J, Ugurbil K. Whole-body imaging at 7T: preliminary results. *Magn Reson Med* 2009;61(1):244–8.
5. Collins CM, Liu W, Swift BJ, Smith MB. Combination of optimized transmit arrays and some receive array reconstruction methods can yield homogeneous images at very high frequencies. *Magn Reson Med* 2005;54(6):1327–32.
6. Mao W, Smith MB, Collins CM. Exploring the limits of RF shimming for high-field MRI of the human head. *Magn Reson Med* 2006;56(4):918–22.
7. Katscher U, Börnert P, Leussler C, van den Brink JS. Transmit SENSE. *Magn Reson Med* 2003;49(1):144–50.
8. Grissom W, Yip C, Zhang Z, Stenger VA, Fessler JA, Noll DC. Spatial domain method for the design of RF pulses in multicoil parallel excitation. *Magn Reson Med* 2006;56(3):620–9.

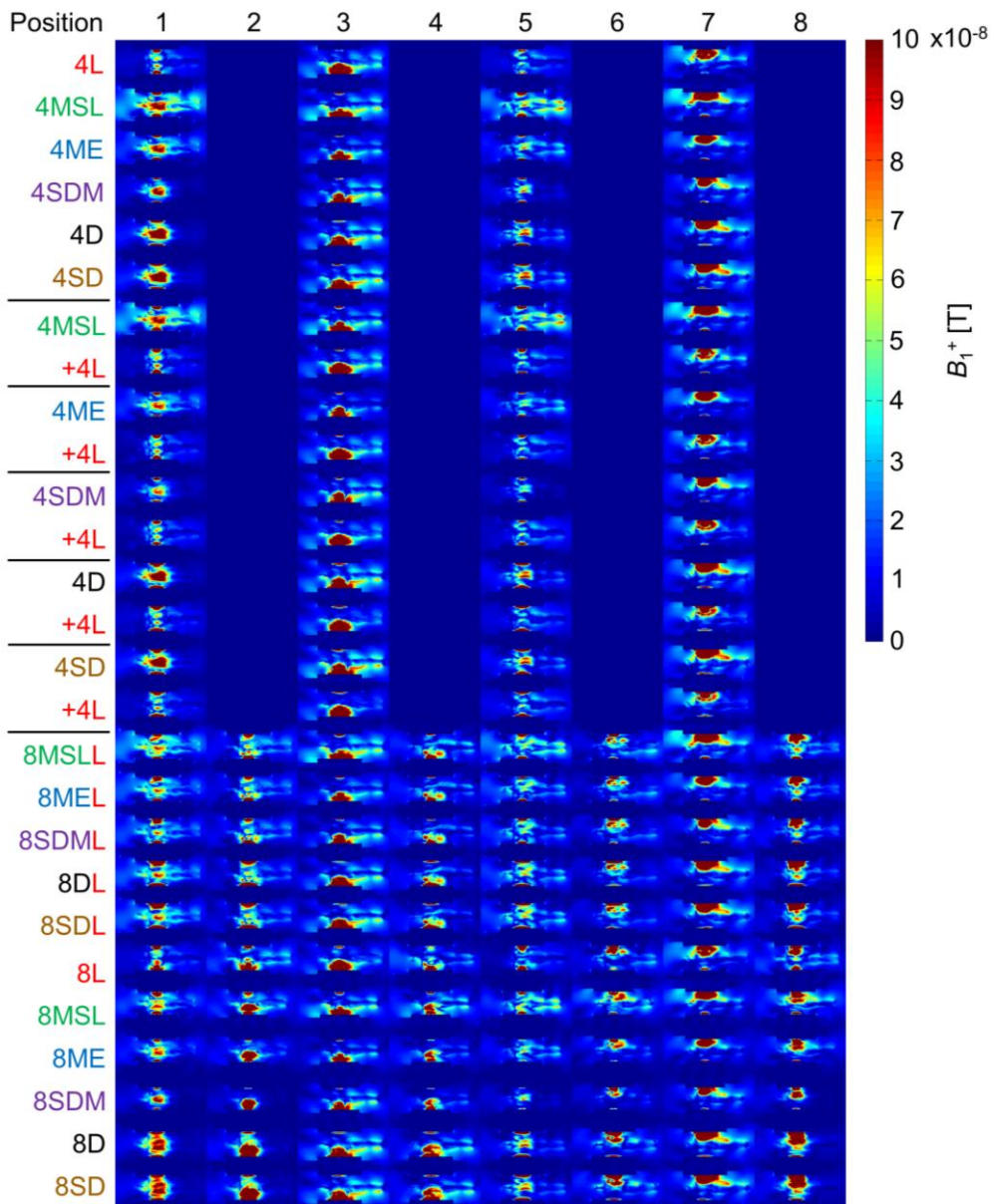
9. Orzada S, Maderwald S, Poser BA, Bitz AK, Quick HH, Ladd ME. RF excitation using time interleaved acquisition of modes (TIAMO) to address B1 inhomogeneity in high-field MRI. *Magn Reson Med* 2010;64(2):327–33.
10. Guérin B, Gebhardt M, Serano P, Adalsteinsson E, Hamm M, Pfeuffer J, Nistler J, Wald LL. Comparison of simulated parallel transmit body arrays at 3 T using excitation uniformity, global SAR, local SAR, and power efficiency metrics. *Magn Reson Med* 2014;73:1137–50.
11. Metzger GJ, Snyder C, Akgun C, Vaughan T, Ugurbil K, Van de Moortele P-F. Local B1+ shimming for prostate imaging with transceiver arrays at 7T based on subject-dependent transmit phase measurements. *Magn Reson Med* 2008;59(2):396–409.
12. Orzada S, Quick HH, Ladd ME, Bahr A, Bolz T, Yazdanbakhsh P, Solbach K, Bitz AK. A flexible 8-channel transmit/receive body coil for 7 T human imaging. *Proc Intl Soc MRM* 17 2009;2999.
13. Aussenhofer SA, Webb AG. An eight-channel transmit/receive array of TE01 mode high permittivity ceramic resonators for human imaging at 7T. *J Magn Reson Elsevier Inc.*; 2014;243:122–9.
14. Graessl A, Renz W, Hezel F, Dieringer M a, Winter L, Oezerdem C, Rieger J, Kellman P, Santoro D, Lindel TD, et al. Modular 32-channel transceiver coil array for cardiac MRI at 7.0T. *Magn Reson Med* 2014;72(1):276–90.
15. Rosenkrantz AB, Zhang B, Ben-eliezer N, Nobin J Le, Melamed J, Deng F, Taneja SS, Wiggins GC. T2-Weighted Prostate MRI at 7 Tesla Using a Simplified External Transmit-Receive Coil Array : Correlation With Radical

- Prostatectomy Findings in Two Prostate Cancer Patients. 232(2015):226–32.
16. Umutlu L, Maderwald S, Kinner S, Kraff O, Bitz AK, Orzada S, Johst S, Wrede K, Forsting M, Ladd ME, et al. First-pass contrast-enhanced renal MRA at 7 Tesla: initial results. *Eur Radiol* 2013;23(4):1059–66.
 17. Hahnenmann ML, Kraff O, Orzada S, Umutlu L, Kinner S, Ladd ME, Quick HH, Lauenstein TC. T1-Weighted Contrast-Enhanced Magnetic Resonance Imaging of the Small Bowel. *Invest Radiol* 2015;50(8):539–47.
 18. Lazik-Palm A, Kraff O, Johst S, Quick HH, Ladd ME, Geis C, Körsmeier K, Landgraeber S, Theysohn JM. Morphological and Quantitative 7 T MRI of Hip Cartilage Transplants in Comparison to 3 T—Initial Experiences. *Invest Radiol* 2016;51(9):552–9.
 19. Orzada S, Bitz AK, Gratz M, Johst S, Völker MN, Kraff O, Beyer D, Mathiebe T, Abuelhaija A, Solbach K, et al. An integrated 8-channel Tx / Rx body coil for 7 Tesla whole-body MRI. *Proc Intl Soc MRM* 23 2015. p. 630.
 20. Flöser M, Bitz AK, Orzada S, Solbach K, Ladd ME. Comparison of Local and Remote Transmit Arrays for Body Imaging at 7T under Power and Local SAR Constraints. *Proc Intl Soc MRM* 23 2015;550.
 21. Orzada S, Maderwald S, Kraff O, Brote I, Ladd ME, Solbach K, Yazdanbakhsh P, Bahr A, Fautz H-P, Bitz AK. 16-channel Tx / Rx body coil for RF shimming with selected Cp modes at 7T. *Proc Intl Soc MRM* 18 2010;50.
 22. Rietsch SHG, Quick HH, Orzada S. Impact of different meander sizes on the RF transmit performance and coupling of microstrip line elements at 7 T.

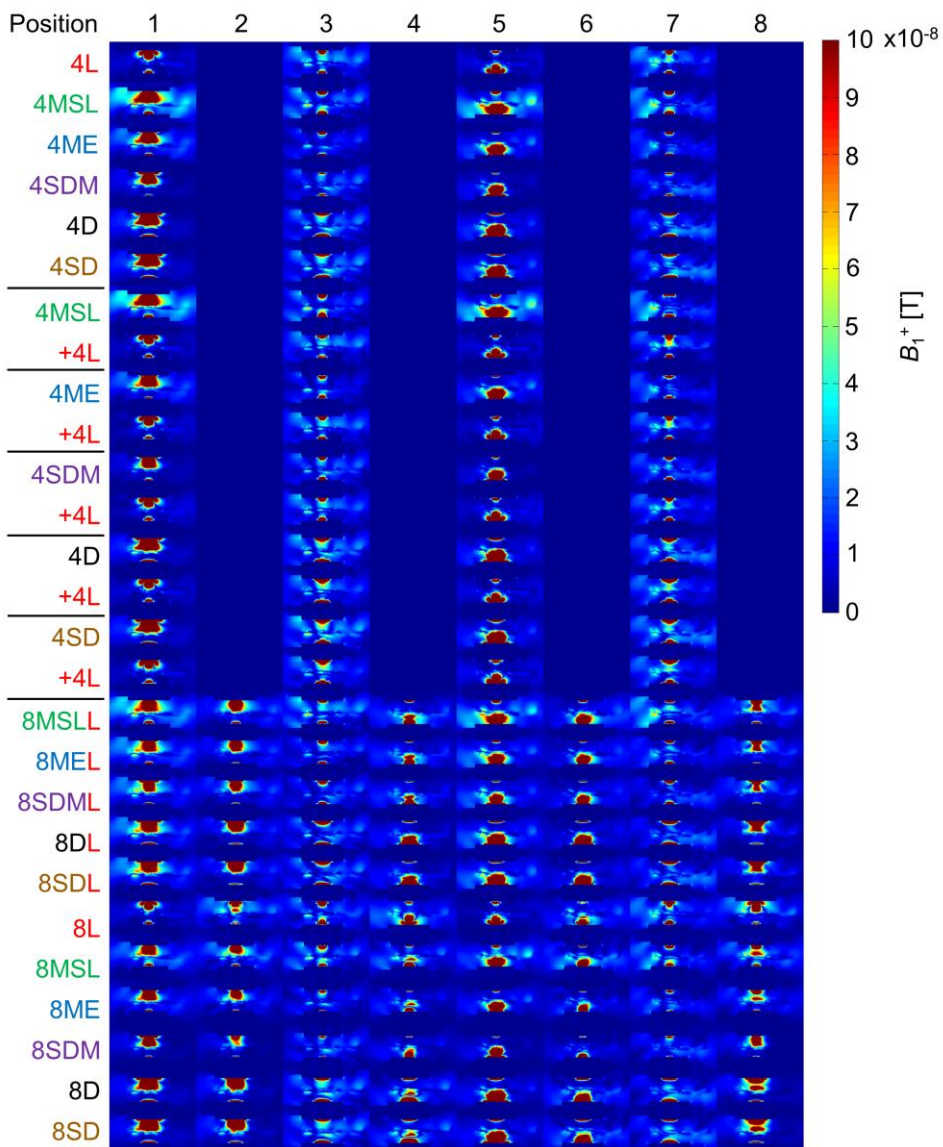
- Med Phys 2015;42(8):4542–52.
23. Brunner DO, De Zanche N, Froehlich J, Baumann D, Pruessmann KP. A symmetrically fed microstrip coil array for 7T. Proc Intl Soc MRM 15 2007;p.448.
 24. Raaijmakers AJE, Ipek O, Klomp DWJ, Possanzini C, Harvey PR, Lagendijk JJW, van den Berg CAT. Design of a radiative surface coil array element at 7 T: the single-side adapted dipole antenna. Magn Reson Med 2011;66(5):1488–97.
 25. Ertürk MA, Raaijmakers AJE, Adriany G, Uğurbil K, Metzger GJ. A 16-channel combined loop-dipole transceiver array for 7 Tesla body MRI. Magn Reson Med 2017;77:884–94.
 26. Christ A, Kainz W, Hahn EG, Honegger K, Zefferer M, Neufeld E, Rascher W, Janka R, Bautz W, Chen J, et al. The Virtual Family--development of surface-based anatomical models of two adults and two children for dosimetric simulations. Phys Med Biol 2010;55(2):N23–38.
 27. Kuehne A, Goluch S, Waxmann P, Seifert F, Ittermann B, Moser E, Laistler E. Power balance and loss mechanism analysis in RF transmit coil arrays. Magn Reson Med 2015;74(4):1165–76.
 28. Eichfelder G, Gebhardt M. Local specific absorption rate control for parallel transmission by virtual observation points. Magn Reson Med 2011;66(5):1468–76.



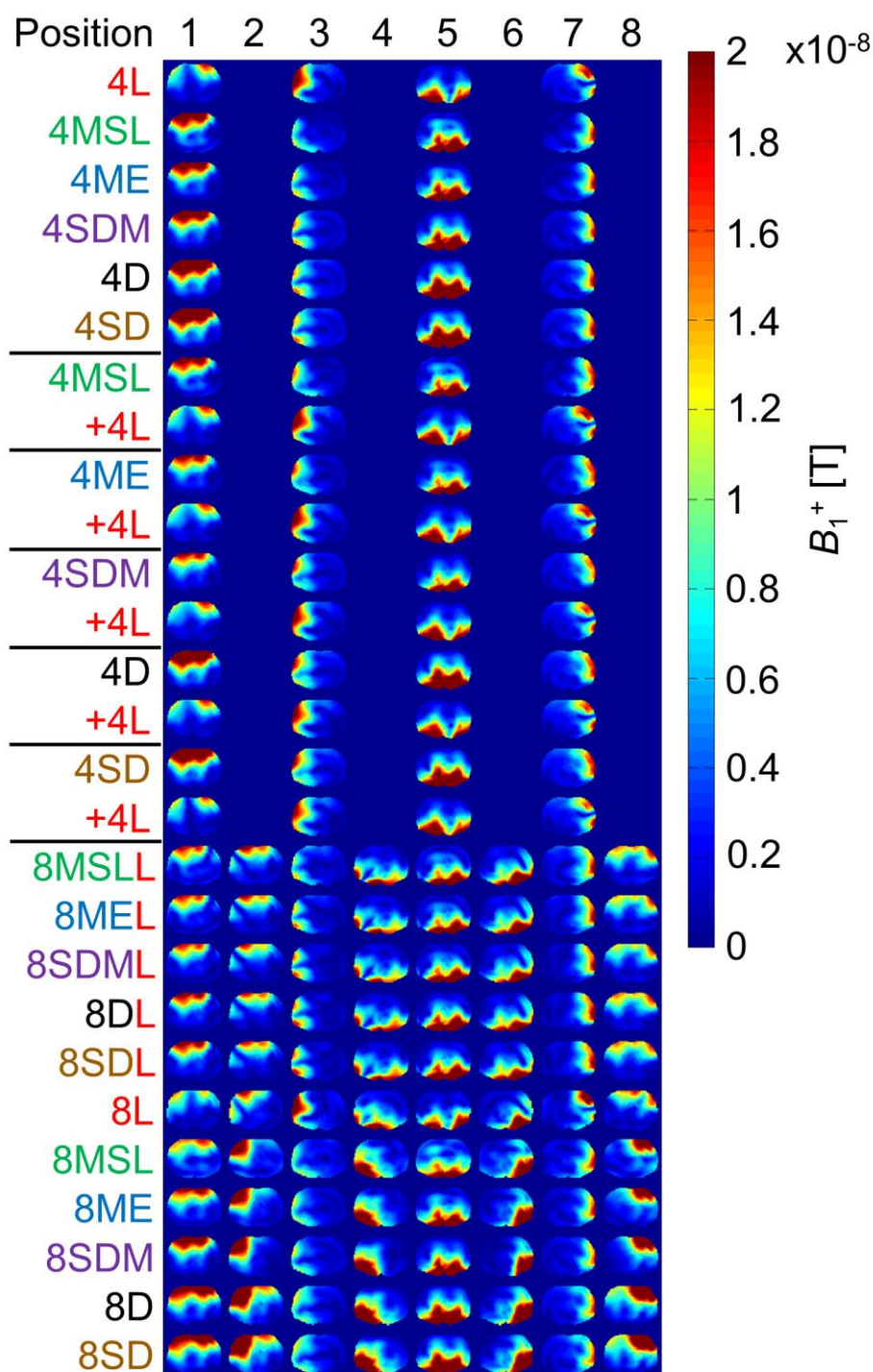
Supporting Figure 3S1: Absolute values of the B_1^+ for each channel of the investigated arrays shown for the transversal orientation. The entire simulation domain is depicted and the position indicated on top corresponds to the position at which the elements are located (Figure 3.3). While arrays with four elements show comparably small coupling to neighboring elements, coupling can be observed for arrays with eight elements on a ring, especially if loops are used for the array. Scales in all figures are cropped.



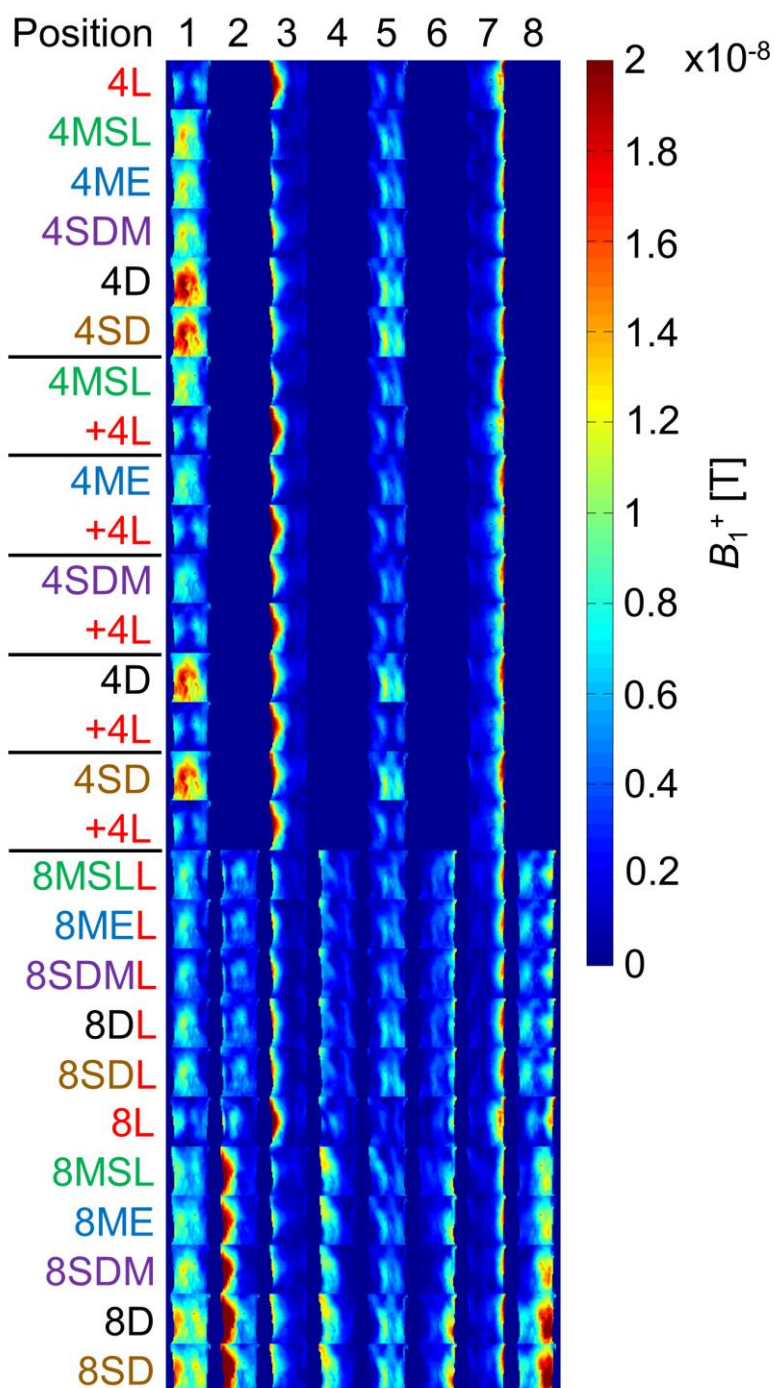
Supporting Figure 3S2: Absolute values of the B_1^+ for each channel of the investigated arrays shown for the coronal orientation. The entire simulation domain is depicted and the position indicated on top corresponds to the position at which the elements are located (Figure 3.3). In this orientation the comparably high field values for both the 4MSL and the 4MSLL array near the end of the bore can be observed. Scales in all figures are cropped.



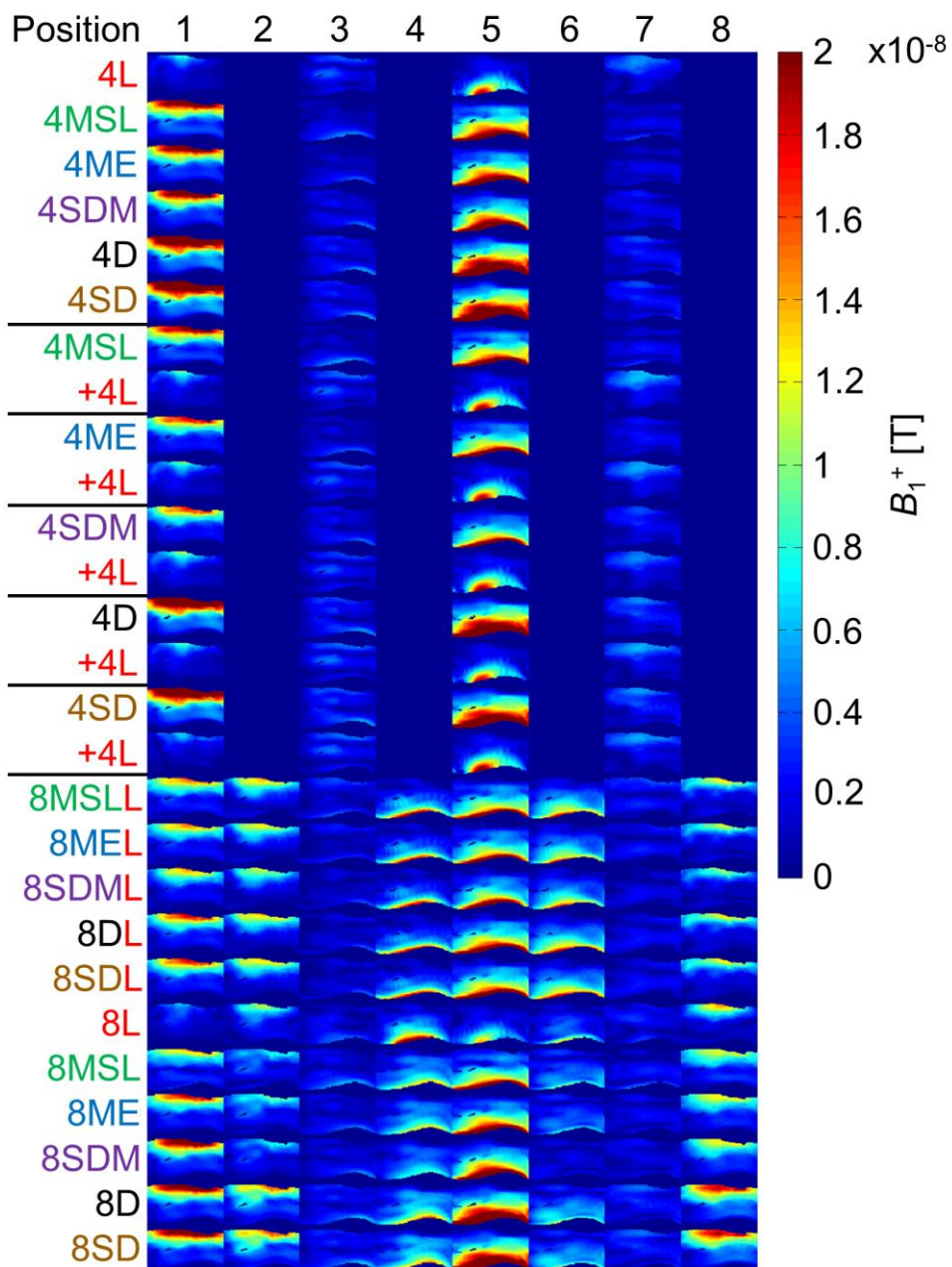
Supporting Figure 3S3: Absolute values of the B_1^+ for each channel of the investigated arrays shown for the sagittal orientation. The entire simulation domain is depicted and the position indicated on top corresponds to the position at which the elements are located (Figure 3.3). Scales in all figures are cropped.



Supporting Figure 3S4: Absolute values of the B_1^+ for each channel of the investigated arrays shown for the transversal orientation. Here, only the body model excluding the arms is depicted and the position indicated on top corresponds to the position at which the elements are located (Figure 3.3). As can be seen, the 8D and the 8SD array show comparably high field values for example at position 1,2,4-6 and 8 while near the arms (position 3 and 7) arrays with loops have high field values at least close to the surface. Scales in all figures are cropped.



Supporting Figure 3S5: Absolute values of the B_1^+ for each channel of the investigated arrays shown for the coronal orientation. Here, only the body model excluding the arms is depicted and the position indicated on top corresponds to the position at which the elements are located (Figure 3.3). Here, observations from Figure S4 are bolstered. Furthermore, the comparably high field values throughout the slice can be observed for arrays with dipoles. Scales in all figures are cropped.



Supporting Figure 3S6: Absolute values of the B_1^+ for each channel of the investigated arrays shown for the sagittal orientation. Here, only the body model excluding the arms is depicted and the position indicated on top corresponds to the position at which the elements are located (Figure 3.3). In this orientation it becomes obvious that in general elements located at positions 3 and 7 contribute only little to the field amplitude in the center. Scales in all figures are cropped.

Chapter 4 An 8-channel transceiver 7-channel receive RF coil setup for high SNR ultrahigh-field MRI of the shoulder at 7T*

Purpose

In this work, we present an 8-channel transceiver (Tx/Rx) 7-channel receive (Rx) radiofrequency (RF) coil setup for 7T ultrahigh-field MR imaging of the shoulder.

Methods

A C-shaped 8-channel Tx/Rx coil was combined with an anatomically close-fitting 7-channel Rx-only coil. The safety and performance parameters of this coil setup were evaluated on the bench and in phantom experiments. The 7T MR imaging performance of the shoulder RF coil setup was evaluated in in vivo measurements using a 3D DESS, a 2D PD-weighted TSE sequence, and safety supervision based on virtual observation points.

Results

Distinct SNR gain and acceleration capabilities provided by the additional 7-channel Rx-only coil were demonstrated in phantom and in vivo measurements. The power efficiency indicated good performance of each channel and a maximum B1+ of 19 μ T if the hardware RF power limits of the MR system were exploited. MR imaging of the shoulder was demonstrated with clinically excellent image quality and sub-millimeter spatial resolution.

Conclusion

The presented 8-channel transceiver 7-channel receive RF coil setup was successfully applied for in vivo 7T MRI of the shoulder providing a clear SNR gain versus the transceiver array without the additional receive array. Homogeneous images across the shoulder region were obtained using 8-channel subject-specific phase-only RF shimming.

*published as: Rietsch SHG, Pfaffenrot V, Bitz AK, Orzada S, Lazik-palm A, Theysohn JM, Ladd ME, Quick HH, Kraff O. An 8-channel transceiver 7-channel receive RF coil setup for high SNR ultrahigh-field MRI of the shoulder at 7T. Medical Physics 2017, 44(12):6195-6208

4.1 Introduction

While MR imaging at 1.5 and 3T magnetic field strength is widely established for a variety of diagnostic applications in the clinical setting, the use of 7T ultrahigh-field MRI is still limited to a comparably small number of about 60 research institutions (1). This can be ascribed to the main challenge encountered at UHF MRI, which is the decreasing wavelength of radiofrequency (RF) fields in tissue when employing increasing magnetic field strength (2,3). A short RF excitation wavelength may lead to inhomogeneous distribution of the RF transmit field B_1^+ (4) and renders the handling of the specific absorption rate (SAR) more challenging when compared to MRI at lower magnetic field strength (2).

Despite the inherent challenges, UHF MRI also potentially increases the imaging capabilities, especially regarding signal-to-noise ratio (SNR) (2,5–7), which can be used to increase the spatial resolution, temporal resolution, or to enable a useful tradeoff between both. Furthermore, excellent soft tissue contrast and even new contrast mechanisms (8) can provide unique insight into the human anatomy.

To exploit the potential of UHF MRI, the aforementioned challenges need to be addressed. Regarding B_1^+ inhomogeneity, approaches such as RF shimming (9,10), TIAMO (11,12), or transmit SENSE (13,14) have been presented. All of these techniques require a multi-channel RF transmit coil setup. Consequently, in UHF MRI the construction of dedicated RF coils is one of the main issues to image specific body regions. In conjunction with multi-channel RF shimming systems like the one presented in reference (15), the requirements to address the high-frequency challenges of UHF MRI are provided.

For 7T transmit (Tx) and combined transmit/receive (Tx/Rx) coils, a variety of different generic RF coil elements has been published. These include, for example, loops (16–19), microstrip lines (20,21), microstrip lines with meanders (22–24), ceramic resonators (25), bow ties (26), loopoles (27), dipoles (28,29), and other dipole-like RF elements (30–32). All of these RF coil elements have specific

advantages and disadvantages. This presents a difficult decision when choosing a specific element type. Loops, for example, do not need a shield, can be well decoupled by geometrical overlap (33), and show comparably high transmit field inhomogeneity (30) and low SAR efficiency (30) when compared to dipoles. Alternatively, a recent simulation study showed that medium-sized meander structures also yield minimal coupling and feature high transmit field strength, while dipole-like elements are advantageous with regard to their SAR efficiency (32). Regarding receive-only elements, loops are the most commonly used RF elements to boost SNR and acceleration capabilities (33), even at 7T UHF MRI (19,31,34).

Musculoskeletal UHF MR imaging has already demonstrated clinical potential and benefits beyond pure structural imaging, providing high spatial resolution in studies investigating sodium imaging, facilitating new techniques such as chemical exchange saturation transfer (CEST), or by delineating compositional differences in cartilage and trabecular bone in T2/T2* imaging (35). Compared to 3T, it has been shown in multiple joints, including the knee (36–42), wrist (43), elbow (44), ankle (36,45), and the hip (46–48), that the spatial resolution at 7T can be increased or that, alternatively, acquisition time can be reduced without compromising superior quantitative and comparable qualitative results. Today, MRI of the shoulder is almost exclusively limited to 1.5 and 3T while at 7T shoulder imaging has only been reported in two publications. In 2010, Kraff et al. presented preliminary results obtained with a multi-purpose coil for MSK imaging(44). In another study(34), Brown et al. presented an RF coil setup which is based on loops both for an 8-channel transmit-only and a 10-channel receive-only RF coil surrounding the shoulder. A total of 6 healthy volunteers were imaged to test the coil array's performance with currently no clinical follow-up study in patients. While neighboring loops in both arrays of this RF array can be decoupled by geometric overlap (33), they are not necessarily the best-suited transmit element especially at UHF (49). Also, the transmit loops were not used for signal reception in addition to the 10 Rx loops, while this could have provided a potential benefit in SNR.

Improvement of musculoskeletal imaging compared to 3T has already been demonstrated for 7T MRI of the knee (50). High spatial resolution MRI, however, necessitates not only high SNR alone, but additionally excellent g-factor performance to enable fast acquisition times through parallel imaging techniques. Consequently, a focus of RF coil array construction in general, and especially with regard to 7T shoulder imaging in the context of this work, is on high SNR. Further design aspects are coil geometry with respect to patient anatomy, B_1^+ efficiency, and RF shimming capabilities, such that the power delivered to the RF coil translates into a high flip angle within the region of interest.

To further exploit the potential of 7T shoulder MRI, the number and distribution of receive channels as well as the B_1^+ efficiency will be improved compared to previously presented coil designs by combining an 8-channel Tx/Rx coil and a 7-channel Rx coil to a combined 8-channel Tx/15-channel Rx array. The presented coil was evaluated on the bench, in volunteers, and in a patient.

4.2 Materials and Methods

The local ethics committee approved all in vivo 7 Tesla MRI measurements in this study and the subjects gave written informed consent. Four healthy male volunteers were included to assess the coil performance by imaging both shoulders of each subject (V1: 32 years old, 183 cm, 83 kg, BMI 24.8, V2: 34 years old, 188 cm, 79 kg, BMI 22.4, and V3: 34 years old, 176 cm, 82 kg, BMI 26.5, V4: 28 years old, 178 cm, 75 kg, BMI 23.7). Additionally, a female patient (51 years old, 165 cm, 66 kg, BMI 24.2) with impingement syndrome of the right shoulder was included as a pilot for a future clinical follow-up study.

8-channel Tx/Rx RF coil

In the presented setup, an 8-channel Tx/Rx RF coil is used for spin excitation. The coil is based on microstrip lines with meanders (22) with a total length of 25 cm in z-direction (Figure 4.1A) and 8 cm transverse to the meander structures. Tuning and matching are enabled by a network centrally located on the groundplane (shield) (20) that allows balanced feeding. Altogether, 8 elements are mounted on a C-shaped Plexiglas holder (Figure 4.1A) to surround the (left or right) shoulder of the subject. This C-shaped holder is separable into two parts (3 elements anterior, 5 elements posterior) for easy patient positioning (Figure 4.1B,C).

The thickness of the coil in x-direction is 47 mm (Figure 4.1B). This dictates the maximum size of a subject, which is about 520 mm in x-direction for imaging in a typical 60-cm-diameter 7T bore. According to the German industry norm DIN 33402-2, the 95th percentile for the dimension from the left to the right shoulder is 430 mm, and only 5% of adults are larger. Consequently, the available space should be sufficient for most subjects. The overall outer dimensions of the coil are 358 mm in x-direction, 378 mm in y-direction, and 300 mm in z-direction, while the space available in y-direction (anterior-posterior) inside the coil is 274 mm.

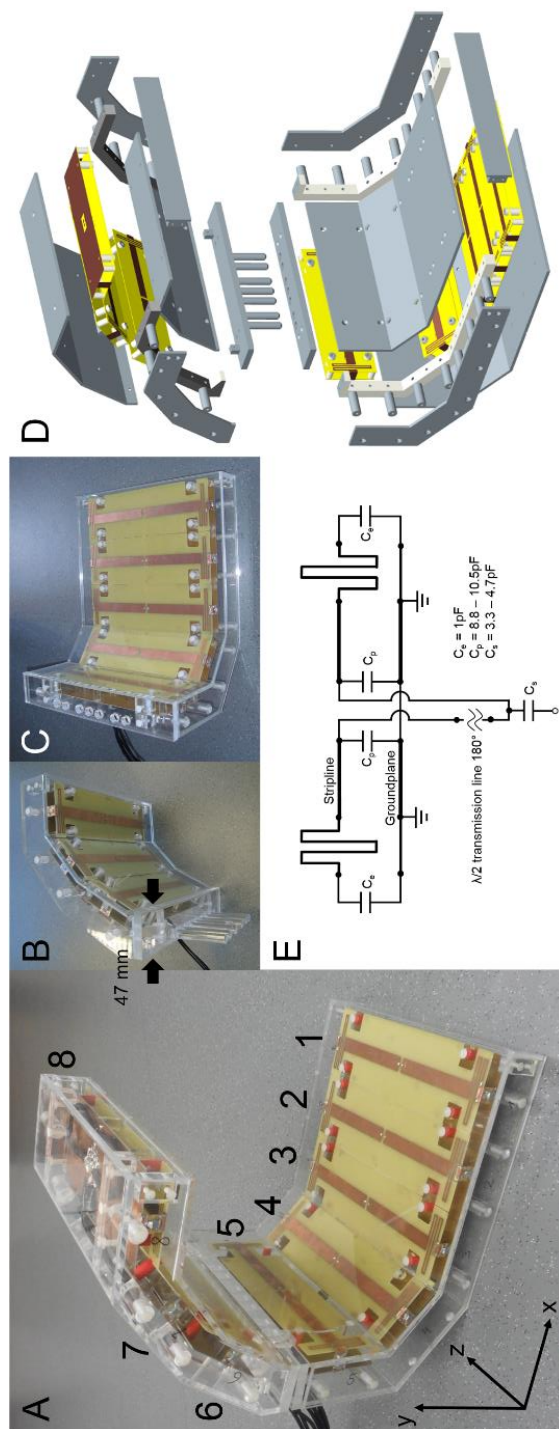


Figure 4.1: Housing of the 8Tx/Rx coil (A) with coordinate system, anterior part with 3 elements (B), posterior part with 5 elements (C), and exploded view (D). Due to the thickness of 47 mm in x-direction, the coil limits the maximum size of the subject in this direction to about 520 mm in a 600-mm-bore. The schematic of a Tx/Rx meander element (E) depicts the matching network mounted on the ground plane of the element with a serial (C_s) capacitor, two parallel capacitors (C_p), and a lambda-over-two transmission line.

The exploded schematic (Figure 4.1D) shows the construction of the Plexiglas frame on which the eight RF elements are mounted.

Values for the capacitors at the end of the RF elements (C_e), the serial capacitors (C_s) and the parallel capacitors (C_p), and the electronic layout are provided in the schematic (Figure 4.1E). A lambda-over-two transmission line (cable: RG223/U, Nexans, Paris, France) provides balanced feeding, while the connection to a custom-built 8-channel Tx/Rx switchbox with low-impedance preamplifiers (Stark Contrast, Erlangen, Germany) is accomplished via BNC connectors (cable: Aircell 5, SSB-Electronic GmbH, Lippstadt, Germany). The meander structures, the microstrip line, and the groundplane are etched on a 1 mm FR4 substrate. All capacitors (11 and 25 series, Voltronics Corporation, Denville, NJ, USA, and 11 series Dalian Dalicap Co.,Ltd., China) used for the 8-channel Tx/Rx coil are non-magnetic and optimized for low loss.

7-channel Rx RF coil

For increased SNR and acceleration performance, an additional 7-channel Rx-only coil was constructed that can be flexibly positioned on the subject and is anatomically close-fitting. A concave polymethylmethacrylate housing (Figure 4.2A) with 3 mm thickness was used. This housing contains 6 overlapping loops arranged in a hexagonal shape (Figure 4.2B) with a seventh loop placed in the center. These unshielded loops are made of insulated copper wire soldered on 1-mm FR4 printed boards (Protomat H60 milling machine, LPKF Laser & Electronics AG, Garbsen, Germany) with added capacitors. Cable traps (BalUn) are placed 1 cm from the RF feeding point of the loops and at the end of the housing.

Detuning of each RF channel (Figure 4.2C) is enabled by a PIN diode (MA4P7470F-1072T, MACOM, MA, USA) mounted on an FR4 printed circuit board. The PIN diode introduces a short connection to ground that is transformed to a high impedance at the coil terminals.

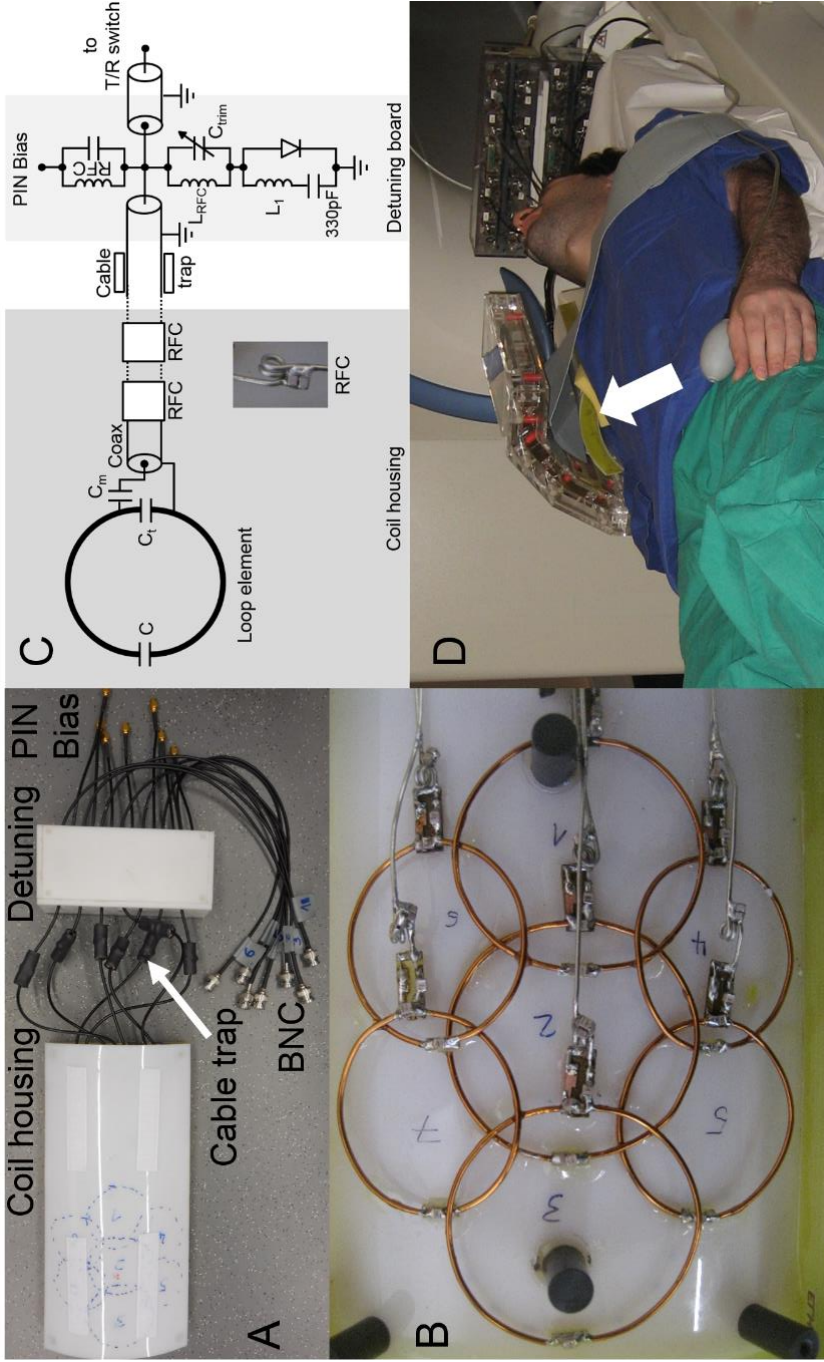


Figure 4.1: Housing of the 7-channel Rx-only coil connected to the housing of the detuning board (A). Each of the 7 loop elements (B) can be described with the same schematic (C), showing 2 radiofrequency chokes (RFC) and the cable trap as well as the detuning mechanism, which is based on a short provided by the PIN diode. This short can be optimized by adjusting the trimming capacitor C_{trim} , while the parasitic capacitance of the PIN diode during reception is compensated by the inductance L_1 . The full coil setup (D) on a volunteer allows imaging of both shoulders. The position of the ergonomically-designed 7-channel Rx-only coil is indicated by the white arrow (D).

The circuit board is isolated by a polymethylmethacrylate housing to prevent patient contact (Figure 4.2A). Inside the 7-channel Rx coil (Figure 4.2B,C), semi-rigid coaxial cables are used to form radiofrequency chokes (RFC) by winding the cable and soldering a capacitance across the windings (Figure 4.2C). One RFC is located 1 cm from each coil element's feeding point (Figure 4.2B) and another one is located on an FR4 circuit board at the end of the coil housing. From there, coaxial cables (G02232D, Huber & Suhner GmbH, Taufkirchen, Germany) are used to connect the 7-channel Rx coil and the detuning board as well as the detuning board and the custom-built 8-channel Tx/Rx switchbox (identically to the one used with the 8-channel transceiver coil) via BNC connectors. The rationale behind using an existing switchbox was to save costs for additional preamplifiers. The PIN bias necessary for detuning is provided via a TIM™ cable (Total Imaging Matrix, Siemens Healthineers GmbH, Erlangen, Germany) and SMA connectors (Figure 4.2A). One floating cable trap (51) is placed on each cable between the coil housing and the housing of the detuning board (Figure 4.2A).

The entire RF coil setup with both arrays (Figure 4.2D) allows MR imaging of either the right or the left shoulder.

Safety evaluation

In order to guarantee safe use of the 8-channel Tx/Rx coil in transmit mode according to the IEC international standard 60601-2-33, the 10-g specific absorption rate (SAR_{10g}) was monitored with a custom-built real-time SAR supervision system using virtual observation points (VOP) (52). For this purpose, finite integration technique simulations (Microwave Studio, CST, Darmstadt, Germany) of the 8-channel Tx/Rx coil loaded with the body models DUKE and ELLA from the virtual family (53) were performed.

Prior to the SAR simulations the coil model used in the simulations was validated by performing dosimetric measurements of the H-field at 297 MHz inside an

elliptical phantom filled with tissue-simulating liquid ($\epsilon_r = 45.3$, $\sigma = 0.84 \Omega^{-1} \text{ m}^{-1}$). The phantom offers adequate coil loading and a canonical test scenario for the validation. A field probe (Dosimetric Assessment System, SPEAG, Zurich, Switzerland) was systematically moved through the phantom by a computer-controlled three-axis positioning device while the 8-channel Tx/Rx coil was driven in the circularly polarized mode (45° phase increments) using an 8-channel custom-built Butler matrix. The results of the field probe measurements were compared to the numerical simulation of the identical setup to validate the RF coil model and to determine a reasonable safety margin with respect to the deviation under consideration of the measurement error. The measurement error that is employed represents the expanded uncertainty (coverage factor of 2) of all error sources.

The field probe measurement setup was also used to demonstrate adequate detuning of the 7-channel Rx-only coil array in the combined setup by comparing line plot measurements of the 8-channel Tx/Rx RF coil with and without the 7-channel Rx-only coil in place. If the deviation between these two measurements was sufficiently low (on the order of the measurement error), the detuning performance of the 7-channel Rx-only coil was considered to be validated.

Coil performance on the bench

Preamplifier decoupling and detuning efficiency of the RF coils were measured on the bench with a 2-channel network analyzer (Agilent E5061A, Agilent Technologies, Santa Clara, CA, USA) and a custom-built RF sniffer probe consisting of two loosely coupled loops.

Coil performance on 7T MR system

All MRI measurements were acquired on a 7T whole-body research system (MAGNETOM 7T, Siemens Healthineers GmbH, Erlangen, Germany) equipped with

a custom-built 8-channel RF transmit chain add-on (15) that allows for static (amplitude and phase) RF shimming. The system's gradient coil (AS095, Siemens Healthineers GmbH, Erlangen, Germany, maximum gradient amplitude 38 mT/m, maximum slew rate $200 \text{ T} \cdot \text{m}^{-1} \cdot \text{s}^{-1}$) allows for sufficient linear field-of-view coverage to image both shoulders. Measurements included the acquisition of the noise correlation between the RF coil channels, g-factor maps, and SNR maps both in a phantom (cylindrical body-sized phantom filled with tissue-simulating liquid, $\epsilon_r = 46.3$, $\sigma = 0.8 \text{ } \Omega^{-1} \text{ m}^{-1}$) and in four healthy male volunteers (both shoulders were imaged in each subject). To ensure that the measurement setup is as close as possible to the body model used in the simulations, each volunteer was positioned accordingly with respect to the position of the 8-channel Tx/Rx coil. The 7-channel Rx-only coil was positioned in the center of the 8-channel Tx/Rx coil (z-direction).

The SNR gain provided by additionally using the 7-channel Rx-only coil was calculated by dividing SNR maps acquired with the combination of both arrays by SNR maps acquired with only the 8-channel Tx/Rx coil. For the measurements with the 8-channel Tx/Rx coil alone, the patient table was moved out of the magnet after measuring with the combination of both arrays. While the subject remained within the RF coil, the 7-channel Rx-only coil was carefully disconnected and removed to allow subsequent imaging of the subject's shoulder at identical spatial position. Two 3D MRI datasets obtained prior to and after the hardware modifications were loaded into the fusion toolbox on the MR console (Syngo, VB17, Siemens Healthineers GmbH, Erlangen, Germany) to qualitatively verify no or only marginal movement of the subjects relative to the 8-channel Tx/Rx RF shoulder coil. Evaluations were performed for transversal, para-coronal, and para-sagittal orientation for the phantom and the four volunteers.

In order to obtain channel-dependent B_1^+ maps of the 8-channel Tx/Rx coil, the B1TIAMO mapping approach presented by Brunheim et al. (54) was utilized in transversal orientation. This approach is based on relative single-channel maps, each scaled by absolute flip angle distributions of two complementary shim settings

to obtain reasonable absolute single-channel maps in the whole region of interest. First, phase shims with 45° phase increment (CP+ mode) and with 90° phase increment (CP2+ mode) were used as complementary shims to cover the region of interest in transversal orientation. Then, the aforementioned method was applied to obtain B_1^+ maps for each channel. Since, CP+ and CP2+ are not necessarily the best choice for an asymmetric RF array, two new optimized shims were calculated from the resulting single-channel B_1^+ maps. The final absolute $|B_1^+|$ maps resulted by applying B1TIAMO again with these shims. This procedure was applied for both the phantom and the four volunteers for both the left and the right side. For the phantom, a rectangular RF pulse with 1 ms duration and 220 V nominal pulse amplitude was used. For the volunteers, an optimized 4 ms duration double sinc RF pulse (each 450 Hz bandwidth) with 344 V nominal pulse amplitude was used to simultaneously cover fat and water (1 kHz distance of the peaks), which improved the SNR in the maps.

In vivo imaging

For all anatomical images phase-only RF shimming was applied to obtain a high amplitude in the region of interest which is needed in particular for the acquisition of clinically relevant spin echo images under the current constraints of limited available peak RF power at 7 T. Shims were calculated (in about 3 minutes) based on the measured B_1^+ maps and an algorithm balancing field maximization and homogeneity. Two anatomical sequences based on clinical protocols adapted from 7T studies on hip joint imaging (48,55) were acquired in the four volunteers and in the patient. The first anatomical sequence was a 3D double-echo steady state (DESS) sequence with water excitation acquired in para-coronal orientation with a 190 x 190 mm² in-plane field of view (FOV), an isotropic resolution of 0.74 mm, repetition time (TR) / echo time (TE) of 8.1/2.4 ms, and acquisition time (TA) of 4 min 58 sec. The second anatomical sequence was a proton density (PD) weighted 2D turbo spin echo (TSE) sequence in transversal orientation with a 180 x 180 mm²

in-plane FOV, a spatial resolution of $0.35 \times 0.35 \times 2.50 \text{ mm}^3$, TR/TE of 4500/36 ms, and TA of 3 min 32 sec. Both sequences were acquired with parallel imaging acceleration factors of $R = 2/3/4$ using GRAPPA. Phase-only RF shimming was used in order to balance both amplitude and homogeneity in the shoulder of the subject.

4.3 Results

Safety evaluation

In Figure 4.3 the results of the H-field measurements for the validation of the numerical coil model in an elliptical phantom are shown. In the sagittal plane (Figure 4.3A), high qualitative agreement between simulation (Figure 4.3B) and measurement (Figure 4.3C) can be seen. However, the simulation slightly overestimates the values of the H-field. Closer to the coil, for example along the microstrip line of element 2 (Figure 4.3D), there is high quantitative agreement between simulation and measurement. Subsequently, VOP files were generated from the SAR simulations performed with two different body models.

To further evaluate the detuning performance of the 7-channel Rx-only coil, which was measured at the bench, measurements along z-direction (Figure 4.3E) with and without this coil were performed at three different locations (Figure 4.3F-H). These three positions correspond to the three rows of loops within the hexagonal shape of the 7-channel Rx-only coil. The quantitative agreement between measurements with and without the 7-channel Rx-only coil is sufficiently high considering the measurement error. Consequently, the detuning of the 7-channel Rx-only array is validated.

Coil performance on the bench

Measurements on the bench yielded mean values of -10.8 dB (worst case -8 dB) for the preamplifier decoupling; for the 7-channel Rx-only coil, the mean detuning was -18.7 dB (worst case -15.3 dB).

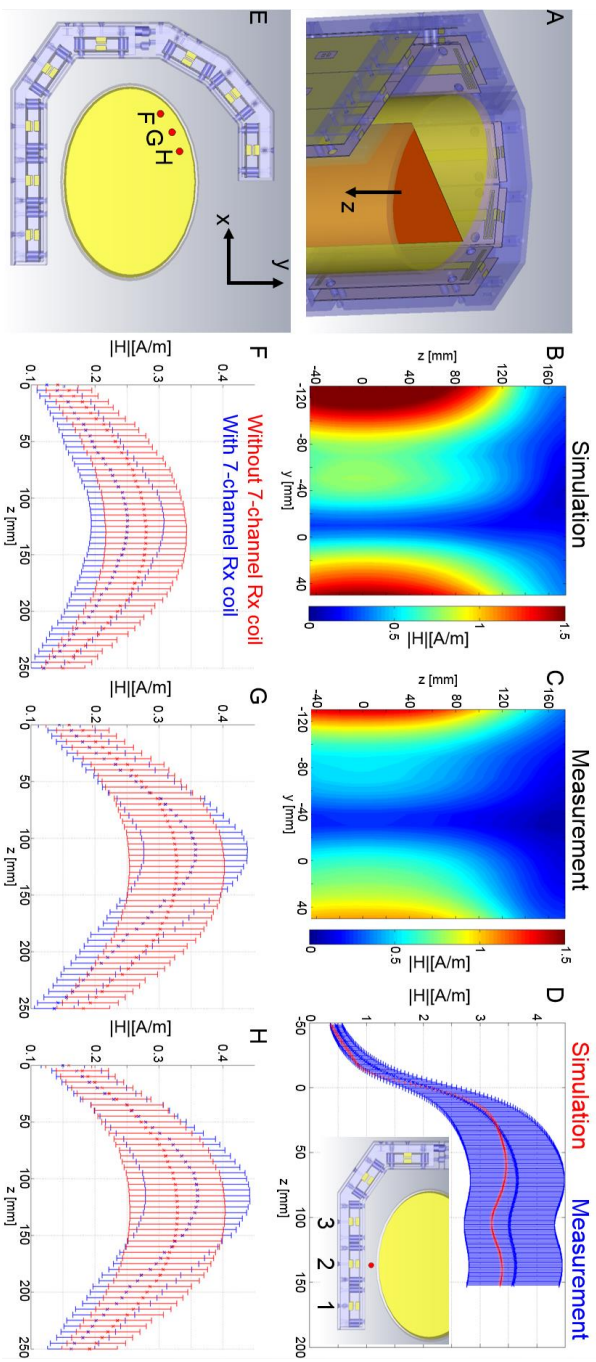


Figure 4.3: Results of the validation part of the safety assessment performed prior to the full SAR simulations in different body models. (A) shows the elliptical phantom and the evaluated sagittal plane (red). Qualitatively the simulation (B) and measurement (C) match well, although the simulation slightly overestimates the H-field in the tissue-simulating liquid. Close to the element of channel 2 (D) the evaluation along z-direction shows very good agreement between simulation and measurement in air. Measurements along z-direction (E) at three positions (F-H) with and without the 7-channel Rx-only coil demonstrate the detuning efficiency.

Coil performance on 7T MR system

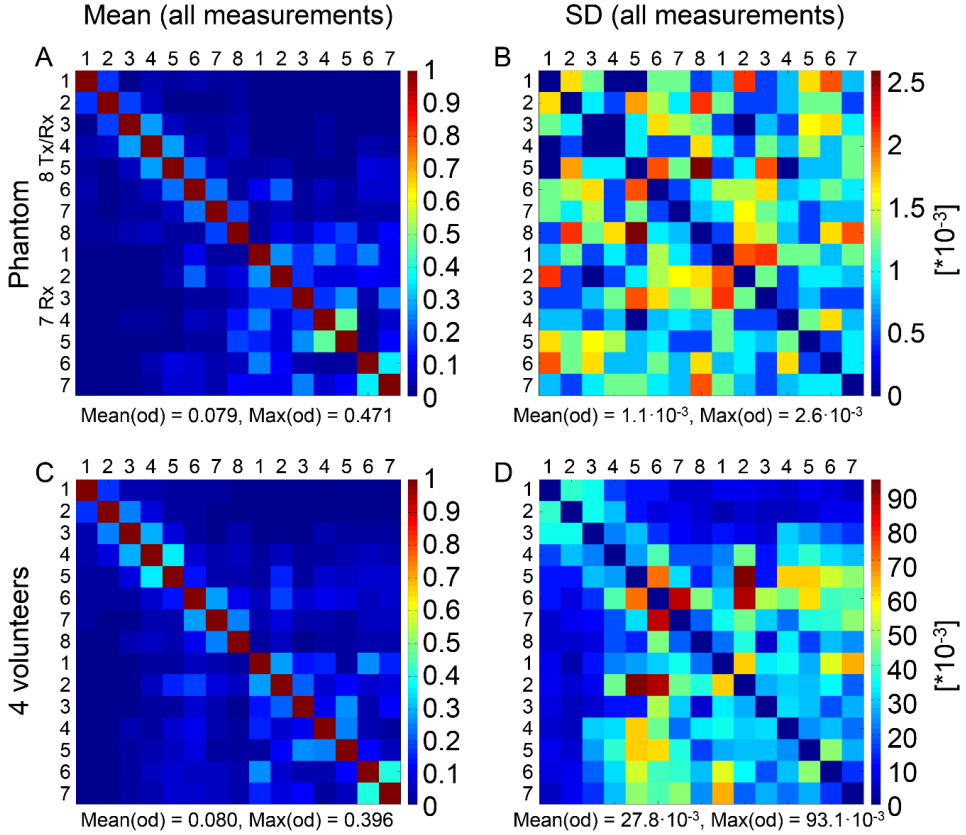


Figure 4.4: Evaluation of the noise correlation coefficient for the phantom and the 4 volunteers. For the phantom, the magnitude of the noise correlation coefficient is averaged over acquisitions of transversal, para-coronal, and para-sagittal orientations (A). The standard deviation (SD) for the off-diagonal (od) elements of these 3 orientations (B) is low, which could be expected. For the 4 volunteers the averaging (C) was performed over all volunteers, over acquisitions of the left and right shoulder, and over each of the three slice orientations to investigate the influence of the coil loading. Here, the SD is higher compared to the phantom measurements.

The results for the evaluation of the noise correlation coefficients are presented in Figure 4.4. In order to quantify the load dependence of the RF arrays for the

phantom, the mean value of the measurements in transversal, para-coronal, and para-sagittal orientation was calculated (Figure 4.4A). The corresponding standard deviation (SD) among these measurements (Figure 4.4B) is low. For the volunteer measurements, the mean of all measurements for different volunteers, left and right shoulder, and for slice orientations was calculated (Figure 4.4C). The corresponding SD (Figure 4.4D) indicates comparatively higher variation, especially between channel 2 of the 7-channel Rx-only coil and channels 6 and 5 of the 8-channel Tx/Rx coil.

The SNR gain evaluated in the body-sized phantom (Figure 4.5A-D) was calculated by dividing SNR maps acquired with the combination of 8-channel Tx/Rx coil and 7-channel Rx-only coil by SNR maps acquired with the 8-channel Tx/Rx coil alone. A combined image (Figure 4.5A) indicates the slice orientations, while the SNR gain is illustrated in transversal (B), para-coronal (C), and para-sagittal (D) orientation. As soon as the color differs from the background, the 7-channel Rx-only coil boosts the SNR and a distinct SNR gain can be observed in all orientations. As expected, the SNR gain is highest near areas close to the surface where the 7-channel Rx-only coil is located and decreases towards regions further away from the coil.

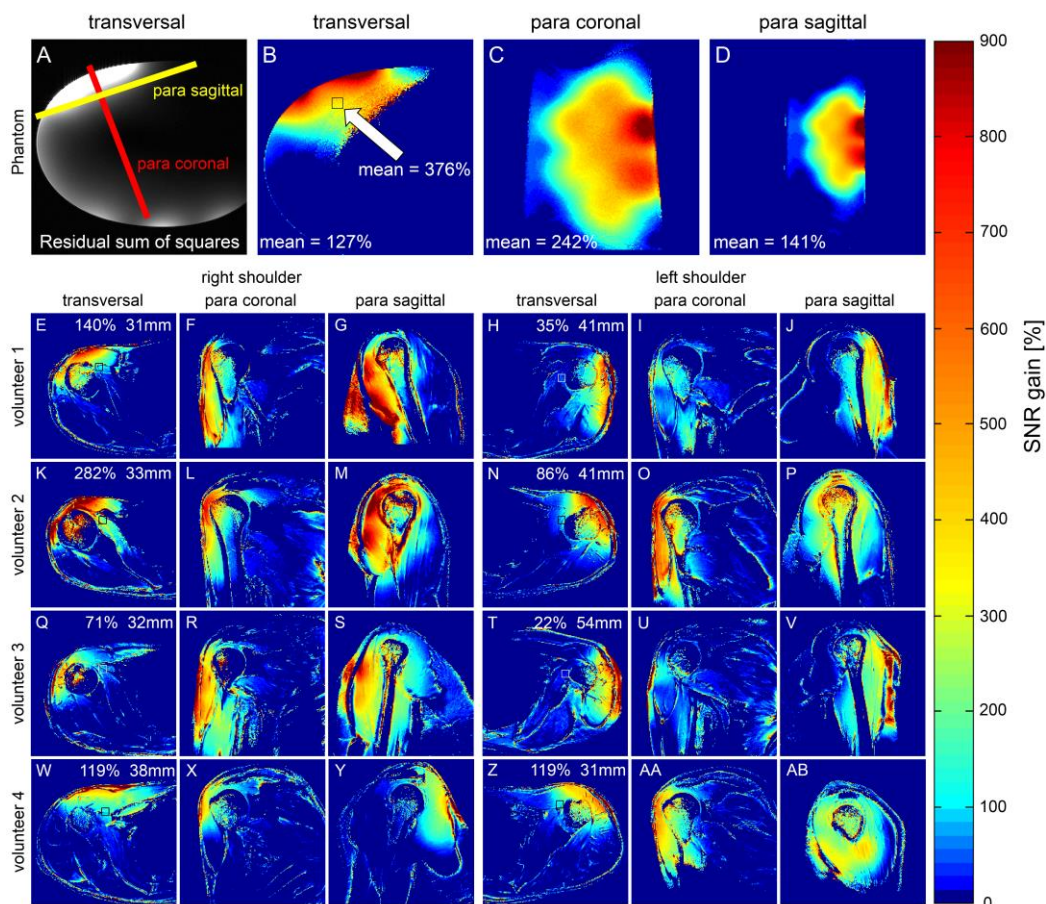


Figure 4.5: SNR gain (cropped scale) in a body-sized phantom (A-D) and in the four volunteers for the right and the left shoulder (E-AB). SNR gain in comparably deep-laying regions is visibly independent of the coil positioning, while the absolute values depend on the position of the 7-channel Rx-only coil. In transversal orientation, the average SNR gain is calculated in rectangular regions of interest at a certain distance from the surface, e.g. 376% in the rectangular region (B) which is located 42 mm from the surface of the phantom or 140% in a rectangular region 31 mm from the surface (E). The areas in which SNR gain is visible indicate the coverage of the 7-channel Rx coil.

The results from the volunteer measurements (Figure 4.5E-AB) confirm the SNR gain observed in the phantom measurements. However, the influence of both the position of the arrays, especially the 7-channel Rx-only coil, and the subject geometry is important here. While, for example, a high SNR gain of 282% can be measured in a region of interest next to the shoulder joint in transversal orientation for volunteer 2 (Figure 4.5K), the SNR gain at a comparable distance from the surface in volunteer 3 is only 71% (Figure 4.5Q), but still significant.

Results for the g-factors for SENSE acceleration are provided in Table 4.1 for the measurements in a body-sized phantom (mean/maximum g-factors) and for the four volunteers (mean \pm SD of the average g-factor among the volunteers). In all measurements, the combination of the two RF arrays has lower g-factors than the 8-channel Tx/Rx coil alone. Consequently, the improved geometry is advantageous to maintain sufficient SNR in accelerated imaging. Furthermore, the gain for the arrays is maximum for the para-sagittal orientation, followed by the para-coronal and the transversal orientations, both in the phantom and in the left and right shoulder of the four volunteers. In general, the lowest g-factors are achieved in transversal orientation for both coil setups. The performance in the left and right shoulder is comparable for volunteers in transversal orientation, while for the para-coronal and para-sagittal orientations the difference is slightly larger.

Phantom									
	8Tx/Tx				8Tx/Tx + 7Rx				
tra	AP/RL	1	2	3	AP/RL	1	2	3	4
	2	1.05/2.04	1.15/2.54	1.53/10.87	2	1.03/1.47	1.07/1.59	1.18/2.15	
	3	1.15/3.39	1.45/8.85		3	1.09/1.72	1.17/2.09	1.43/3.51	2.17/16.39
	4	1.37/5.49			4	1.23/2.47		2.03/9.01	
	HF/RL	1	2	3	HF/RL	1	2	3	4
para sag	2	1.07/2.03	5.14/30.30	13.22/111.1	2	1.04/1.41	1.14/1.90	1.25/2.76	
	3	1.13/2.26	6.93/83.33		3	1.07/1.65	1.28/4.42	1.49/4.27	2.19/16.67
	4	1.33/3.50			4	1.17/2.09		2.15/11.36	
para sag	HF/AP	1	2	3	HF/AP	1	2	3	4
	2	2.42/12.66	2.88/18.18	3.77/58.82	2	1.11/1.80	1.20/2.24	1.32/2.66	
	3	9.69/29.41	14.00/83.33		3	1.15/1.85	1.32/2.71	1.58/3.92	2.15/7.35
	4	18.74/125.00			4	1.26/3.14		2.22/9.17	

Table 4.1: Comparison of the mean/maximum g-factors in the phantom scan using only the 8-channel Tx/Rx coil or the combination of the 8-channel Tx/Rx and the 7-channel Rx-only coil. For the volunteer measurements of the left and the right shoulder, the same comparison is shown. Values represent mean \pm SD among the four volunteers for the average g-factor. The directions of acceleration are Ry (anterior/posterior), Rx (left/right) and Rz (head/feet). As can be seen, in general, the lowest g-factors can be achieved in the transversal orientation.

8Tx/Tx										8Tx/Tx + 7Rx									
		AP/RL		1		2		3		AP/RL		1		2		3		4	
tra		2		1.05 ± 0.01		1.20 ± 0.01		1.54 ± 0.03		2		1.04 ± 0.01		1.11 ± 0.01		1.23 ± 0.01			
		3		1.17 ± 0.02		1.62 ± 0.03				3		1.09 ± 0.01		1.23 ± 0.01		1.50 ± 0.01		2.20 ± 0.06	
		4		1.37 ± 0.03						4		1.20 ± 0.01				2.13 ± 0.03			
		HF/RL		1		2		3		HF/RL		1		2		3		4	
para sag		2		1.03 ± 0.01		1.58 ± 0.19		3.43 ± 0.80		2		1.01 ± 0.01		1.20 ± 0.11		1.52 ± 0.24			
		3		1.12 ± 0.02		2.12 ± 0.29				3		1.07 ± 0.01		1.36 ± 0.12		1.95 ± 0.30		2.98 ± 0.53	
		4		1.30 ± 0.02						4		1.21 ± 0.02				3.01 ± 0.50			
para sag		HF/AP		1		2		3		HF/AP		1		2		3		4	
		2		1.50 ± 0.42		1.80 ± 0.49		2.68 ± 0.49		2		1.03 ± 0.01		1.10 ± 0.02		1.22 ± 0.02			
		3		2.78 ± 1.25		4.17 ± 1.90				3		1.08 ± 0.01		1.21 ± 0.02		1.46 ± 0.02		2.05 ± 0.03	
		4		4.41 ± 2.22						4		1.18 ± 0.01				2.05 ± 0.05			

8Tx/Tx										8Tx/Tx + 7Rx									
		AP/RL		1		2		3		AP/RL		1		2		3		4	
tra	2	1.05 ± 0.01		1.22 ± 0.01		1.65 ± 0.03		2		1.03 ± 0.00		1.10 ± 0.01		1.23 ± 0.02					
	3	1.16 ± 0.01		1.62 ± 0.03				3		1.09 ± 0.01		1.23 ± 0.01		1.51 ± 0.03		2.21 ± 0.08			
	4	1.39 ± 0.03						4		1.23 ± 0.03				2.23 ± 0.10					
	RL/HF	1		2		3		RL/HF		1		2		3		4			
para sag	2	1.05 ± 0.01		1.66 ± 0.19		4.12 ± 1.19		2		1.04 ± 0.02		1.29 ± 0.25		1.87 ± 0.93					
	3	1.18 ± 0.05		2.31 ± 0.32				3		1.13 ± 0.03		1.51 ± 0.33		2.40 ± 1.19		3.76 ± 2.26			
	4	1.41 ± 0.10						4		1.27 ± 0.07				3.66 ± 1.88					
para sag	HF/AP	1		2		3		HF/AP		1		2		3		4			
	2	1.54 ± 0.28		1.80 ± 0.34		2.59 ± 0.43		2		1.11 ± 0.05		1.17 ± 0.05		1.29 ± 0.04					
	3	2.75 ± 0.47		4.00 ± 0.62				3		1.24 ± 0.13		1.38 ± 0.14		1.64 ± 0.17		2.41 ± 0.26			
	4	4.25 ± 0.67						4		1.38 ± 0.18				2.36 ± 0.30					

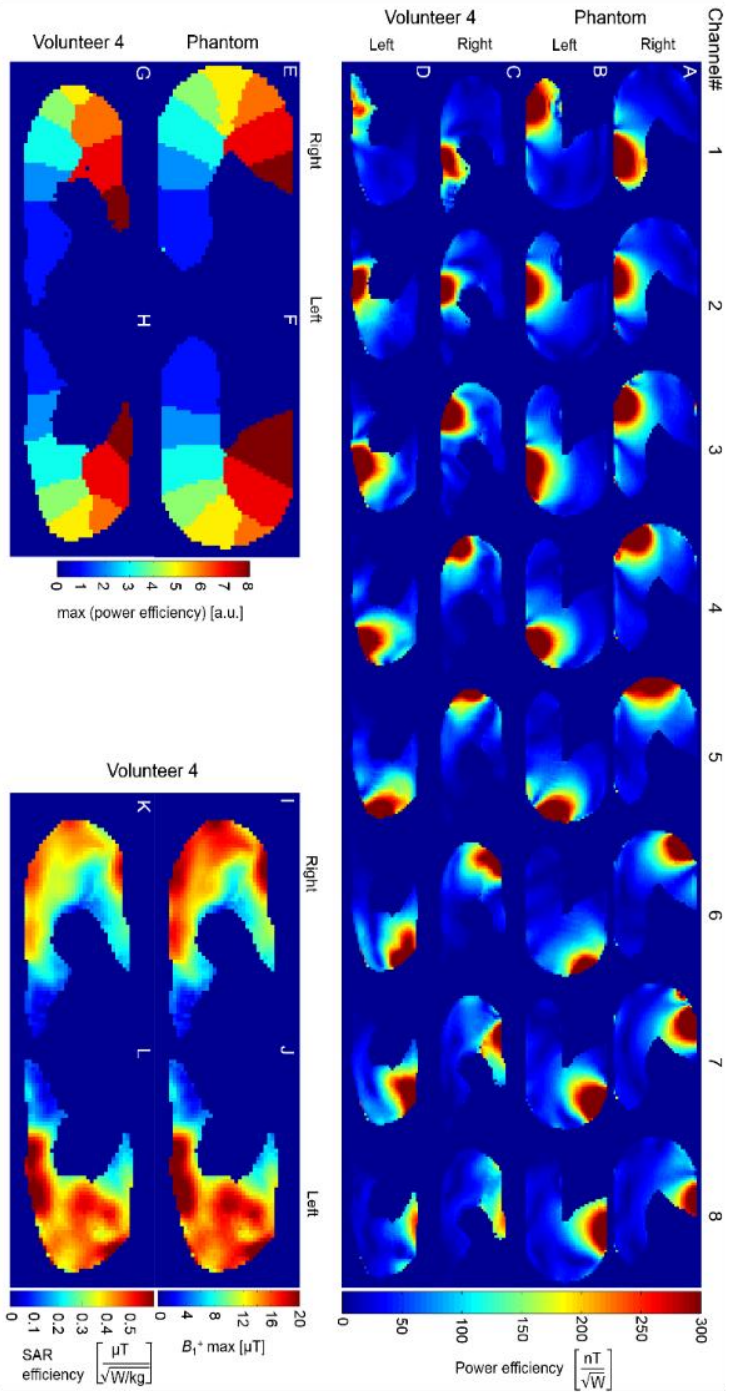


Figure 4.6: Channel-dependent power efficiency for the 8-channel Tx/Rx coil for the right (A) and the left (B) side in a phantom and for the right (C) and the left (D) shoulder of volunteer 4. As shown, the power efficiency of the channels is approximately equal and the entire region of interest is well covered. The regions in which one channel has the highest signal intensity is indicated in (E-H) for both sides of the phantom and volunteer 4, indicating that the loading conditions influence the overall contribution of each channel. For two different phase-only RF shims with maximum available hardware power in the right (I) and in the left (J) shoulder of volunteer 4, a maximum B_1^+ amplitude of 19 μT in the shoulder can be achieved. The SAR efficiency for the two shims (K,L) indicates good performance.

Well-differentiated excitation profiles can be observed in the power efficiency maps in Figure 4.6A-D. For the right (Figure 4.6A) and the left (Figure 4.6B) side of the phantom the power efficiency is approximately equal for each RF channel. The intensity profiles are slightly twisted for both orientations. The power efficiency in the phantom and in volunteer 4 is comparable, while slightly lower power efficiency was found for channels 1 and 8 in the volunteer. The distributions differ due to the different electric properties of the subjects and the heterogeneous tissue distribution of the volunteers. To evaluate which RF element contributes most to a certain region in the transversal slice, the index of the corresponding channel is depicted in Figure 4.6E and F for the phantom and in Figure 4.6G and H for volunteer 4. As can be seen, the profiles are more clearly separated in the phantom while they are deformed in the volunteer. Especially channel 5 contributes only to the surface in the volunteer's right shoulder. Figure 4.6I, J show how much B1+ amplitude can be reached for a dedicated phase-only shim if the RF hardware power limits of the system are exploited. Maximum values of about 19 μ T can be reached even in deeper-lying regions behind the shoulder joint. For these two shim settings the SAR efficiency was calculated (Figure 4.6K,L) based on the VOPs.

In vivo imaging

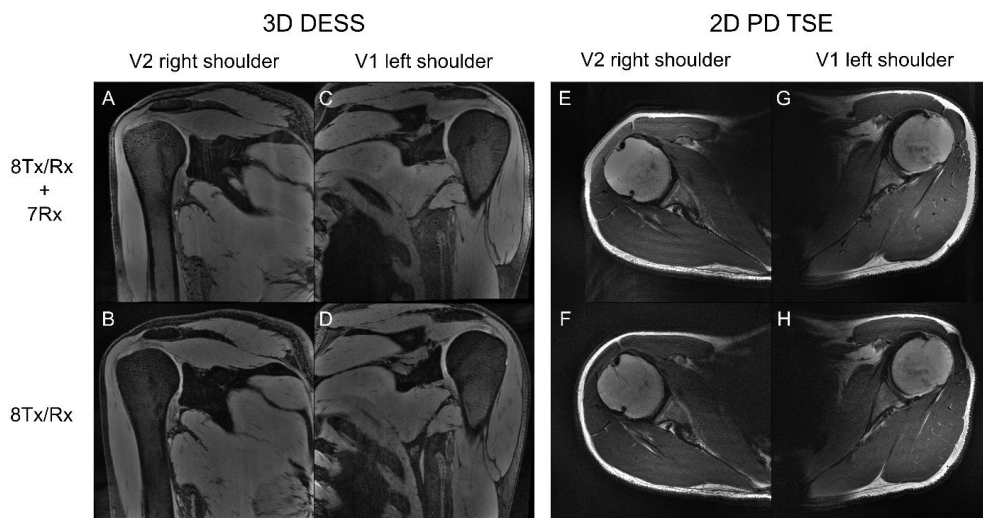


Figure 4.7: Measurements in volunteer 1 (V1) and volunteer 2 (V2) with and without the 7-channel Rx-only coil using a 3D DESS sequence with water excitation (A-D) in para-coronal and a 2D PD TSE sequence in transversal orientation (E-H), both accelerated by a factor of $R = 2$. Please note the enhanced anatomical detail and better SNR when the combination of both arrays is used, especially close to the 7-channel Rx-only coil. Intensity correction was applied to all images.

In Figure 4.7, the MR imaging results of volunteers 1 (left shoulder) and 2 (right shoulder) are depicted using both the combination of the 8-channel Tx/Rx coil and the 7-channel Rx-only coil as well as the 8-channel Tx/Rx coil alone, respectively. An image intensity correction was used for all images to yield a balanced comparison while partially masking the gain in SNR for the combined coil setup. Surface coil intensity corrections are common practice on clinical 1.5 T and 3 T systems, but not directly available on 7 T systems. For the 3D DESS sequence (Figure 4.7A-D) in para-coronal orientation, slightly higher image quality can be observed, which manifests in higher anatomical detail and less prominence of noisy regions. This is especially visible in the triceps close to the 7-channel Rx-only coil when both arrays are used (Figure 4.7A,C) compared to the case where only the 8-channel Tx/Rx coil is used (Figure 4.7B,D). Improved capabilities for the combination of both RF arrays can

also be appreciated in Figure 4.7E-H for the 2D PD-weighted TSE images. Subtle anatomical details are much better visible in Figure 4.7E compared to Figure 4.7F as well as in Figure 4.7G compared to Figure 4.7H.

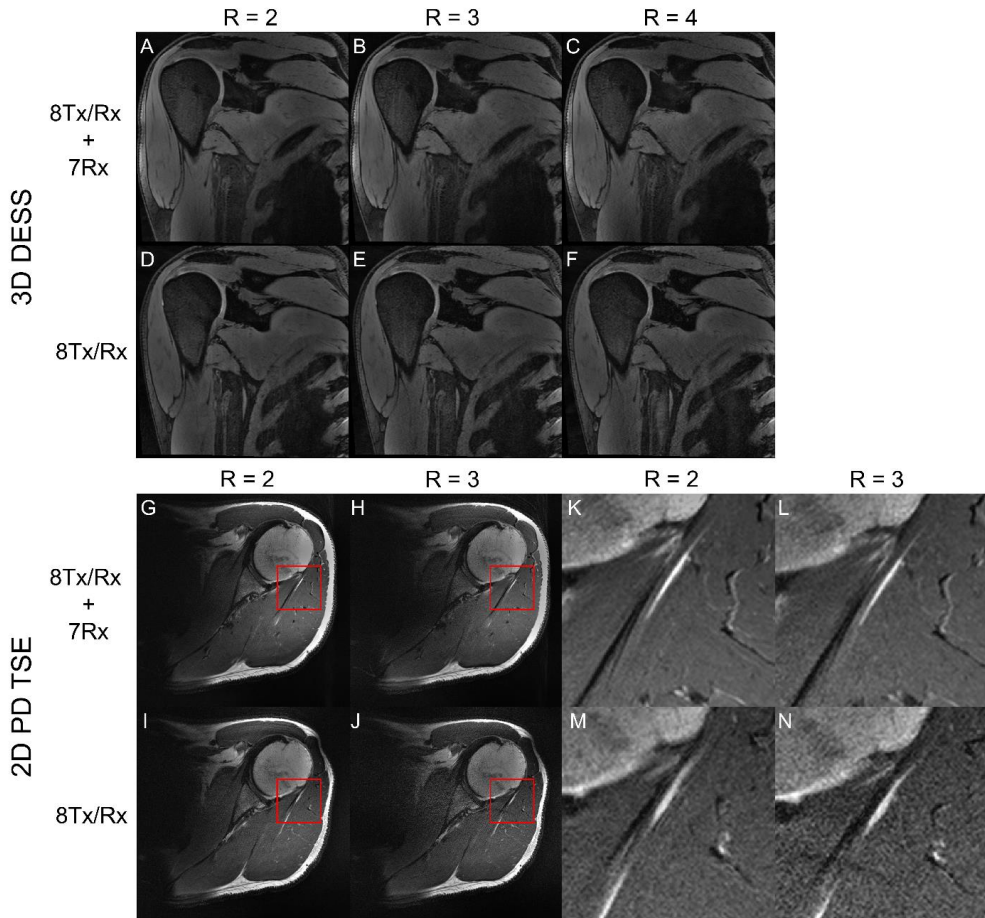


Figure 4.8: Impact of different acceleration factors on measurements of volunteer 1 for the 3D DESS (A-F) and TSE sequence (G-N) using both arrays (top row) and only the 8-channel Tx/Rx coil (bottom row). Even with $R = 4$, the 3D DESS sequence can still provide high anatomical detail without introducing too much noise when both arrays are used. As expected, increasing the acceleration leads to reduced SNR in each case, but the combination of both arrays can compensate the SNR loss much better due to the lower g-factors. This is especially prominent in the zoomed region (K-N). Note that intensity correction was applied to the images.

To demonstrate the influence of the g-factor evaluation, Figure 4.8 shows the MR imaging results using the 3D DESS (Figure 4.8A-F) and the 2D PD TSE (Figure 4.8G-N) sequence in volunteer 1 with different acceleration factors. Despite the high spatial resolution of 0.74 mm isotropic for the 3D DESS sequence, acceleration factors of $R = 3$ and 4 do not degenerate the SNR impression of the images (Figure 4.8B-C), while the 8-channel Tx/Rx coil alone cannot provide competitive image quality with these relatively high acceleration factors (Figure 4.8D-F). This is exemplified by the enhanced noise visible in Figure 4.8F caudal to the shoulder joint. Similar observations can also be made for the 2D PD TSE in transversal orientation (Figure 4.8G-J). Qualitatively, the anatomical details are mostly preserved if the image with $R = 2$ (Figure 4.8G) is compared to the image with $R = 3$ (Figure 4.8H) for the combination of both arrays. For the 8-channel Tx/Rx coil alone, the impact of noise on image quality between images with $R = 2$ (Figure 4.8I) and $R = 3$ (Figure 4.8J) is more severe, and the influence of enhanced noise can be observed in Figure 4.8J lateral to the shoulder joint. In the zoomed version (Figure 4.8K-N) of the TSE sequence, the difference between the two RF coil setups can be appreciated for both $R = 2$ and $R = 3$.

The examination in a 51-year-old female patient (Figure 4.9) using a PD-weighted TSE sequence with fat saturation ($0.4 \times 0.4 \times 2.0 \text{ mm}^3$) in para-coronal orientation shows very good and clinically convincing image quality. This is substantiated by several details and findings visible in the image, like the narrowing of the subacromial space caused by an osteophyte (Figure 4.9A), a partial tendon tear (Figure 4.9B) that was confirmed by subsequent arthroscopy, and signs of acromioclavicular joint arthrosis indicated by irregularities of the cartilage surface, joint fluid, and edema in the joint capsule (Figure 4.9C).



Figure 4.9: Para-coronal PD-weighted TSE sequence with fat saturation (0.4x0.4x2.0 mm³) in a 51-year-old female patient (165 cm, 66 kg) with impingement syndrome of the right shoulder. Both RF arrays were used for the image acquisition. Narrowing of the subacromial space caused by an osteophyte (A) is apparent, and signal alterations with areas of high signal intensity in the supraspinatus tendon (B) suggest a partial tendon tear. Furthermore, signs of acromioclavicular joint arthrosis are obvious with cartilage surface irregularities, joint fluid, and edema of the joint capsule (C).

4.4 Discussion

In this work, we evaluated the performance of an 8-channel transceiver 7-channel receive RF shoulder coil setup on the bench including safety assessment using field measurements and full SAR simulations in different body models. We demonstrated in vivo 7T MRI measurements with high image quality of the left and the right shoulder in volunteers as well as first imaging results in a patient. High SNR gain provided by the 7-channel Rx array and good performance regarding g-factors were shown.

Regarding the safety evaluation, measurements of the H-field in the phantom indicated that the RF coil model for the simulations was reasonable. Therefore, the SAR distribution for in vivo measurements could be assessed using RF simulations with heterogeneous body models, and real-time SAR supervision using virtual observation points was used to guarantee safe use. Influence of different positioning and tissue distributions were minimized by positioning the subjects with respect to the coil similar to the simulation. In addition, a twofold safety margin was included by restricting the SAR limits to the normal mode. Measurements in the phantom additionally indicated that the 7-channel Rx-only coil can be left out of the SAR calculation since only a neglectable impact on the field distribution could be measured, which was within the measurement error.

Detuning efficiency was also measured on the bench. With about -19 dB of detuning efficiency, safe use could be verified. The preamplifier decoupling provides an additional isolation of about -11 dB between the receive channels of the 7-channel Rx coil during signal reception. Together with intrinsic decoupling and overlap between the 7 Rx-only loops, this is sufficient even for higher acceleration factors.

The presented RF coil setup provides a maximum noise correlation coefficient of 0.47 in a phantom and 0.40 in volunteers. The noise correlation does depend on the specific loading conditions of the coil. The load dependency regarding the noise

correlation coefficient was quantified using the standard deviation of measurements in four different volunteers. Maximum values of about 9% for one coil channel combination and an average value of about 3% were measured. Keeping these values in mind and the fact that the position of the 7-channel Rx coil varies between volunteers as showed by the SNR gain maps, the presented 8-channel transceiver 7-channel receive RF coil setup seems to be robust regarding different loading conditions at least with respect to the noise correlation coefficients.

Robust SNR gain for the left and right side in both phantom and volunteers could be demonstrated. For measurements in volunteers, the impact of the positioning of the RF arrays on the subject's shoulder has to be noted; nonetheless, the overall improvement in image quality justifies the use of the 7-channel Rx-only coil since it provides an up to 10-fold SNR gain near the surface of the subjects. In deeper-lying regions, the SNR gain due to the 7-channel Rx array drops as expected. Nevertheless, an SNR increase of about 35-86% can still be achieved at 41 mm depth from the skin while at 32 mm depth from the skin, values in the range of 71-282% can be expected. However, the quantitative SNR gain does not necessarily translate in a better qualitative impression for unaccelerated images since the SNR of the 8Tx/Rx coil is already so high that the images do not appear noisy.

In the context of the g-factor evaluation, a benefit of the additional 7-channel Rx-only coil can be stated without exception. In none of the comparisons did the 8-channel Tx/Rx array alone perform better, and the parallel imaging capabilities are consequently consistently improved by using the additional 7-channel Rx-only coil. This is important to fulfill the high SNR requirement for high spatial resolution shoulder imaging, also for higher acceleration factors, which was motivation for developing the coil setup. Regarding left and right shoulder imaging in volunteers at higher acceleration factors, a slightly increased performance could be observed for the left shoulders. However, the small number of subjects and the fact that RF

coil positioning itself might be the reason for this difference do not allow a clear judgment about whether or not there is an actual left-right difference.

The presented coil setup can be used for MR imaging of both the left and the right shoulder at 7T; the available space was sufficient for all investigated subjects. While the amount of space offered in the y-direction theoretically allows for even larger subjects, the size of the 8-channel Tx/Rx coil limits the patient size to about 520 mm in the x-direction. The 7-channel Rx-only array can further limit the available space in the x- or y-direction depending on the positioning, but this is only an issue for a comparably small patient population.

In transversal orientation, the 8-channel Tx/Rx coil allows for coverage of the entire shoulder volume, and the contribution of the different RF channels is approximately equal. Differences regarding power efficiency between phantom and volunteer measurements not only occur due to the different electric properties and the heterogeneous tissue distribution in the volunteers, but also due to different loading conditions and the resulting differences in RF coupling between neighboring elements. As values of about $300 \text{ nT/W}^{0.5}$ can be reached in close proximity to the elements, flip angles of 55° and higher are possible for a 1 ms rectangular pulse with 18 W per channel. In the same constellation the RF coil setup from reference (34) reaches values of about 45° . Similarly, both RF coil designs allow parallel imaging acceleration factors of up to $R=3$ without compromising image quality. In this work, excellent performance even with $R=4$ was shown for the gradient-echo DESS sequence. In general, the benefit of using the 7-channel Rx-only coil in addition to the 8-channel Tx/Rx RF coil was unambiguously observed for protocols with high acceleration factors, resulting in up to 2 minutes shorter acquisition times and lower SAR load, both highly improving workflow for a prospective clinical follow-up study. In reference (34), B_1^+ twisting (transmit and receive profiles are twisted in opposite directions) was reported, and this can also be observed with the presented RF coil setup as indicated by the evaluation of the power efficiency. Furthermore, it was reported that lower flip angles were reached

in the right shoulder compared to the left shoulder. A similar observation could not be observed with the presented coil setup. For the presented RF coil setup, the maximum possible B_1^+ amplitude in the shoulder of 19 μT that can be achieved for a dedicated phase-only shim if the power limits of the system are exploited, corresponds well to the values reported from several publications of coil setups for 7T imaging (16,56–58). Due to the geometry of both coils the setup can theoretically also be used in other body regions e.g. for hip imaging. Yet, this is not addressed in this work.

In the presented study, a single phase-only shim was sufficient in principle to cover the region of interest and provided a nearly homogeneous image. Techniques like TIAMO (11,12) could potentially be used to further homogenize the imaging region.

In future clinical protocols, the isotropic 3D DESS sequence with higher acceleration factors of e.g. $R = 4$ could potentially be used as a fast high-resolution, high-quality anatomic overview since it covers the entire volume of the shoulder in a comparably short time. Based on the resulting multi-planar reformations, a more detailed planning of subsequent measurements can be achieved. Furthermore, higher parallel acceleration factors have a positive impact on SAR, especially in clinical workhorse TSE sequences, which additionally improves workflow in 7 T UHF protocols for fast high spatial resolution shoulder imaging.

4.5 Conclusions

In this work, we presented a 7T two-array RF coil setup for shoulder imaging featuring an 8-channel Tx/Rx coil based on microstrip lines with meanders and a 7-channel Rx-only coil based on loops. Measurements on the bench and the safety evaluation demonstrate the capability of the RF coil setup to conduct safe imaging at 7T. Consequently, the setup was tested in both a body-sized phantom and in four volunteers, where distinct SNR gain and benefits with respect to g-factors could be demonstrated in the left and the right shoulder. Anatomical images in volunteers and in a patient demonstrate the high performance of the RF coil setup to acquire high-resolution 7T shoulder imaging with excellent image quality.

Acknowledgements

The research leading to these results has received funding from the European Research Council under the European Union's Seventh Framework Programme (FP/2007-2013) / ERC Grant Agreement n. 291903 MRexcite. The study was partly supported by a research grant ("IFORES") of the University Duisburg-Essen, awarded to one of the co-authors (A. Lazik-Palm).

Conflicts of Interest

The authors have no relevant conflicts of interest to disclose.

References

1. Kraff O, Quick HH. 7T: Physics, safety, and potential clinical applications. *J Magn Reson Imaging* 2017;1–17.
2. Hoult DI, Phil D. Sensitivity and Power Deposition in a High-Field Imaging Experiment. *J Magn Reson Imaging* 2000;67:46–67.
3. Yang QX, Wang J, Zhang X, Collins CM, Smith MB, Liu H, Zhu X-H, Vaughan JT, Ugurbil K, Chen W. Analysis of wave behavior in lossy dielectric samples at high field. *Magn Reson Med* 2002;47(5):982–9.
4. Vaughan JT, Garwood M, Collins CM, Liu W, Delabarre L, Adriany G, Andersen P, Merkle H, Goebel R, Smith MB, et al. 7T vs. 4T: RF power, homogeneity, and signal-to-noise comparison in head images. *Magn Reson Med* 2001;46(1):24–30.
5. Wiesinger F, Boesiger P, Pruessmann KP. Electrodynamics and ultimate SNR in parallel MR imaging. *Magn Reson Med* 2004;52(2):376–90.
6. Ohliger MA, Grant AK, Sodickson DK. Ultimate intrinsic signal-to-noise ratio for parallel MRI: electromagnetic field considerations. *Magn Reson Med* 2003;50(5):1018–30.
7. Pohmann R, Speck O, Scheffler K. Signal-to-Noise Ratio and MR Tissue Parameters in Human Brain Imaging at 3 , 7 , and 9 . 4 Tesla Using Current Receive Coil Arrays. *Magn Reson Med* 2016;75(2):1–9.
8. Regatte RR, Schweitzer ME. Novel contrast mechanisms at 3 tesla and 7 tesla. *Semin Musculoskelet Radiol* 2008;12(3):266–80.

9. Collins CM, Liu W, Swift BJ, Smith MB. Combination of optimized transmit arrays and some receive array reconstruction methods can yield homogeneous images at very high frequencies. *Magn Reson Med* 2005;54(6):1327–32.
10. Mao W, Smith MB, Collins CM. Exploring the limits of RF shimming for high-field MRI of the human head. *Magn Reson Med* 2006;56(4):918–22.
11. Orzada S, Maderwald S, Poser BA, Johst S, Kannengiesser S, Ladd ME, Bitz AK. Time-interleaved acquisition of modes: an analysis of SAR and image contrast implications. *Magn Reson Med* 2012;67(4):1033–41.
12. Orzada S, Maderwald S, Poser BA, Bitz AK, Quick HH, Ladd ME. RF excitation using time interleaved acquisition of modes (TIAMO) to address B1 inhomogeneity in high-field MRI. *Magn Reson Med* 2010;64(2):327–33.
13. Katscher U, Börnert P, Leussler C, van den Brink JS. Transmit SENSE. *Magn Reson Med* 2003;49(1):144–50.
14. Grissom W, Yip C, Zhang Z, Stenger VA, Fessler JA, Noll DC. Spatial domain method for the design of RF pulses in multicoil parallel excitation. *Magn Reson Med* 2006;56(3):620–9.
15. Bitz AK, Brote I, Orzada S, Kraff O, Maderwald S, Quick HH, Yazdanbakhsh P, Solbach K, Bahr A, Bolz T, et al. An 8-channel add-on RF shimming system for whole-body 7 Tesla MRI including real-time SAR monitoring. *Proc Intl Soc MRM* 17 2009. p. 4767.
16. Avdievich NI. Transceiver-Phased Arrays for Human Brain Studies at 7 T. *Appl Magn Reson* 2013;41:483–506.

17. Winter L, Kellman P, Renz W, Gräßl A, Hezel F, Thalhammer C, von Knobelsdorff-Brenkenhoff F, Tkachenko V, Schulz-Menger J, Niendorf T. Comparison of three multichannel transmit/receive radiofrequency coil configurations for anatomic and functional cardiac MRI at 7.0T: implications for clinical imaging. *Eur Radiol* 2012;22(10):2211–20.
18. Kraff O, Bitz AK, Kruszona S, Orzada S, Schaefer LC, Theysohn JM, Maderwald S, Ladd ME, Quick HH. An eight-channel phased array RF coil for spine MR imaging at 7 T. *Invest Radiol* 2009;44(11):734–40.
19. Shajan G, Kozlov M, Hoffmann J, Turner R, Scheffler K, Pohmann R. A 16-channel dual-row transmit array in combination with a 31-element receive array for human brain imaging at 9.4 T. *Magn Reson Med* 2014;71(2):870–9.
20. Brunner DO, De Zanche N, Froehlich J, Baumann D, Pruessmann KP. A symmetrically fed microstrip coil array for 7T. *Proc Intl Soc MRM* 15 2007. p. 448.
21. Metzger GJ, Snyder C, Akgun C, Vaughan T, Ugurbil K, Van de Moortele P-F. Local B1+ shimming for prostate imaging with transceiver arrays at 7T based on subject-dependent transmit phase measurements. *Magn Reson Med* 2008;59(2):396–409.
22. Orzada S, Bahr A, Bolz T. A novel 7 T microstrip element using meanders to enhance decoupling. *Proc Intl Soc MRM* 16 2008. p. 2979.
23. Orzada S, Kraff O, Schäfer LC, Brote I, Bahr A, Bolz T, Maderwald S, Ladd ME, Bitz AK. 8-channel transmit/receive head coil for 7 T human imaging

- using intrinsically decoupled strip line elements with meanders. *Proc Intl Soc MRM* 17 2009;3010.
24. Maderwald S, Orzada S, Schäfer LC, Bitz AK, Brote I, Kraff O, Theysohn JM, Ladd ME, Ladd SC, Quick HH. 7T Human in vivo Cardiac Imaging with an 8-Channel Transmit/Receive Array. *Proc Intl Soc MRM* 17 2009. p. 822.
 25. Aussenhofer SA, Webb AG. An eight-channel transmit/receive array of TE₀₁ mode high permittivity ceramic resonators for human imaging at 7T. *J Magn Reson Elsevier Inc.*; 2014;243:122–9.
 26. Oezerdem C, Winter L, Graessl A, Paul K, Els A, Weinberger O, Rieger J, Kuehne A, Dieringer M, Hezel F, et al. 16-channel bow tie antenna transceiver array for cardiac MR at 7.0 tesla. *Magn Reson Med* 2016;75(6):2553–65.
 27. Lakshmanan K, Cloos M, Brown R, Shepherd T, Wiggins G. A Four Channel Transmit Receive " Loopole " Array for Spine Imaging at 7 . 0 Tesla. *Proc Intl Soc MRM* 23 2015;628.
 28. Wiggins GC, Zhang B, Cloos M, Lattanzi R, Chen G, Lakshmanan K, Haemer G, Sodickson DK. Mixing loops and electric dipole antennas for increased sensitivity at 7 Tesla. *Proc Intl Soc MRM* 21 2013;2737.
 29. Shajan G, Mirkes C, Buckenmaier K, Hoffmann J, Pohmann R, Scheffler K. Three-layered radio frequency coil arrangement for sodium MRI of the human brain at 9.4 Tesla. *Magn Reson Med* 2016;75(2):906–16.
 30. Raaijmakers AJE, Ipek O, Klomp DWJ, Possanzini C, Harvey PR, Lagendijk JJW, van den Berg CAT. Design of a radiative surface coil array element at 7

- T: the single-side adapted dipole antenna. *Magn Reson Med* 2011;66(5):1488–97.
31. Voogt IJ, Klomp DWJ, Hoogduin H, Luttje MP, Luijten PR, van den Berg CAT, Raaijmakers AJE. Combined 8-channel transceiver fractionated dipole antenna array with a 16-channel loop coil receive array for body imaging at 7T. *Proc Intl Soc MRM* 23 2015. p. 631.
 32. Rietsch SHG, Quick HH, Orzada S. Impact of different meander sizes on the RF transmit performance and coupling of microstrip line elements at 7 T. *Med Phys* 2015;42(8):4542–52.
 33. Roemer PB, Edelstein WA, Hayes CE, Souza SP, Mueller OM. The NMR phased array. *Magn Reson Med* 1990;16(2):192–225.
 34. Brown R, Deniz CM, Zhang B, Chang G, Sodickson DK, Wiggins GC. Design and Application of Combined 8-Channel Transmit and 10-Channel Receive Arrays and Radiofrequency Shimming for 7-T Shoulder Magnetic Resonance Imaging. *Invest Radiol* 2014;49(1):35–47.
 35. Trattnig S, Zbýň Š, Schmitt B, Friedrich K, Juras V, Szomolanyi P, Bogner W. Advanced MR methods at ultra-high field (7 Tesla) for clinical musculoskeletal applications. *Eur Radiol* 2012;22(11):2338–46.
 36. Regatte RR, Schweitzer ME. Ultra-high-field MRI of the musculoskeletal system at 7.0T. *J Magn Reson Imaging* 2007;25(2):262–9.
 37. Krug R, Carballido-Gamio J, Banerjee S, Stahl R, Carvajal L, Xu D, Vigneron D, Kelley DAC, Link TM, Majumdar S. In vivo bone and cartilage MRI using fully-balanced steady-state free-precession at 7 Tesla. *Magn Reson Med*

- 2007;58(6):1294–8.
38. Banerjee S, Krug R, Carballido-Gamio J, Kelley DAC, Xu D, Vigneron DB, Majumdar S. Rapid in vivo musculoskeletal MR with parallel imaging at 7T. *Magn Reson Med* 2008;59(3):655–60.
 39. Welsch GH, Mamisch TC, Hughes T, Zilkens C, Quirbach S, Scheffler K, Kraff O, Schweitzer ME, Szomolanyi P, Trattnig S. In vivo biochemical 7.0 Tesla magnetic resonance: preliminary results of dGEMRIC, zonal T2, and T2* mapping of articular cartilage. *Invest Radiol* 2008;43(9):619–26.
 40. Zuo J, Bolbos R, Hammond K, Li X, Majumdar S. Reproducibility of the quantitative assessment of cartilage morphology and trabecular bone structure with magnetic resonance imaging at 7 T. *Magn Reson Imaging* 2008;26(4):560–6.
 41. Chang G, Wiggins GC, Xia D, Lattanzi R, Madelin G, Raya JG, Finnerty M, Fujita H, Recht MP, Regatte RR. Comparison of a 28-channel receive array coil and quadrature volume coil for morphologic imaging and T2 mapping of knee cartilage at 7T. *J Magn Reson Imaging* 2012;35(2):441–8.
 42. Ji Y, Waiczies H, Winter L, Neumanova P, Hofmann D, Rieger J, Mekle R, Waiczies S, Niendorf T. Eight-channel transceiver RF coil array tailored for ¹H/¹⁹F MR of the human knee and fluorinated drugs at 7.0 T. *NMR Biomed* 2015;28(6):726–37.
 43. Chang G, Friedrich KM, Wang L, Vieira RLR, Schweitzer ME, Recht MP, Wiggins GC, Regatte RR. MRI of the Wrist at 7 Tesla using an 8 Channel Array Coil Combined with Parallel Imaging : Preliminary Results. *J*

Magn Reson 2011;31(3):740–6.

44. Kraff O, Bitz AK, Dammann P, Ladd SC, Ladd ME, Quick HH. An eight-channel transmit/receive multipurpose coil for musculoskeletal MR imaging at 7 T. *Med Phys* 2010;37(12):6368.
45. Orzada S, Bitz AK, Schäfer LC, Ladd SC, Ladd ME, Maderwald S. Open design eight-channel transmit/receive coil for high-resolution and real-time ankle imaging at 7 T. *Med Phys* 2011;38(3):1162–7.
46. Theysohn JM, Kraff O, Theysohn N, Orzada S, Landgraeber S, Ladd ME, Lauenstein TC. Hip imaging of avascular necrosis at 7 Tesla compared with 3 Tesla. *Skeletal Radiol* 2014;43(5):623–32.
47. Theysohn JM, Kraff O, Orzada S, Theysohn N, Classen T, Landgraeber S, Ladd ME, Lauenstein TC. Bilateral hip imaging at 7 Tesla using a multi-channel transmit technology: initial results presenting anatomical detail in healthy volunteers and pathological changes in patients with avascular necrosis of the femoral head. *Skeletal Radiol* 2013;42(11):1555–63.
48. Lazik-Palm A, Kraff O, Johst S, Quick HH, Ladd ME, Geis C, Körsmeier K, Landgraeber S, Theysohn JM. Morphological and Quantitative 7 T MRI of Hip Cartilage Transplants in Comparison to 3 T—Initial Experiences. *Invest Radiol* 2016;51(9):552–9.
49. Lattanzi R, Sodickson DK. Ideal current patterns yielding optimal signal-to-noise ratio and specific absorption rate in magnetic resonance imaging: computational methods and physical insights. 2012;68(1):286–304.
50. Springer E, Bohndorf K, Juras V, Szomolanyi P, Zbyn S, Schreiner MM,

- Schmitt B, Trattnig S. Comparison of Routine Knee Magnetic Resonance Imaging at 3 T and 7 T. *Invest Radiol* 2017;52(1):42–54.
51. Seeber DA, Jevtic J, Menon A. Floating shield current suppression trap. *Concepts Magn Reson Part B Magn Reson Eng* 2004;21(1):26–31.
 52. Eichfelder G, Gebhardt M. Local specific absorption rate control for parallel transmission by virtual observation points. *Magn Reson Med* 2011;66(5):1468–76.
 53. Christ A, Kainz W, Hahn EG, Honegger K, Zefferer M, Neufeld E, Rascher W, Janka R, Bautz W, Chen J, et al. The Virtual Family--development of surface-based anatomical models of two adults and two children for dosimetric simulations. *Phys Med Biol* 2010;55(2):N23–38.
 54. Brunheim S, Orzada S, Johst S, Gratz M, Voelker MN, Kraff O, Floeser M, Bitz AK, Ladd ME, Quick HH. Combining B1 mapping with TIAMO for fast and accurate multi-channel RF shimming in 7 Tesla body MRI. *Proc Intl Soc MRM* 24 2016;3186.
 55. Lazik-Palm A, Kraff O, Geis C, Johst S, Goebel J, Ladd ME, Quick HH, Theysohn JM. Morphological imaging and T2 and T2* mapping of hip cartilage at 7 Tesla MRI under the influence of intravenous gadolinium. *Eur Radiol European Radiology*; 2016;26(11):3923–31.
 56. Raaijmakers AJE, Italiaander M, Voogt IJ, Luijten PR, Hoogduin JM, Klomp DWJ, Van Den Berg CAT. The fractionated dipole antenna: A new antenna for body imaging at 7 Tesla. *Magn Reson Med* 2016;75(3):1366–74.
 57. Aussenhofer SA, Webb AG. High-permittivity solid ceramic resonators for

high-field human MRI. *NMR Biomed* 2013;26(11):1555–61.

58. Ertürk MA, Raaijmakers AJE, Adriany G, Uğurbil K, Metzger GJ. A 16-channel combined loop-dipole transceiver array for 7 Tesla body MRI. *Magn Reson Med* 2017;77:884–94.

Chapter 5 7T ultra-high field body MR imaging with an 8-channel transmit / 32-channel receive radiofrequency coil array*

Purpose

In this work a combined body coil array with 8 transmit/receive (Tx/Rx) meander elements and with 24 receive-only (Rx) loops (8Tx/32Rx) was developed and evaluated in comparison to an 8-channel transmit/receive body array (8Tx/Rx) based on meander elements serving as the reference standard.

Methods

Systematic evaluation of the RF array was performed on a body-sized phantom. Body imaging at 7T was performed in 6 volunteers in the body regions pelvis, abdomen, and heart. Coil characteristics such as signal-to-noise-ratio, acceleration capability, g-factors, S-parameters, noise correlation, and B1+ maps were assessed. Safety was ensured by numerical simulations using a coil model validated by dosimetric field measurements.

Results

Meander elements and loops are intrinsically well decoupled with a maximum coupling value of -20.5 dB. Safe use of the 8Tx/32Rx array could be demonstrated. High gain in signal-to-noise ratio (33% in the subject's center) could be shown for the 8Tx/32Rx array compared to the 8Tx/Rx array. Improvement in acceleration capability in all investigations could be demonstrated. For example, the 8Tx/32Rx array provides lower g-factors in the right-left and anterior-posterior directions

with $R = 3$ undersampling as compared to the 8Tx/Rx array using $R = 2$. Both arrays are very similar regarding their RF transmit performance. Excellent image quality in the investigated body regions could be achieved with the 8Tx/32Rx array.

Conclusion

In this work we show that a combination of 8 meander elements and 24 loop receive elements is possible without impeding transmit performance. Improved SNR and g-factor performance compared to an RF array without these loops is demonstrated. Body MRI at 7T with the 8Tx/32Rx array could be accomplished in the heart, abdomen, and pelvis with excellent image quality.

*published as: Rietsch SHG, Orzada S, Maderwald S, Brunheim S, Philips BWJ, Scheenen TWJ, Ladd ME, Quick HH. 7T ultra-high field body MR imaging with an 8-channel transmit / 32-channel receive radiofrequency coil array. Medical Physics 2018, 45(7):2978-2990

5.1 Introduction

In magnetic resonance imaging (MRI), radiofrequency (RF) coil arrays are used both to transmit pulses for spin excitation and refocusing and to receive the MR signal. A coil used for transmission (Tx) primarily needs to balance the B1+ amplitude and the specific absorption rate (SAR) to obtain a high SAR efficiency. A coil used for reception (Rx) must fulfill other performance criteria: for maximum signal-to-noise-ratio (SNR), several receive (Rx) coil elements should be placed closely around the target anatomy (1); also, a high number of receive elements oriented along the phase-encoding direction allows for high acceleration factors in this direction during image acquisition (2). For simultaneous multi-slice acquisitions, it is also important to have multiple rows of coil elements along the slice-encoding direction. Consequently, a SAR-efficient, large-volume, RF body coil fed by one, two or sometimes four ports for transmit in combination with dedicated receive-only coil arrays for high SNR and high acceleration factors are typically used for clinical body MRI at 1.5T and 3T.

At the ultra-high field (UHF) strength of 7T, the high Larmor frequency of protons at 297 MHz implies short RF excitation wavelengths (about 13 cm) in the human body. This leads to constructive and destructive interference of the RF fields inside the human tissue that cause signal dropouts and RF hotspots, which complicates the SAR supervision for the subject (3,4). To mitigate signal inhomogeneity in the images, techniques like RF shimming (5,6), transmit SENSE (7,8), and TIAMO (9,10) can be employed. A prerequisite for these techniques is a multi-channel transmit coil with elements that can be individually fed either with identical RF pulses that are modulated with differing complex weighting factors or with unique RF pulses.

As the building blocks of such transmit array designs for 7T MRI, several different element types have been investigated including micro striplines (11–14), loops (15–17), dipole antennas (18), and meander elements (ME) (19,20). Meander elements are micro stripline RF elements with meander structures at both ends that

are used to shape the RF excitation profile of the elements. Since it is possible to minimize coupling between adjacent ME (21), this element type is well suited for the implementation of transmit coils, e.g. the 8-channel Tx/Rx array presented in reference (22) for body imaging. Due to the poor transmit efficiency and the lack of adequate RF power on most 7 Tesla systems, such transmit arrays for body imaging are typically placed very close to or directly on the anatomy of interest, and the elements are operated as transmit/receive (23–25). In reference (24) the authors present a combination of 8 fractionated dipole antennas and 8 loops. All elements were used for transmit and receive and loops are consequently about 1 cm away from the subject's skin. This is useful to optimize the SAR efficiency but it can lead to SNR loss compared to close-fitting receive loops placed directly on the subject's surface. An alternative to the transmit/receive design is the separation into transmit-only and receive-only coil elements in one array (26). This approach combines the advantage of a power-efficient transmission and high-SNR reception. Yet, the transmit elements were not used for receive in this abstract and the additional loop elements reduced the transmit efficiency as stated by the authors.

Consequently, in this work we present an 8-channel-transmit-32-channel-receive array with 8 Tx/Rx meander elements in combination with 24 receive-only loops. This 8Tx/32Rx RF array is evaluated on the bench, in a phantom, and in volunteer measurements on a 7T MRI system. The performance of the new 8Tx/32Rx array is compared to an 8Tx/Rx RF array (22) with similar transmit geometry that serves as a reference standard. High-resolution 7T MR imaging in the pelvis of a volunteer is also performed with the new 8Tx/32Rx array.

5.2 Methods

The local ethics committee approved all in-vivo 7 Tesla MRI examinations in the presented study. All subjects gave written informed consent. Altogether, six healthy volunteers (V1: 40-year-old male, 186 cm, 80 kg, V2: 36-year-old male, 172 cm, 65 kg, V3: 35-year-old male, 175 cm, 78 kg, V4: 26-year-old male, 180 cm, 76 kg, V5: 34-year-old male, 189 cm, 81 kg, V6: 22-year-old female, 158 cm, 62 kg) were examined.

Array Construction and Bench Measurements

Figure 5.1a shows the 8Tx/Rx RF body array presented in reference (22), which served as the reference standard against which the new 8Tx/32Rx array coil setup (Figure 5.1b) was compared. The transmit arrays of both coils are identical and consist of 8 identical meander elements (ME): micro stripline elements with a length of 250 mm in z-direction (orientation of the magnet bore), 100 mm in x-direction (left-right), 18 mm in y-direction (up-down), and 65-mm-wide meander structures with 2 mm spacing at both ends of the stripline. The distance to the subject under investigation is fixed at 30 mm by the housing. This element type shows good decoupling characteristics to neighboring elements and advantageous field characteristics (21) when compared to the standard micro stripline. Both arrays are separated into a posterior bottom part (4 ME) that fits into the patient table of the 7T system and an anterior top part consisting of a semi-flexible belt that connects another 4 ME. This design allows imaging of a wide range of patient sizes and body regions (e.g. thorax, abdomen, and pelvis). All housings are made of polycarbonate, which is robust, electrically insulating, has low dielectric losses at 297 MHz and low signal for short echo times.

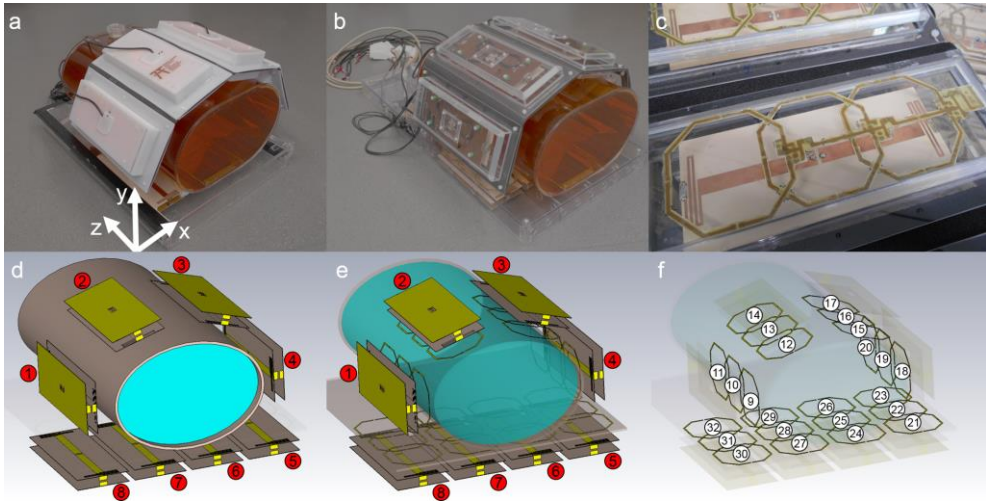


Figure 5.1: Photographs of the 8Tx/Rx (a) and the 8Tx/32Rx (b) coils loaded with a body-sized phantom. Both coils consist of a semi-flexible belt with 4 building blocks on top (anterior) and a rigid base with 4 building blocks on the bottom (posterior) that is placed on the patient table of the 7T MRI system. Each of the 8 building blocks of the 8Tx/32Rx coil is made up of one micro stripline with meanders and three overlapping loops (c). Simulation models of the 8Tx/Rx (d) and the 8Tx/32Rx (e,f) coil with numbering of the coil elements (1-8 Tx/Rx meander striplines, 9-32 Rx loop elements). The simulation model (excluding loops) was validated by field probe measurements in the y-z and x-z planes.

In the 8Tx/Rx array the ME elements serve as transmit and receive elements. The same holds for the newly developed 8Tx/32Rx array, but in addition, this array incorporates 24 Rx-only loops. For this purpose, each ME is combined with 3 loops to form a building block (Figure 5.1c). The size of the housings on top is 397 mm in z-direction, 168 mm in x-direction, and 56 mm in y-direction. The bottom housing is a cuboid (900 mm in z-, 450 mm in x-, and 59 mm in y-direction) including a 4-mm-thick cover and 5-mm walls between the building blocks (11-mm spacing) and along the edges.

To fabricate the loops, a Protomat H60 milling machine (LPKF Laser & Electronics AG, Garbsen, Germany) was used to extract three loops with overlap between nearest neighbors from a 1-mm-thick FR4 plate with 35- μm copper cladding. The loops are of rectangular shape (10 cm size) with chamfered edges and 3.9 pF capacitors (11 series Dalian Dalicap Co.,Ltd., China) are equally distributed along each side. Cable traps near the feeding point of the loops were formed from windings in semi-rigid cable and parallel capacitors. Active detuning of the loops is enabled by a PIN diode and a series inductance, which are both parallel to the capacitor at the feeding point. Simulation models of the arrays (Figures 5.1d-f) indicate the coil numbering used for further descriptions.

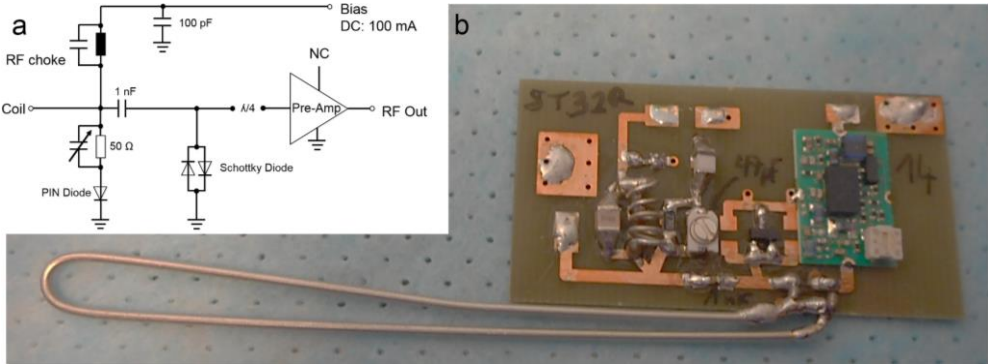


Figure 5.2: Circuit diagram of the preamplifier boards (a). The supply for the PIN diodes of both the coil and detuning circuit is isolated from RF by a RF choke and an additional 100 pF capacitor on top. To set the current of the PIN diodes during transmit, a resistance of 50 Ω is employed. Capacitors of 1 nF allow RF to pass while DC is blocked. In order to protect the preamplifier from high input power, a Schottky diode to ground is placed in front of a $\lambda/4$ semi-rigid cable (a,b) connected to the preamplifier input.

While for both arrays the 8 ME are connected to a custom-built T/R switch box via BNC connectors and RG 223U cables, separate preamplifier boards (Figure 5.2a,b) were designed to integrate low impedance preamplifiers (Wantcom, Chanhassen, MN, USA) and detuning bias for the loops. Preamplifier decoupling was realized by carefully trimming of the cable length.

Three Tim cables (Total imaging matrix, Siemens Healthcare GmbH, Erlangen, Germany) allow direct connection to the MR system receive channels. All coil elements were tuned to 297 MHz and S-parameter measurements were performed with the coil array in place on the abdomen of a male volunteer (34-year-old male, 189 cm, 81 kg) using a 2-port network analyzer (Agilent E5061A, Santa Clara, CA, USA). This network analyzer was also used to quantify preamplifier decoupling and detuning of the loaded (elliptical body-sized phantom, $\epsilon_r = 45$, $\sigma = 0.8 \text{ S m}^{-1}$) coil with a loosely coupled double pick-up probe.

Safety Evaluation

Safety was ensured by numerical simulations using coil models. The models were validated by measurements of the magnetic (H) and electric (E) fields in a phantom (27,28) for both coils. Measurements of the root mean square values of the H- and the E-field were accomplished with a custom-built automatic positioning device (27). Field probes for H- and E-field and the control unit EASY4 (all from SPEAG, Zurich, Switzerland) allowed for field measurements in a 2 mm raster in the y-z plane (coronal) and x-z plane (transversal) (Figure 5.1a) inside an elliptical body phantom filled with tissue-simulating liquid ($\epsilon_r = 46.4$, $\sigma = 0.86 \text{ S m}^{-1}$) to reflect a typical body load (Figure 5.1d,e). The elliptical phantom was made using a polycarbonate shell with dimensions 300 mm in y-, 210 mm in x-, 500 mm in z-direction and a 5-mm-thick wall. Measurements were performed up to a distance of 10 mm from the phantom wall.

To justify the use of subsequent simulations with a heterogeneous body model to determine RF power limits for SAR supervision, simulations of the above measurement setup with the phantom were first performed. By comparing measurements in the phantom performed with both coils with the corresponding simulations, the simulated coil models could be validated. All simulations were carried out in CST Microwave Studio (CST AG, Darmstadt, Germany) and were

calculated on a high-performance computing cluster with 4 Nvidia Tesla M2090 graphics cards.

A detailed description of the element modeling can be found in reference (21). Central feeding of the ME is introduced via RF ports on the bottom substrate and simulated in the CST network co-simulation using a $\lambda/2$ BalUn modeled as a transmission line (length = 330 mm, attenuation = 0.3 dB m^{-1}) and a matching network (11) with two capacitors in parallel and one capacitor in series. Identical capacitors of 1 pF at the ends of the element were introduced by lumped elements including their equivalent series resistance. Mesh refinement to 0.5 mm was ensured close to the meander structures in all simulations. Meander structures, strip line, ground plane, and wires connecting the ground plane and the upper conductors were modeled as perfect electric conductors, while the top substrate was modeled as Rogers C4003 ($\epsilon_r = 3.35$, $\tan\delta_{el} = 0.0027$).

For the phantom simulations, 36.6 million mesh cells were used and the phantom liquid was modeled corresponding to the measurements ($\epsilon_r = 46.4$, $\sigma = 0.86 \text{ S m}^{-1}$). Simulations using the body models Duke and Ella (2 mm isotropic resolution, about 80 tissue types) from the Virtual Family (29) were subsequently performed for further safety evaluation. Since the meander elements of both coils are identical, corresponding simulations and measurements should yield nearly identical results.

MRI Measurements

All MRI measurements were performed on a 7T whole-body research system (MAGNETOM 7T, Siemens Healthcare GmbH, Erlangen, Germany) using a custom-built 8-channel RF transmit chain add-on (30) for RF amplitude/phase shimming and the same custom-built 8-channel Tx/Rx switchbox for both arrays. The system is equipped with a gradient coil (AS095, Siemens Healthcare GmbH, Erlangen,

Germany) with maximum gradient amplitude 38 mT/m and maximum slew rate $200 \text{ Tm}^{-1}\text{s}^{-1}$ that provides sufficient coverage for body imaging in all dimensions.

To compare the two RF coils, phantom and volunteer data were acquired to assess noise correlation between the RF coil channels, g-factor maps, SNR maps using the circularly polarized mode, and B1+ maps. For B1+ mapping, the approach presented by Brunheim et al. (31) was utilized, which is based on two complementary shims in conjunction with the TIAMO (9,10) approach for data combination. Maximum values for the specific absorption rate using 10 g averages (maxSAR10g) were calculated based on the simulation results.

To investigate the impact of different GRAPPA (2) acceleration factors ($R = 1, 2, 3, 4, 6, 8$) in left-right direction on the image quality for both arrays, Volunteers 1-5 were scanned using a 2D FLASH gradient echo sequence in coronal orientation with TR/TE of 45/2.0 ms, 980 Hz/pixel bandwidth, and $1.3 \times 1.3 \times 3 \text{ mm}^3$ resolution. A subject-specific phase-only RF shim was used to homogenize the B1+ for the left or the right kidney.

In transversal orientation, a single RF shim was not sufficient to achieve satisfactory B1+ homogeneity in the entire slice for either coil. Consequently, the TIAMO (9,10) approach was utilized for 2D FLASH gradient echo sequences with a GRAPPA acceleration factor of $R = 2$ in anterior-posterior direction, TR/TE of 45/2.6 ms, and $1.3 \times 1.3 \times 3 \text{ mm}^3$ resolution. Transversal opposed-phase and fat-saturated (both 980 Hz/pixel) as well as T2*-weighted (750 Hz/pixel) sequences were separately acquired for Volunteers 1-5 with both arrays placed around the kidney region.

Cardiac imaging was performed in Volunteer 5 only using the 8Tx/32Rx array. Cardiac gating was achieved by using finger pulse oximetry. Four-chamber, short-axis, and LVOT (left ventricular outflow tract) images were all acquired with a FLASH 2D sequence during a single breath hold with TR/TE of 41/4.8 ms, 992 Hz/pixel bandwidth, and GRAPPA acceleration factor of 2 in anterior-posterior direction. The

four-chamber view was acquired in 20 s with $1.7 \times 1.7 \times 3 \text{ mm}^3$ resolution, the short-axis view in 21 s with $1.5 \times 1.5 \times 3 \text{ mm}^3$ resolution, and the LVOT view in 22 s with $1.5 \times 1.5 \times 3 \text{ mm}^3$ resolution.

Pelvic imaging using the 8Tx/32Rx array was accomplished in a female volunteer with a 3D multi-gradient-echo sequence and TIAMO for image homogenization. The repetition time was 16 ms and echoes were acquired at 2.56/6.98/11.4 ms. A high spatial resolution of $0.68 \times 0.68 \times 0.68 \text{ mm}^3$ was acquired. An acquisition time of TA = 9:40 min, a bandwidth of 325 Hz/pixel, and GRAPPA acceleration of 3 in left-right and 2 in posterior-anterior direction were employed.

5.3 Results

Array Construction and Bench Measurements

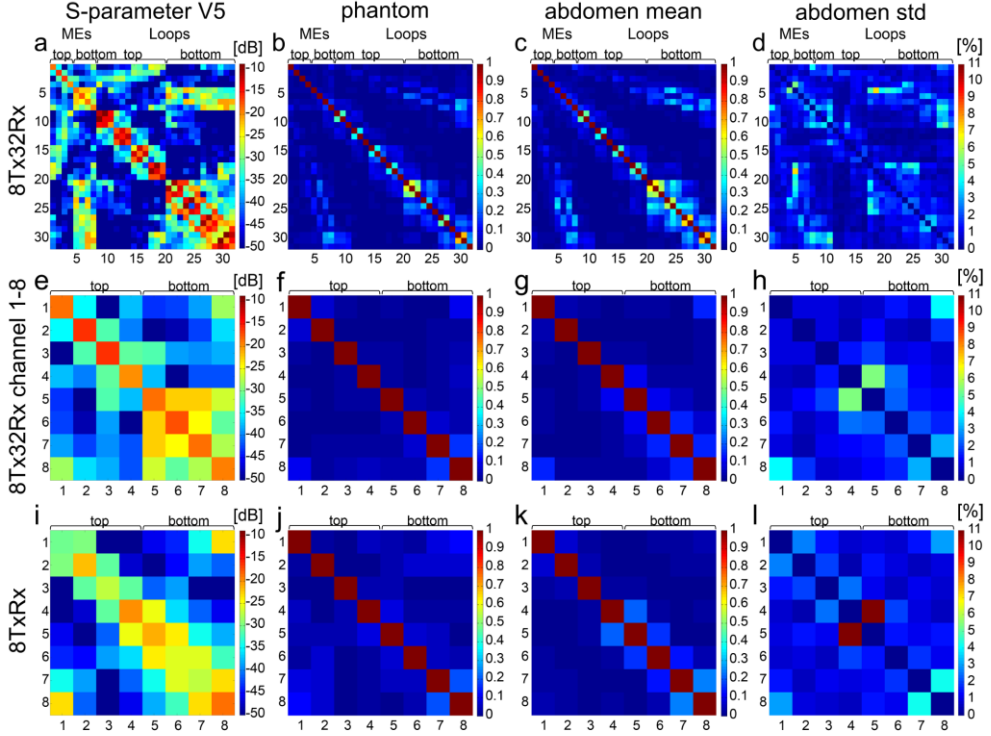


Figure 5.3: S-parameters and noise correlation coefficients of the 8Tx/32Rx coil (a-h) and the 8Tx/Rx coil (i-l). Here, the 8-channel Tx/Rx elements of the 8Tx/32Rx coil are also presented in a zoomed view (e-h). The S-parameters (a,e,i) were measured in the abdomen of Volunteer 5. Values on the diagonal represent reflection while off-diagonal elements represent coupling. Noise correlation coefficients (b-d,f,g,i-l) were measured in a body-sized phantom (b,f,j) and compared to the mean value of abdominal measurements in all 5 volunteers (c,g,k). Results between phantom and volunteer measurements are in good agreement. The standard deviation (std) among the volunteer measurements for both coils (d,h,l) indicate which elements are impacted most for changing loading conditions (e.g. channel 4 and 5 for the 8Tx/Rx coil). For both coils, the coupling is larger in the bottom array half for both element types. Bottom and top halves are well decoupled.

Figure 5.3 shows the S-parameters and noise correlation coefficients of the 8Tx/32Rx array (Figure 5.3a-h) and the 8Tx/Rx array (Figure 5.3i-l). The S-parameters (Figure 5.3a,e,i) were measured in the abdomen of Volunteer 5. While on average the reflection was low for the 8Tx/32Rx array (Figure 5.3a), the highest reflection was $S_{11} = -16.0$ dB for ME and $S_{11} = -11.3$ dB for loops. The highest coupling was $S_{12} = -22.4$ dB between MEs and $S_{12} = -8.7$ dB between loops. The highest coupling values occurred between neighboring loops due to the fixed overlap which could not be adjusted after construction. The ME and loops are intrinsically well decoupled with a maximum coupling of -20.5 dB even if the loops are not detuned.

For the 8Tx/Rx array (Figure 5.3i), the highest reflection is -19.0 dB and the highest coupling is -23.0 dB. If the transmit portions (Tx channels 1-8) of both arrays are compared with one another, the results are in good agreement. In general, for each array coupling is higher in the bottom (posterior) part compared to the top (anterior) part. This is true for the values between MEs and between loops as well as for the coupling values between loops and MEs.

Comparable findings were also observed for the noise correlation coefficients (Figure 5.3b,c,j,k). The noise correlation coefficient measurements were first acquired using a body-sized phantom (Figure 5.3b,f,j). Comparably high values are present between the first two loop elements of each building block (Figure 5.3b). The off-diagonal patterns between MEs and loops indicate that the noise correlation coefficients between MEs and loops in one building block are lower than values between those MEs and loops from neighboring building blocks. For both arrays the values between phantom measurements (Figure 5.3f,j) and the mean values of abdominal volunteer measurements (Figure 5.3g,k) are in good agreement, which adds support for the process chosen for the safety evaluation. Further investigations included the standard deviation (std) for values of the noise correlation coefficients measured in the volunteers (Figures 5.3d,h,l) to characterize the load dependency of the arrays. As can be seen for both arrays,

comparably high values for the standard deviation are present between channels 4 and 5, where top and bottom elements are adjacent to one another near the arms, which can also be observed for channels 1 and 8. Channel 5 of the 8Tx/32Rx array (Figure 5.3d) shows a relatively high standard deviation of the noise correlation coefficients to neighboring loops. This can most likely be attributed to the varying loading by the subjects with respect to the position of this element. Results for the noise correlation coefficients in the abdomen for Volunteers 1-5 can be found in Supporting Figure 5.S1.

For ME the maximum values for preamplifier decoupling was -9.0 dB; however, these elements are intrinsically well decoupled. For loops, the maximum value for preamplifier decoupling was -9.1 dB, and for these elements the intrinsic coupling is higher (up to -8.7 dB). Since preamplifier decoupling is additive to the intrinsic coupling, maximum values of about -17 dB were achieved. The maximum value for active detuning of the loops during transmit was -16.6 dB. Together with the intrinsic decoupling between loops and MEs, this was sufficient as the results of the safety evaluation demonstrate.

Safety Evaluation

Figure 5.4 shows a comparison between the results for E- and H-field simulations on the left and measurements on the right (root mean square values) for the 8Tx/32Rx array. The measurements were performed in the elliptical body-sized phantom. Good qualitative agreement is achieved for E- and H-fields in both the coronal and the sagittal central slices of the phantom. If the values of identical pixels are compared quantitatively, the mean percentage difference for the E-field is 14.4% (13.1% for regions underestimated by the simulation) in coronal and 6.8% (8.6%) in sagittal orientation. For the H-field, these values are 13.9% (5.8%) in coronal and 13.2% (8.5%) in sagittal orientation. With these results, the simulation model of the 8Tx/32Rx coil was considered validated, and a corresponding safety factor to account for the residual differences was introduced into the allowable RF power of the coil array.

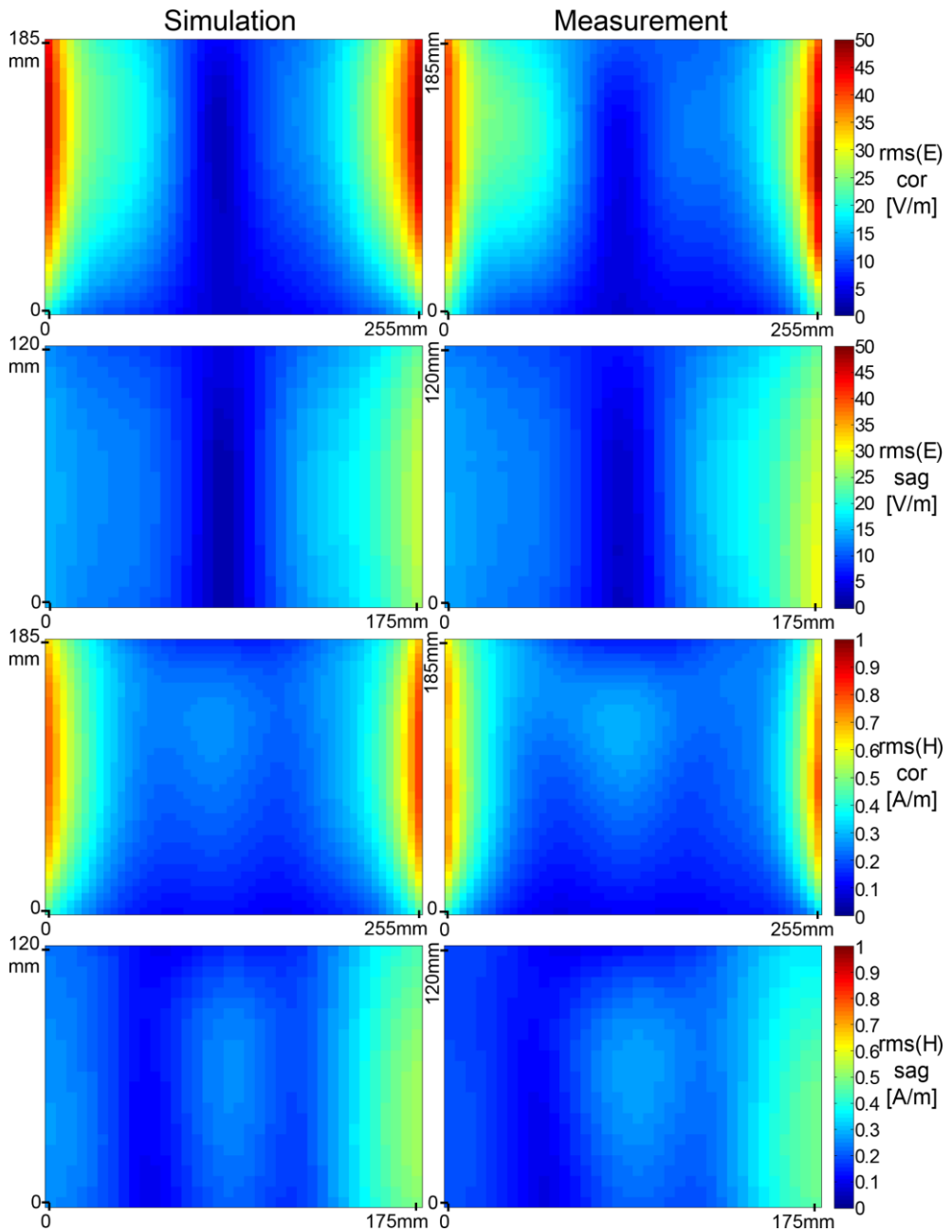


Figure 5.4: Simulated (left column) and measured (right column) E- and H-field magnitudes for the 8Tx/32Rx coil show good qualitative agreement. Field root mean square (rms) values were evaluated in identical coronal and sagittal planes. The elliptical body-sized phantom filled with tissue-simulating liquid was used (dimensions indicated for each plot).

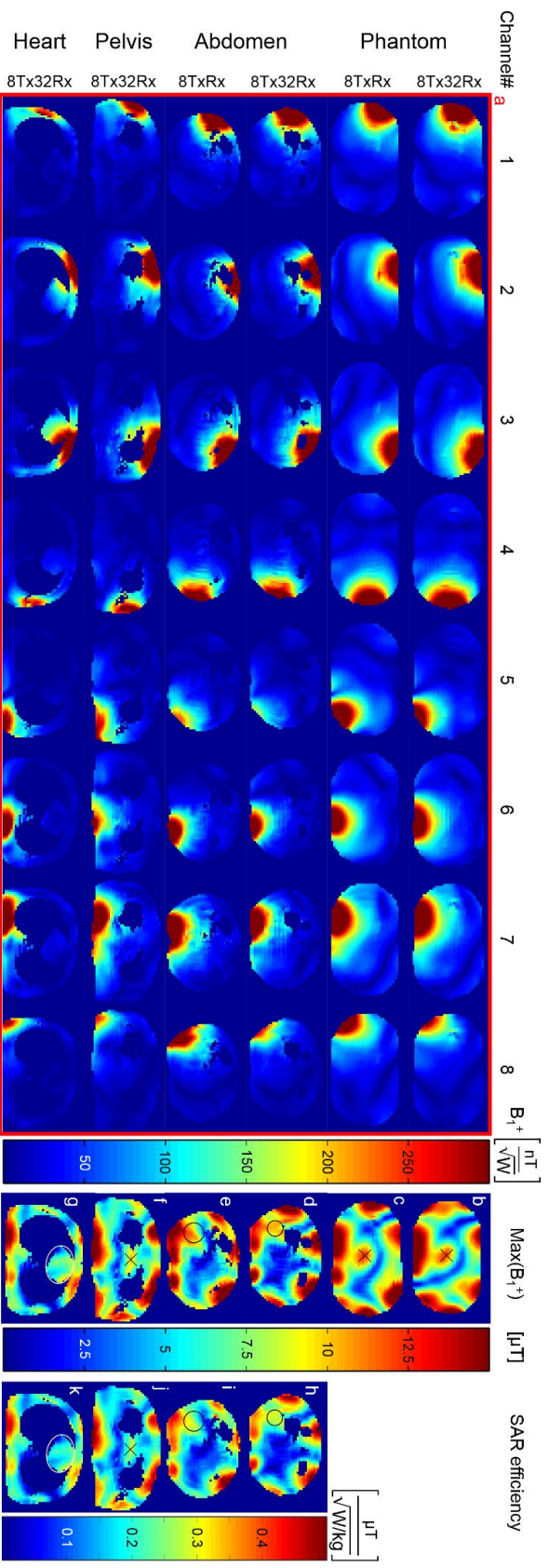


Figure 5.5: Channel-dependent B_1^+ and amplitude (a) for both arrays in a body-sized phantom and in the abdomen of Volunteer 5. The B_1^+ maps are fairly similar for both arrays. Furthermore, B_1^+ maps in the pelvis and heart for the 8Tx/32Rx array are shown for Volunteer 5. It is apparent that primarily Tx channels 2 and 3 contribute to RF excitation in the heart. Figures b-g show phase-only shims optimized for the center (b,c,f) or for a specific region of interest such as the right kidney (d,e) or the heart (g). Maximum B_1^+ and amplitudes of 12.42 μT (b) and 12.39 μT (c) in the phantom demonstrate that both arrays are comparable regarding their maximum transmit amplitude. In the center of the pelvis, a maximum amplitude of 10.59 μT is achievable with the 8Tx/32Rx array. For the right kidney, mean values of 10.04 μT (d) and 9.19 μT (e) are achieved within the specific regions of interest. In the heart (g), a mean value of 6.50 μT is achievable with a universal phase-only shim (not subject-specific). For the shims (d-g), the simulated SAR efficiency (h-k) was calculated using the maxSAR10g from the voxel model DUKE. The results are 0.22 $\mu\text{T W-0.5kg0.5}$ (mean value) for the regions of interest (h,i), 0.29 $\mu\text{T W-0.5kg0.5}$ for the center point (j) of the pelvis, and 0.19 $\mu\text{T W-0.5kg0.5}$ (mean value) for the region of interest in the heart (k).

MRI Measurements

Channel-dependent B1+ maps normalized to the applied forward power were measured in the phantom and in one volunteer (Fig 5a). For measurements with the body-sized phantom, the resulting B1+ maps of the two arrays were fairly similar, both qualitatively and quantitatively. In-vivo B1+ measurements were performed for Volunteer 5. Both arrays were compared in the abdomen. Again, the B1+ maps of both arrays showed comparable performance qualitatively and quantitatively. In addition, B1+ maps in the pelvis and heart were acquired for the 8Tx/32Rx array. In the heart, mainly channels 2 and 3 contributed to the transmit field due to their relative proximity to this organ.

Figures 5.5b-g show different phase-only shims that were achieved when the hardware limits of the system were exploited (750 W per channel). In the center of the phantom (Figures 5.5b,c), the maximum B1+ amplitude was calculated by superimposing all B1+ maps constructively. The maximum values were 12.42 μT for the 8Tx/32Rx array (Figure 5.5b) and 12.39 μT for the 8Tx/Rx array (Figure 5.5c). For the right kidney of Volunteer 5, mean values were 10.04 μT for the 8Tx/32Rx array (Figure 5.5d) and 9.19 μT for the 8Tx/Rx array (Figure 5.5e) in the corresponding regions of interest. For the pelvic region, the same approach as for the phantom measurements was performed, resulting in a maximum value of 8.26 μT in the center of the body (Figure 5.5f). In the heart, a mean value of 6.45 μT was achieved for a universal phase-only shim (not subject-specific) in the corresponding region of interest (Figure 5.5g).

For the phase-only shims (Figure 5.5d-g), the SAR efficiency was calculated for the voxel model DUKE. Maps (Figure 5.5h-k) indicate the simulated SAR efficiency for the entire transversal slice. Mean values of 0.22 $\mu\text{T W}^{-0.5}\text{kg}^{0.5}$ for the regions of interest in the abdomen (Figure 5.5h,i), 0.29 $\mu\text{T W}^{-0.5}\text{kg}^{0.5}$ for the center point (Figure 5.5j) of the pelvis, and 0.19 $\mu\text{T W}^{-0.5}\text{kg}^{0.5}$ (mean value) for the region of interest in the heart (k) could be achieved.

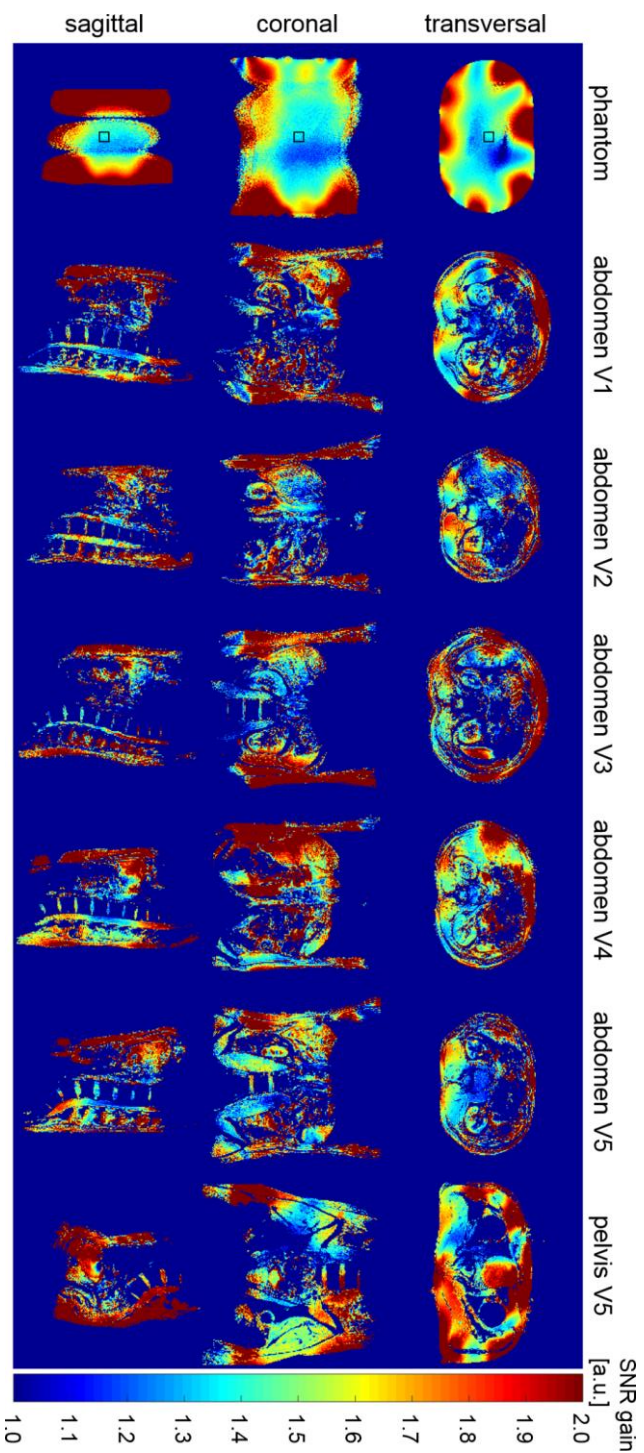


Figure 5.6: SNR gain for the 8Tx/32Rx coil when compared to the 8Tx/Rx coil in transversal, coronal, and sagittal orientation. Results from a body-sized phantom (first column) indicate SNR gain throughout the entire field of view. In the body-sized phantom, an average boost of 62% in transversal (36% in the center), 62% in coronal (33%) and 124% in sagittal (36%) orientation could be achieved. These increases are in general confirmed by investigations in the kidney regions of Volunteer 1-5 (V1-5) and in the pelvis of Volunteer 5.

The SNR gain (Figure 5.6) of the 8Tx/32Rx array when compared to the 8Tx/Rx array was calculated by dividing SNR maps acquired with all 32 channels of the 8Tx/32Rx array by SNR maps acquired with the 8Tx/Rx elements of that array only. This approach can be justified since both arrays are identical regarding the 8 Tx/Rx meander elements. Thus, the SNR gain provided by the additional 24 Rx-only loops could be directly quantified and visually assessed. In the body-sized phantom an average gain of 62% in transversal (36% in the center), 62% in coronal (33%), and 124% in sagittal (36%) orientation was achieved. The SNR gain is also visible in the abdomen (kidney region) of all Volunteers 1-5 and in the pelvis of Volunteer 5. In the kidneys, the 24 Rx-only loops provide about 40% SNR gain.

A comparison between the two arrays with respect to the mean and maximum g-factors measured in a body-sized phantom (Supporting Table 5.S1) shows that the 8Tx/32Rx array outperforms the 8Tx/Rx array in each investigated case. This is especially prominent for the sagittal and coronal orientations where the additional loops of the 8Tx/32Rx array contribute most. Yet, also in transversal orientation, right-left acceleration factors of $R(R-L) = 3$ and anterior-posterior acceleration factors of $R(A-P) = 3$ were possible with lower mean and maximum g-factors when using the 8Tx/32Rx coil compared to using the 8Tx/Rx array with $R(R-L) = 2$ and $R(A-P) = 2$. Consequently, higher acceleration capabilities can be ascribed to the 8Tx/32Rx array in general and in comparison to the 8Tx/Rx coil in particular. These findings are also bolstered by the abdominal measurements in the volunteers (Supporting Tables 5.S2-S4 and Supporting Figure 5.S2).

Figure 5.7 shows a comparison between the two arrays for different acceleration factors for Volunteer 2. In general, good image quality and homogeneity are possible with a phase-only shim in coronal orientation for both arrays. While acceleration factors of $R = 1, 2, 3$ are feasible for both arrays without impairing image quality too much, the zoomed images suggest that higher acceleration factors impede image quality especially for the 8Tx/Rx array. Here, the 8Tx/32Rx array can utilize the SNR advantage and sensitivity diversity provided by the additional 24 Rx-only loops. Comparable results can also be appreciated for Volunteers 1, 3-5 (Supporting Figures 5.S3-S6).

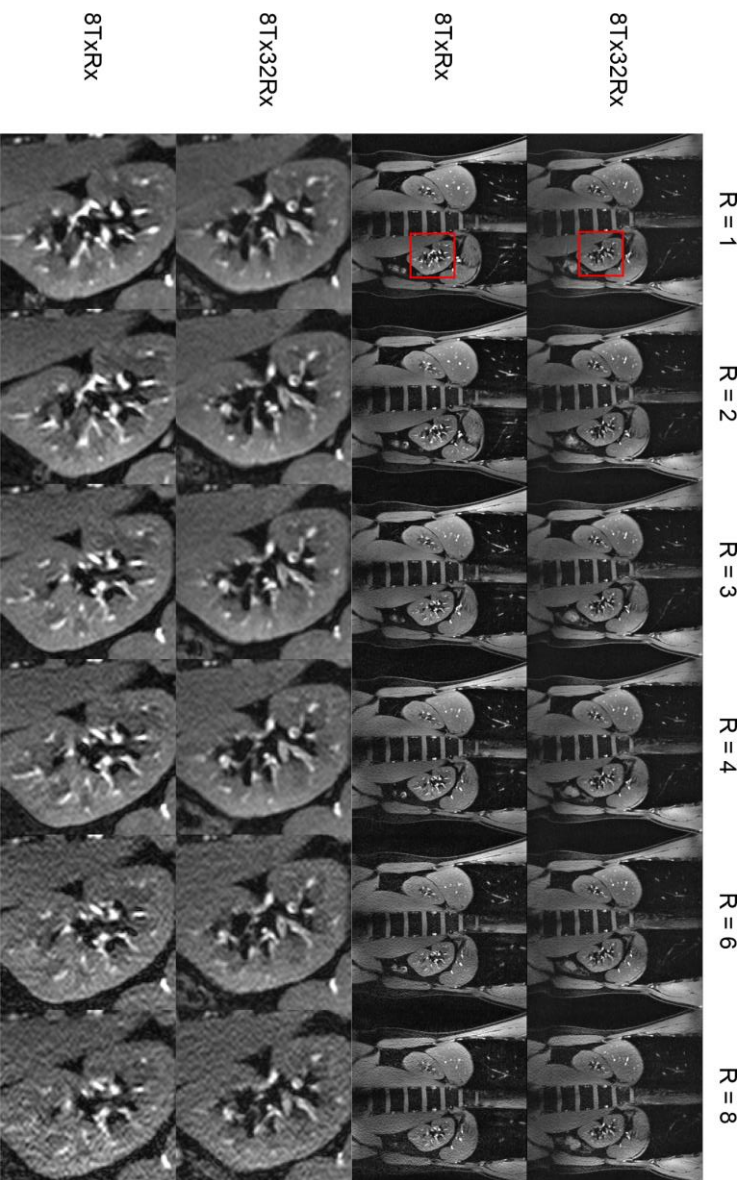


Figure 5.7: Coronal 2D FLASH gradient echo sequence in Volunteer 2 comparing images acquired with both arrays with increasing GRAPPA acceleration factors in left-right orientation. A subject specific phase-only RF shim for the left kidney was applied, which nevertheless provides good coverage of the whole abdomen. Differences are most prominent in the zoomed area (rectangle) for acceleration factors of $R = 3$ and $R = 4$. There, increased noise for the 8Tx/Rx coil is apparent in direct comparison to the 8Tx/32Rx coil. For $R = 8$, this is also visible in the entire field of view for the 8Tx/Rx coil.

Transversal acquisitions in Volunteers 1-5 using TIAMO for opposed-phase, fat-saturated, and T2*-weighted imaging are depicted in Figure 5.8. In order to compensate for the high intensity of the receive elements close to the subjects' surface, an intensity correction including a mask was applied. Excellent image quality and homogeneity were obtained with both arrays and for all sequences.

Results for cardiac imaging are depicted in Figure 5.9. During a single breath hold of about 20 s, quite homogeneous coverage and excellent blood/myocardium contrast were achieved (Figure 5.9a,b). Also, sharp delineation of the myocardium is visible. Slight signs of signal decrease due to the universal RF shim and insufficient trigger performance are visible (Figure 5.9a,c).

Coronal (Figure 5.10a) and transversal (Figure 5.10b) imaging results for pelvic imaging in the female volunteer using a 3D multi-gradient-echo sequence show high contrast and sharp delineation of the anatomical structures with a high spatial resolution of $0.68 \times 0.68 \times 0.68 \text{ mm}^3$. The sequence is optimized for the detection of metastatic lymph nodes (32). The image clearly depicts the lymph nodes and gives detailed insight in the vessel architecture. Three echoes at TE = 2.56, 6.98, 11.40 ms were reconstructed using a sum of squares reconstruction.

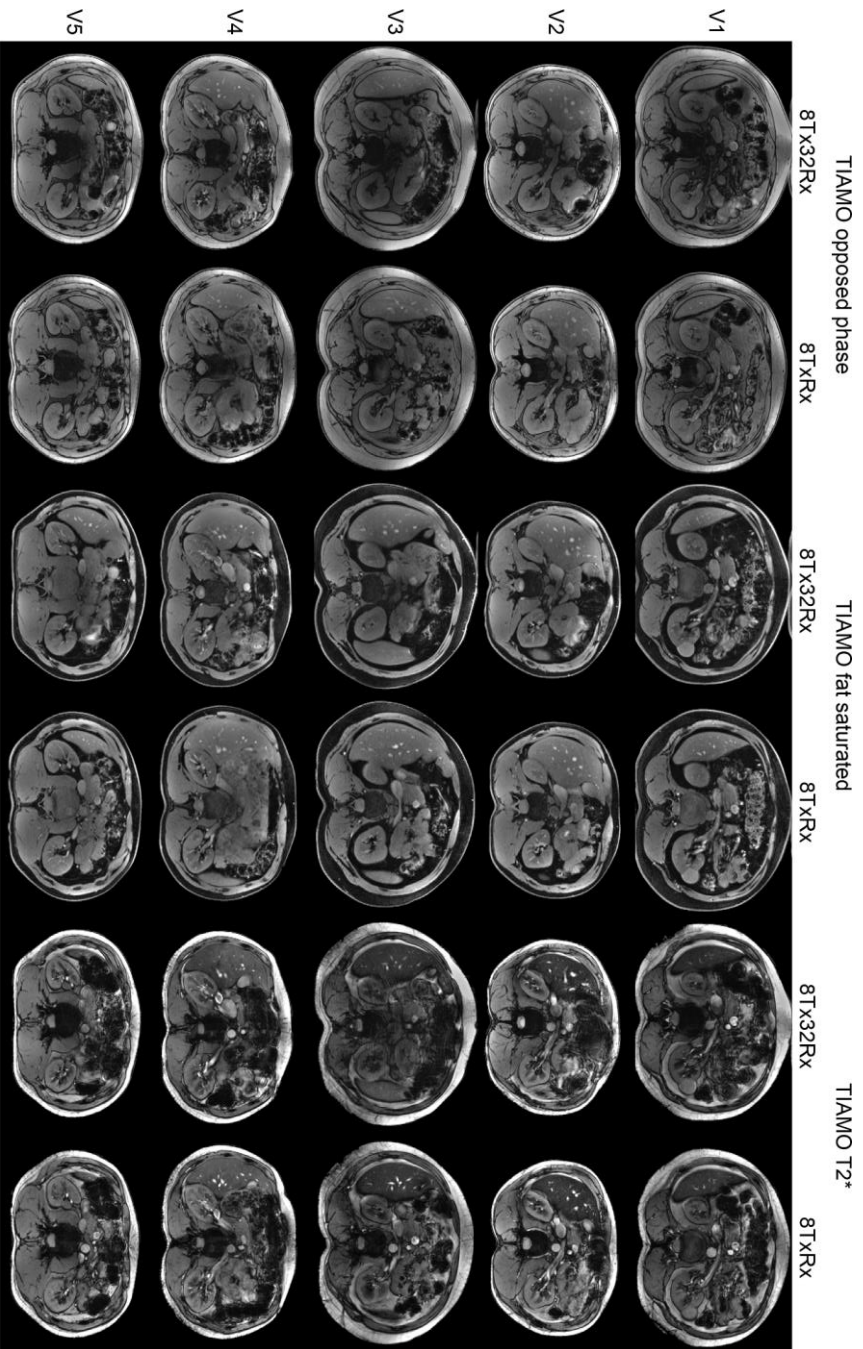


Figure 5.8: Comparison of the two arrays for transversal opposed-phase, fat-saturated, and T2*-weighted abdominal imaging in the kidney region using TIAMO for image homogenization. Overall, good image quality and homogeneity could be achieved for all Volunteers 1-5 and for both coil arrays. The first row shows images of Volunteer 1 with a known cyst in the left kidney.

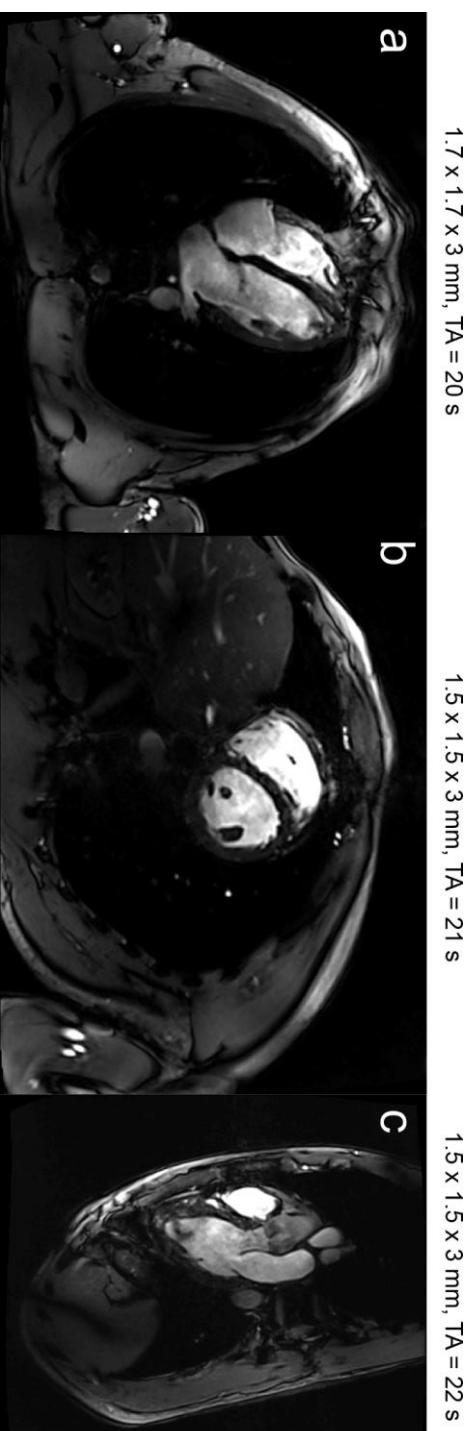


Figure 5.9: Results for cardiac MRI (a-c) using the 8Tx/32Rx array. For cardiac imaging the 4-chamber (a), short-axis (b) and LVOT (c) views are shown for Volunteer 5 using a FLASH 2D sequence (TR/TE of 41/5 ms, 992 Hz/pixel bandwidth, GRAPPA acceleration factor of $R = 2$) during a single breath hold and utilizing a universal phase-only RF shim. Homogeneous coverage of the heart and excellent blood/myocardium contrast are achieved.

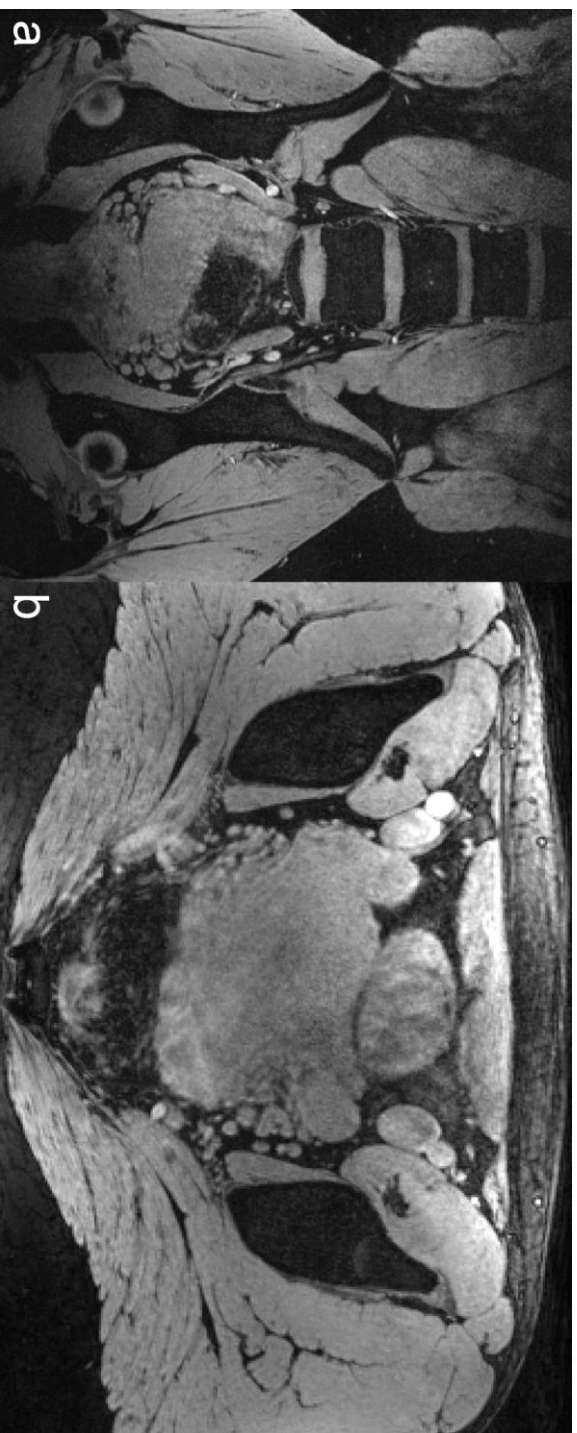


Figure 5.10: Pelvic imaging results in a female volunteer show homogeneous intensity using a 3D water-frequency-selective multi-gradient echo sequence with TIAMO at a resolution of $0.68 \times 0.68 \times 0.68 \text{ mm}^3$ within $TA = 9.40 \text{ min}$. Good visibility of the vessel architecture and presence of pelvic lymph nodes is possible at this resolution both in coronal (a) and transversal (b) orientation. The image is a sum of squares reconstruction from three echoes at $TE = 2.56, 6.98, 11.40 \text{ ms}$.

5.4 Discussion

This work demonstrates the general capability of the newly developed 8Tx/32Rx array to perform body MRI at 7T in the pelvis, abdomen, and heart. Comparisons to the 8Tx/Rx array as a standard of reference indicate the SNR gain of the additional 24 Rx-only loops and the distinct acceleration advantages that come with it. It is shown that it is possible to add three receive loops along the length of a meander element without compromising its performance, thereby making better use of the space on the coil surface near the body compared to what has been published before.

Simulated and measured E- and H-fields for the dosimetric measurement setup using a body-sized elliptical phantom allowed the simulation model of the 8Tx/32Rx array and the simulation procedure to be validated both qualitatively and quantitatively. Low intrinsic coupling between meander elements and loops, sufficient active detuning and comparability between the 8TxRx and the 8Tx32Rx coil concerning B1+ maps suggest that neglecting the loops in the simulation can be justified. Simulations of the new array with heterogeneous body models in the specific body region can then be used to evaluate the SAR and to ensure that the safety limits are not exceeded. Consequently, safe use of the array for in vivo measurements is ensured.

The SNR gain due to the 24 additional Rx-only loops of the 8Tx/32Rx array was strong (33% even in the subject's center). This was especially convincing in the phantom measurements in transversal, coronal, and sagittal sections, where throughout the entire cross-section SNR gain could be appreciated. The results indicate that the SNR gain is decreased towards the center, which can be explained by the limited penetration depth of elements at 300 MHz in general, and loops in this particular case. SNR gain maps in the volunteers confirmed these findings; however, they are influenced by the individual anatomy of each volunteer. It should be noted that the circularly polarized mode was used to acquire the presented SNR maps, leading to low intensity areas due to signal drop out since one shim cannot

cover the entire field of view with adequate uniformity. In these regions, no reliable SNR gain can be quantified. Utilization of the TIAMO technique could be a possible solution for this issue.

While the individual RF coil elements, in general, were well decoupled on the transmit side, the S-parameters indicated enhanced coupling between elements in the posterior portion of the array, which can be attributed to the array geometry and the loading conditions of the corresponding coil elements. All elements in the posterior (bottom) portion are located closer to one another as compared to the anterior (top) elements, and they are aligned to the flat cover of the bottom housing, which increases the distance of the subject to the RF building blocks on both lateral sides. Consequently, for these RF elements coupling is increased due to the lower amount of intervening body tissue.

Measurements of the preamplifier decoupling and the detuning were both performed under loaded conditions. This might influence the results, since the two conductors of the double pick-up loop also receive signals from the sample. Furthermore, the Q of the coil is spoiled by the heavy loading. The presented coil shows maximum coupling values of -22.4 dB for the transmit elements which is below the values reported in references (24,26). Also the intrinsic coupling between the meander elements and loops in the same building block is below -20.5 dB (without any preamplifier decoupling which comes on top). Higher values were reported in references (24,26). This can explain why we can't observe an impact of the loops on transmit efficiency as mentioned before (26).

The comparison between the presented B1+ maps of the 8Tx/Rx and the 8Tx/32Rx arrays confirm the assumption that both arrays are similar from the transmit point of view. In the phantom center, similar maximum values of 12.42 μ T for the 8Tx/32Rx array and 12.39 μ T for the 8Tx/Rx array were achieved. Differences in the right kidney of Volunteer 5 can be attributed to slightly differing shimming regions and different convergence of the shimming algorithm used for calculation. In the pelvis, the maximum value of 8.26 μ T is lower compared to what

is achievable in the phantom, which is most likely related to the body geometry. The 8Tx/32Rx array allows for quite homogeneous B1+ coverage of the heart.

Accelerated images using a phase-only shim for one kidney demonstrated good imaging capabilities for both arrays. While the examinations of SNR gain indicate that in general an SNR gain can be confirmed for the 8Tx/32Rx array, this increase is not directly visible for acceleration factors of $R = 1, 2, 3$ since SNR is sufficient for both arrays. Only at higher acceleration factors in coronal orientation does the 8Tx/32Rx array clearly outperform the 8Tx/Rx array due to the g-factor differences. It should be noted, however, that currently one-dimensional acceleration factors of higher than $R = 6$ are not frequently used, especially for body imaging at 7T. As the g-factors show, additional acceleration in head-feet direction would definitely favor the 8Tx/32Rx array due to the 3 additional loops per building block.

Transversal abdominal images in the kidney region using the TIAMO technique demonstrate good image quality for both arrays and for all five volunteers. Even deep-lying organs are depicted with fine detail, especially in the case of comparatively small body sizes, while for larger subjects reduced image intensity in the center was observed. The reduced intensity in the center is a consequence of a general challenge at ultra-high field, i.e. limited RF signal penetration depth. The improved SNR of the 8Tx/32Rx array does not always translate into a better image quality. For V1 and V3 the 8Tx/Rx array shows slightly better performance than the 8Tx/32Rx array for TIAMO opposed phase images.

Cardiac imaging yielded promising results. A single phase-only RF shim provided sufficient coverage of the entire heart during breath hold, providing good homogeneity and excellent blood/myocardium contrast. The image quality was partly hampered by insufficient cardiac trigger performance. Furthermore, a universal RF shim was used that is not subject-specific and can lead to inhomogeneous areas in the images. Consequently, for cardiac imaging with the 8Tx/32Rx RF array, there is room for improvement in future examinations by using a subject-specific shim and alternative or additional triggering methods.

As the 8Tx/Rx body array, which served as the standard of reference in this work, has already been used in a broad variety of clinical 7T MRI investigations (32–40), the improved performance of the new combined array holds great promise for 7T UHF body MRI, increasing either the spatial resolution of these examinations or speeding up the acquisition time through use of higher parallel imaging factors. Imaging results in the pelvis of a female volunteer showed high homogeneity at a very high resolution of $0.68 \times 0.68 \times 0.68 \text{ mm}^3$, which was achieved within less than 10 min acquisition time. Here an acceleration factor of 6 was used to play out the good acceleration capabilities. These results encourage the application of the newly developed 8Tx/32Rx array in high-resolution applications, such as the detection of metastatic lymph nodes with 7T UHF MRI (32), to further improve the diagnostic power.

5.5 Conclusions

A combination of micro striplines with meanders and loops in a combined 8Tx/32Rx RF array for use in UHF body MRI is technically feasible and safe. Coupling between the two different RF element types was low, and safe use of the array in volunteer examinations could be demonstrated using dosimetric E- and H-field measurements. When compared to an existing 8Tx/Rx array, the new 8Tx/32Rx array offers SNR gain and higher parallel imaging acceleration capabilities. Volunteer images of the abdomen, heart and pelvis confirm the capability of the 8Tx/32Rx array to perform 7T UHF body MR imaging with excellent image quality and homogeneity, indicating opportunities for a wide range of applications in 7T body imaging using the presented RF array.

Acknowledgements

The authors wish to thank Lena C. Schäfer, Sarah Handtke, Jonathan Weine (Erwin L. Hahn Institute for MR imaging, Essen, Germany), and Andreas K. Bitz (University of Applied Sciences Aachen, Germany) for their support. The research leading to these results has received funding from the European Research Council under the European Union's Seventh Framework Programme (FP/2007-2013) / ERC Grant Agreement n. 291903 MRexcite.

References

1. Roemer PB, Edelstein WA, Hayes CE, Souza SP, Mueller OM. The NMR phased array. *Magn Reson Med* 1990;16(2):192–225.
2. Griswold MA, Jakob PM, Heidemann RM, Nittka M, Jellus V, Wang J, Kiefer B, Haase A. Generalized autocalibrating partially parallel acquisitions (GRAPPA). *Magn Reson Med* 2002;47(6):1202–10.
3. Hoult DI, Phil D. Sensitivity and Power Deposition in a High-Field Imaging Experiment. *J Magn Reson Imaging* 2000;67:46–67.
4. Van de Moortele PF, Akgun C, Adriany G, Moeller S, Ritter J, Collins CM, Smith MB, Vaughan JT, Ugurbil K. B1 Destructive Interferences and Spatial Phase Patterns at 7 T with a Head Transceiver Array Coil. 2005;1518:1503–18.
5. Collins CM, Liu W, Swift BJ, Smith MB. Combination of optimized transmit arrays and some receive array reconstruction methods can yield homogeneous images at very high frequencies. *Magn Reson Med* 2005;54(6):1327–32.
6. Mao W, Smith MB, Collins CM. Exploring the limits of RF shimming for high-field MRI of the human head. *Magn Reson Med* 2006;56(4):918–22.
7. Katscher U, Börnert P, Leussler C, van den Brink JS. Transmit SENSE. *Magn Reson Med* 2003;49(1):144–50.
8. Grissom W, Yip C, Zhang Z, Stenger VA, Fessler JA, Noll DC. Spatial domain method for the design of RF pulses in multicoil parallel excitation. *Magn*

Reson Med 2006;56(3):620–9.

9. Orzada S, Maderwald S, Poser BA, Bitz AK, Quick HH, Ladd ME. RF excitation using time interleaved acquisition of modes (TIAMO) to address B1 inhomogeneity in high-field MRI. *Magn Reson Med* 2010;64(2):327–33.
10. Orzada S, Maderwald S, Poser BA, Johst S, Kannengiesser S, Ladd ME, Bitz AK. Time-interleaved acquisition of modes: an analysis of SAR and image contrast implications. *Magn Reson Med* 2012;67(4):1033–41.
11. Brunner DO, De Zanche N, Froehlich J, Baumann D, Pruessmann KP. A symmetrically fed microstrip coil array for 7T. *Proc Intl Soc MRM* 15 2007. p. 448.
12. Metzger GJ, Snyder C, Akgun C, Vaughan T, Ugurbil K, Van de Moortele P-F. Local B1+ shimming for prostate imaging with transceiver arrays at 7T based on subject-dependent transmit phase measurements. *Magn Reson Med* 2008;59(2):396–409.
13. Snyder CJ, DelaBarre L, Metzger GJ, van de Moortele P-F, Akgun C, Ugurbil K, Vaughan JT. Initial results of cardiac imaging at 7 Tesla. *Magn Reson Med* 2009;61(3):517–24.
14. Vaughan JT, Snyder CJ, DelaBarre LJ, Bolan PJ, Tian J, Bolinger L, Adriany G, Andersen P, Strupp J, Ugurbil K. Whole-body imaging at 7T: preliminary results. *Magn Reson Med* 2009;61(1):244–8.
15. Avdievich NI. Transceiver-Phased Arrays for Human Brain Studies at 7 T. *Appl Magn Reson* 2013;41:483–506.

16. Gräßl A, Winter L, Thalhammer C, Renz W, Kellman P, Martin C, von Knobelsdorff-Brenkenhoff F, Tkachenko V, Schulz-Menger J, Niendorf T. Design, evaluation and application of an eight channel transmit/receive coil array for cardiac MRI at 7.0 T. *Eur J Radiol Elsevier Ireland Ltd*; 2013;82(5):752–9.
17. Kraff O, Bitz AK, Kruszona S, Orzada S, Schaefer LC, Theysohn JM, Maderwald S, Ladd ME, Quick HH. An eight-channel phased array RF coil for spine MR imaging at 7 T. *Invest Radiol* 2009;44(11):734–40.
18. Raaijmakers AJE, Ipek O, Klomp DWJ, Possanzini C, Harvey PR, Lagendijk JJW, van den Berg CAT. Design of a radiative surface coil array element at 7 T: the single-side adapted dipole antenna. *Magn Reson Med* 2011;66(5):1488–97.
19. Orzada S, Bahr A, Bolz T. A novel 7 T microstrip element using meanders to enhance decoupling. *Proc Intl Soc MRM* 16 2008. p. 2979.
20. Orzada S, Bitz AK, Schäfer LC, Ladd SC, Ladd ME, Maderwald S. Open design eight-channel transmit/receive coil for high-resolution and real-time ankle imaging at 7 T. *Med Phys* 2011;38(3):1162–7.
21. Rietsch SHG, Quick HH, Orzada S. Impact of different meander sizes on the RF transmit performance and coupling of microstrip line elements at 7 T. *Med Phys* 2015;42(8):4542–52.
22. Orzada S, Quick HH, Ladd ME, Bahr A, Bolz T, Yazdanbakhsh P, Solbach K, Bitz AK. A flexible 8-channel transmit/receive body coil for 7 T human imaging. *Proc Intl Soc MRM* 17 2009. p. 2999.

23. Graessl A, Renz W, Hezel F, Dieringer M a, Winter L, Oezerdem C, Rieger J, Kellman P, Santoro D, Lindel TD, et al. Modular 32-channel transceiver coil array for cardiac MRI at 7.0T. *Magn Reson Med* 2014;72(1):276–90.
24. Ertürk MA, Raaijmakers AJE, Adriany G, Uğurbil K, Metzger GJ. A 16-channel combined loop-dipole transceiver array for 7 Tesla body MRI. *Magn Reson Med* 2017;77:884–94.
25. Raaijmakers AJE, Italiaander M, Voogt IJ, Luijten PR, Hoogduin JM, Klomp DWJ, Van Den Berg CAT. The fractionated dipole antenna: A new antenna for body imaging at 7 Tesla. *Magn Reson Med* 2016;75(3):1366–74.
26. Voogt IJ, Klomp DWJ, Hoogduin H, Luttje MP, Luijten PR, van den Berg CAT, Raaijmakers AJE. Combined 8-channel transceiver fractionated dipole antenna array with a 16-channel loop coil receive array for body imaging at 7T. *Proc Intl Soc MRM* 23 2015. p. 631.
27. Bitz AK, Kraff O, Orzada S, Maderwald S, Brote I, Johst S, Ladd ME. Assessment of RF Safety of Transmit Coils at 7 Tesla by Experimental and Numerical Procedures. *Proc Intl Soc MRM* 19 2011. p. 490.
28. Hoffmann J, Henning A, Giapitzakis I a, Scheffler K, Shajan G, Pohmann R, Avdievich NI. Safety testing and operational procedures for self-developed radiofrequency coils. *NMR Biomed* 2015;29(9):1131–44.
29. Christ A, Kainz W, Hahn EG, Honegger K, Zefferer M, Neufeld E, Rascher W, Janka R, Bautz W, Chen J, et al. The Virtual Family--development of surface-based anatomical models of two adults and two children for dosimetric simulations. *Phys Med Biol* 2010;55(2):N23–38.

30. Bitz AK, Brote I, Orzada S, Kraff O, Maderwald S, Quick HH, Yazdanbakhsh P, Solbach K, Bahr A, Bolz T, et al. An 8-channel add-on RF shimming system for whole-body 7 Tesla MRI including real-time SAR monitoring. *Proc Intl Soc MRM* 17 2009. p. 4767.
31. Brunheim S, Gratz M, Johst S, Bitz AK, Fiedler TM, Ladd ME, Quick HH, Orzada S. Fast and Accurate Multi-Channel B1+ Mapping Based on the TIAMO Technique for 7T UHF Body MRI. *Magn Reson Med* 2017;(epub ahead of print).
32. Philips BWJ, Fortuin AS, Orzada S, Scheenen TWJ, Maas MC. High resolution MR imaging of pelvic lymph nodes at 7 Tesla. *Magn Reson Med* 2017;78(3):1020–8.
33. Lazik-Palm A, Kraff O, Johst S, Quick HH, Ladd ME, Geis C, Körsmeier K, Landgraeber S, Theysohn JM. Morphological and Quantitative 7 T MRI of Hip Cartilage Transplants in Comparison to 3 T—Initial Experiences. *Invest Radiol* 2016;51(9):552–9.
34. Lazik-Palm A, Kraff O, Geis C, Johst S, Goebel J, Ladd ME, Quick HH, Theysohn JM. Morphological imaging and T2 and T2* mapping of hip cartilage at 7 Tesla MRI under the influence of intravenous gadolinium. *Eur Radiol European Radiology*; 2016;26(11):3923–31.
35. Hahnemann ML, Kraff O, Orzada S, Umutlu L, Kinner S, Ladd ME, Quick HH, Lauenstein TC. T1-Weighted Contrast-Enhanced Magnetic Resonance Imaging of the Small Bowel. *Invest Radiol* 2015;50(8):539–47.
36. Hahnemann ML, Kraff O, Maderwald S, Johst S, Orzada S, Umutlu L, Ladd

- ME, Quick HH, Lauenstein TC. Non-enhanced magnetic resonance imaging of the small bowel at 7 Tesla in comparison to 1.5 Tesla: First steps towards clinical application. *Magn Reson Imaging Elsevier Inc.*; 2016;34(5):668–73.
37. Maderwald S, Orzada S, Schäfer LC, Bitz AK, Brote I, Kraff O, Theysohn JM, Ladd ME, Ladd SC, Quick HH. 7T Human in vivo Cardiac Imaging with an 8-Channel Transmit/Receive Array. *Proc Intl Soc MRM* 17 2009. p. 822.
 38. Lagemaat MW, Breukels V, Vos EK, Kerr AB, van Uden MJ, Orzada S, Bitz AK, Maas MC, Scheenen TWJ. ¹H MR spectroscopic imaging of the prostate at 7T using spectral-spatial pulses. *Magn Reson Med* 2015;945(2016):933–45.
 39. Theysohn JM, Kraff O, Orzada S, Theysohn N, Classen T, Landgraeber S, Ladd ME, Lauenstein TC. Bilateral hip imaging at 7 Tesla using a multi-channel transmit technology: initial results presenting anatomical detail in healthy volunteers and pathological changes in patients with avascular necrosis of the femoral head. *Skeletal Radiol* 2013;42(11):1555–63.
 40. Umutlu L, Maderwald S, Kinner S, Kraff O, Bitz AK, Orzada S, Johst S, Wrede K, Forsting M, Ladd ME, et al. First-pass contrast-enhanced renal MRA at 7 Tesla: initial results. *Eur Radiol* 2013;23(4):1059–66.

Supporting Figures

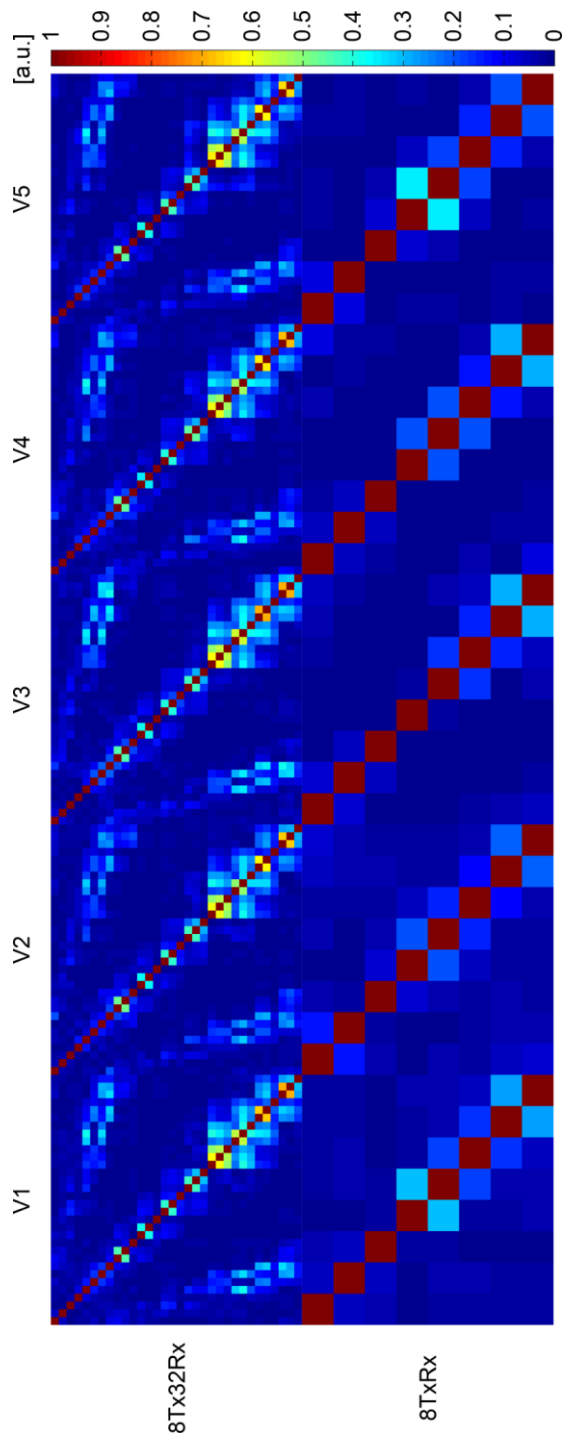


Figure 5S1: Noise correlation coefficient in the abdomen of Volunteers 1-5 using the 8Tx/32Rx coil compared to the 8Tx/Rx coil. The measurement results are in general comparable for all subjects. Nevertheless, some variations are visible, for example between Tx channel 4 and 5 using the 8Tx/Rx coil.

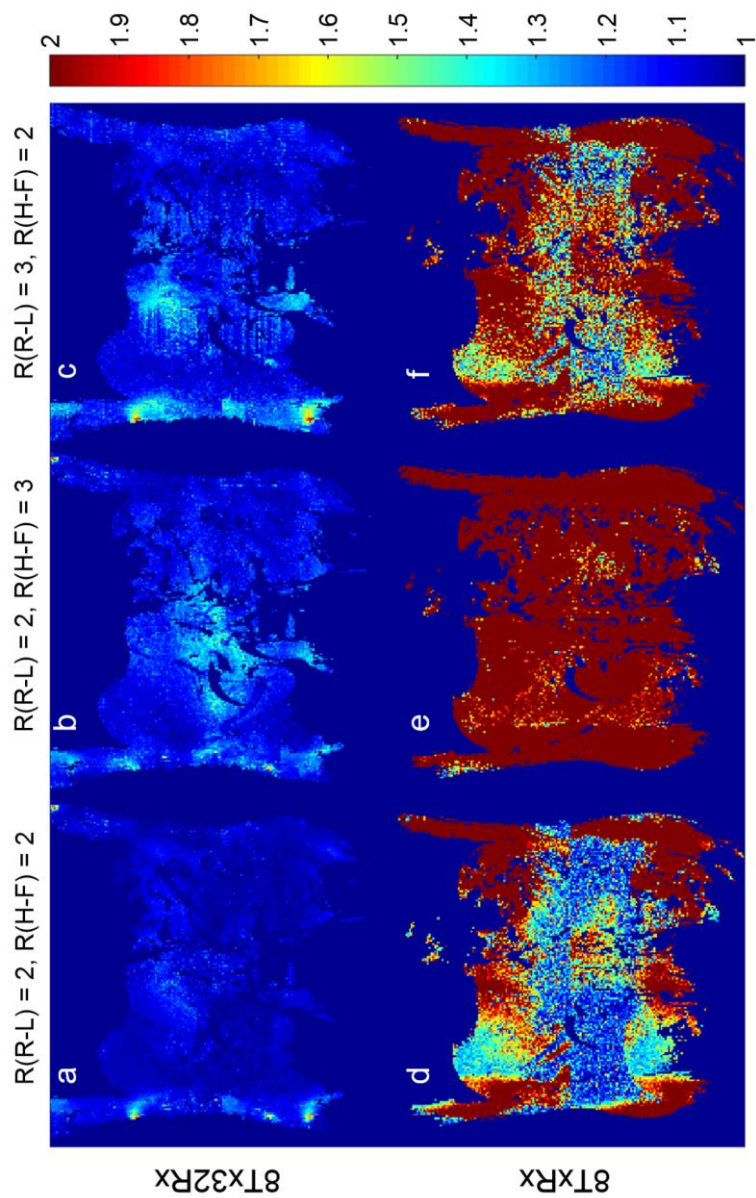


Figure 5S2: Coronal g-factor maps for the 8Tx/32Rx in comparison to the 8Tx/Rx coil. As can be seen, the presented acceleration factors in both directions are still applicable for the 8Tx/32Rx coil while high g-factor values can be observed for the 8Tx/Rx coil. The scale is cropped at the maximum value.

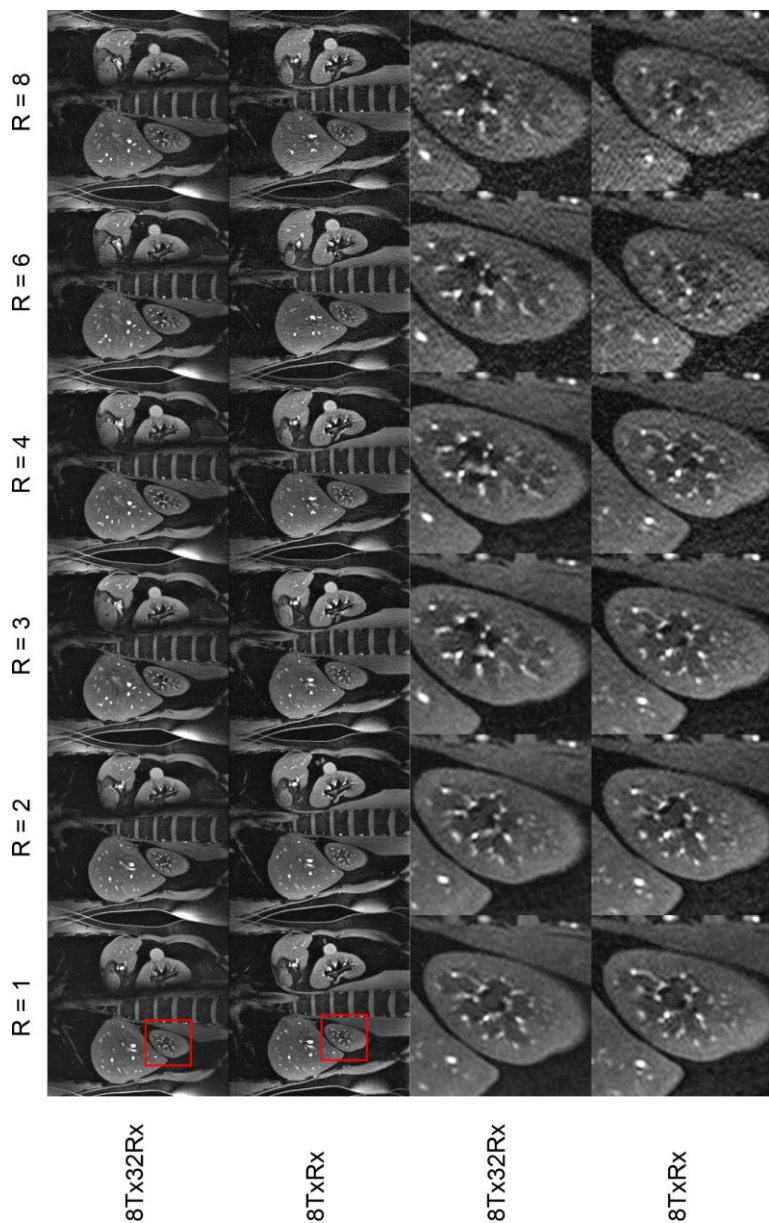


Figure 5S3: Coronal 2D FLASH gradient echo sequence in Volunteer 1 comparing images acquired with both arrays and different acceleration factors. A subject-specific phase-only RF shim for the right kidney was applied. In this case the shim algorithm converged to a phase setting which leads to a signal void in the left kidney. The signal void is oriented parallel to the spine.

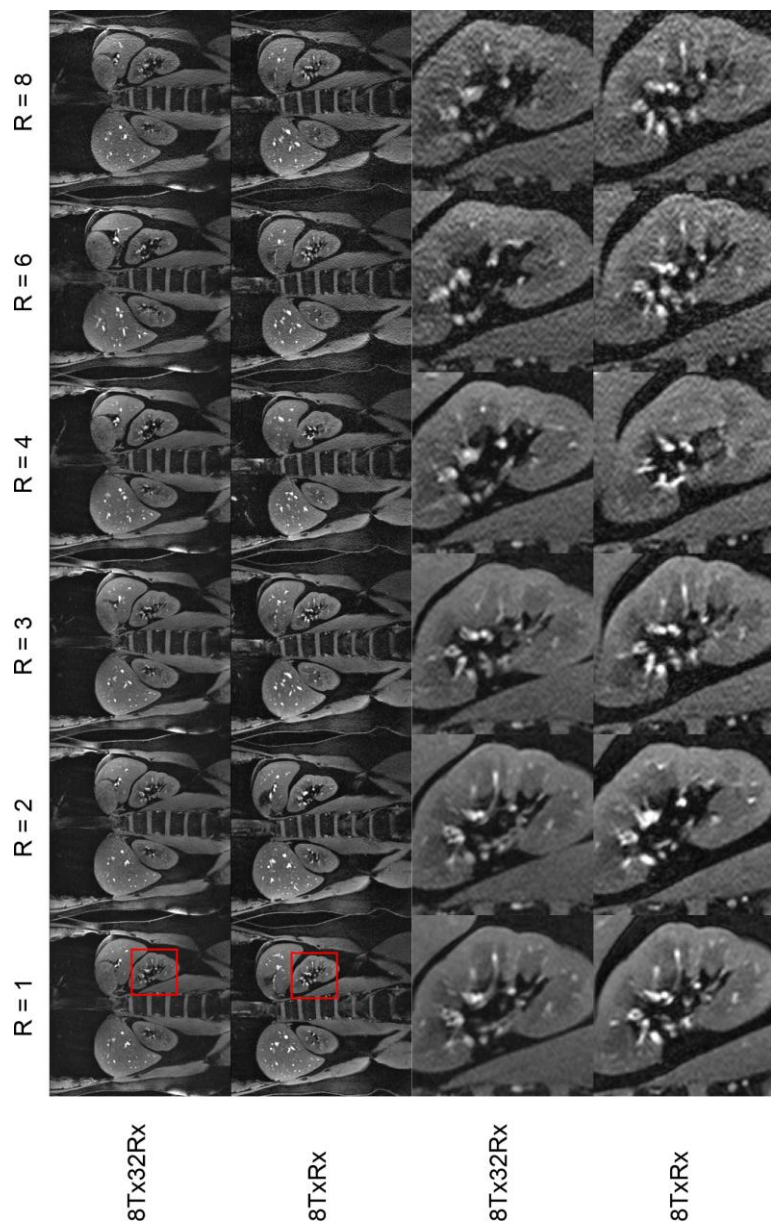


Figure 5S4: Coronal 2D FLASH gradient echo sequence in Volunteer 3 comparing images acquired with both arrays and different acceleration factors. A subject-specific phase-only RF shim for the left kidney was applied. Good homogeneity could be achieved with this phase-only shim in the coronal orientation.

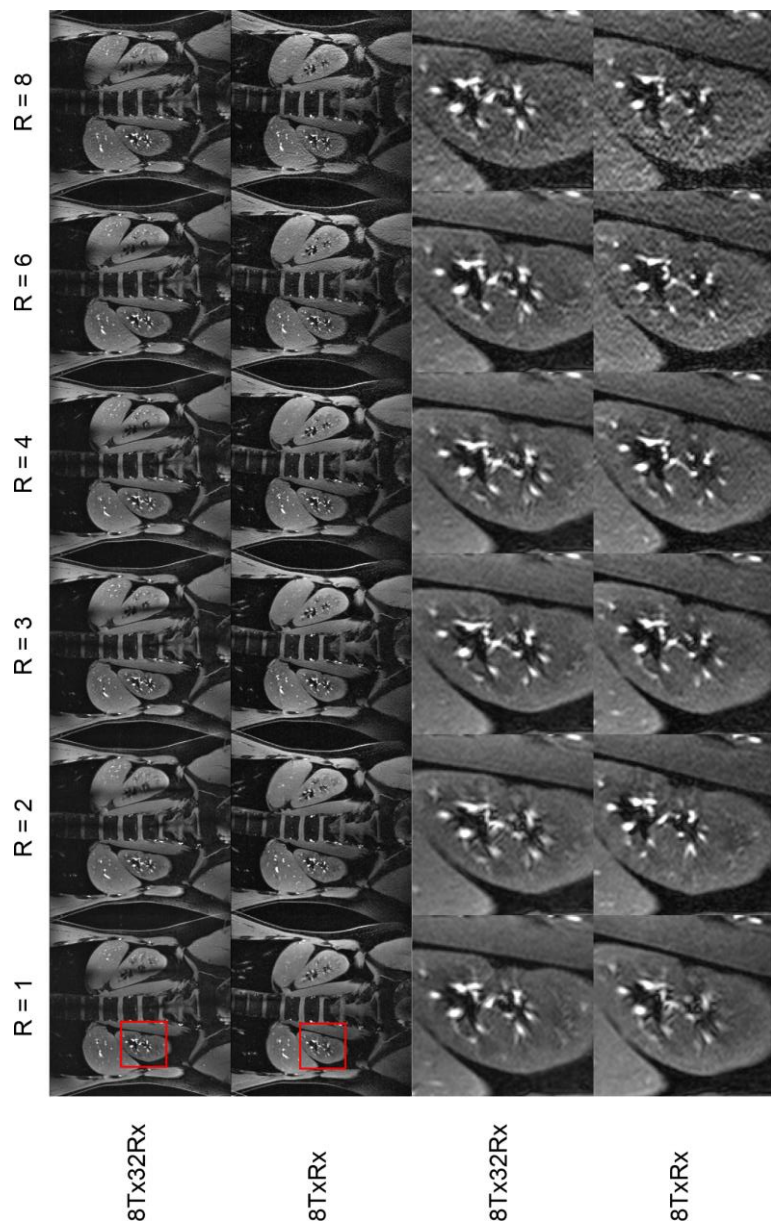


Figure 5S5: Coronal 2D FLASH gradient echo sequence in Volunteer 4 comparing images acquired with both arrays and different acceleration factors. A subject-specific phase-only RF shim for the right kidney was applied.

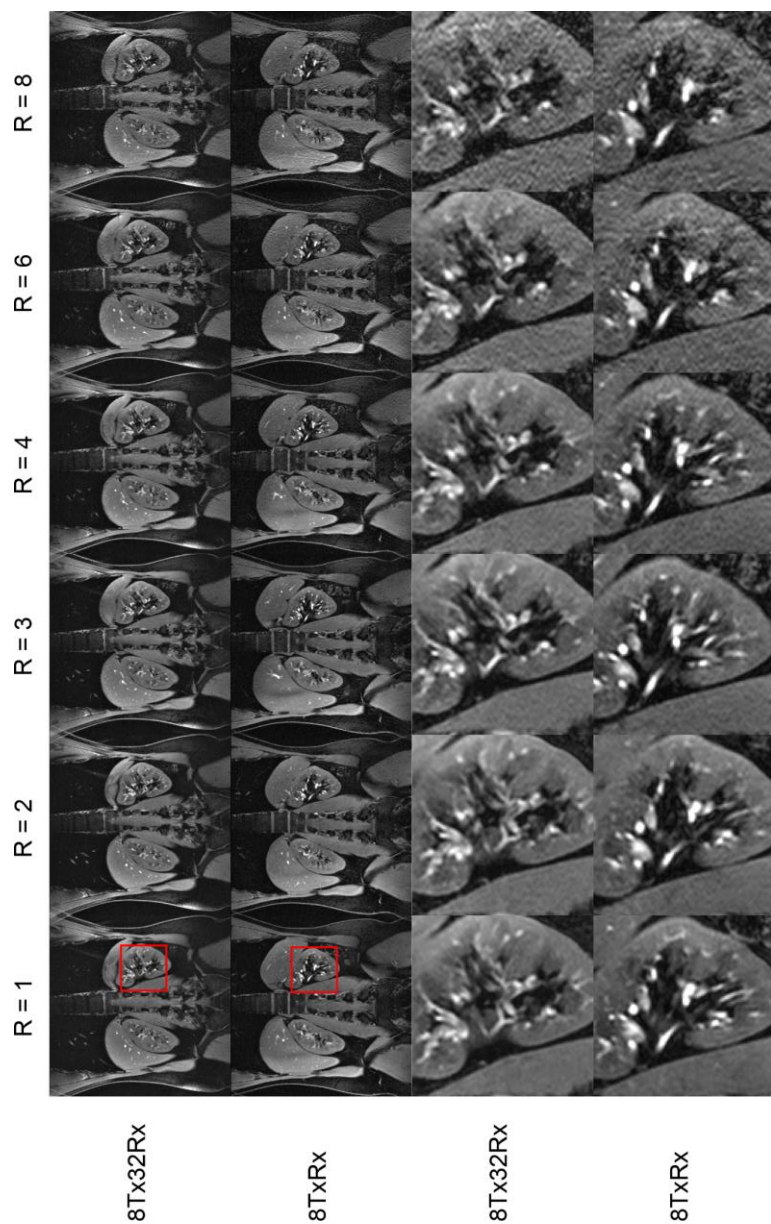


Figure 5S6: Coronal 2D FLASH gradient echo sequence in Volunteer 5 comparing images acquired with both arrays and different acceleration factors. A subject-specific phase-only RF shim for the left kidney was played out. Good homogeneity can be achieved with this phase-only shim in the coronal orientation. The difference between the arrays can be appreciated in the zoomed images, e.g. for $R = 6$.

Supporting Tables

		8Tx/32Rx			8Tx/Rx		
tra		R(R-L) = 1	R(R-L) = 2	R(R-L) = 3	R(R-L) = 1	R(R-L) = 2	R(R-L) = 3
	R(A-P) = 2	1.02/1.22	1.04/1.26	1.07/1.47	1.06/2.23	1.20/3.95	1.53/7.35
	R(A-P) = 3	1.04/1.30	1.07/1.40	1.13/1.55	1.14/2.54	1.48/9.43	
	R(A-P) = 4	1.11/1.55		1.27/2.07	1.34/4.63		
cor		R(H-F) = 1	R(H-F) = 2	R(H-F) = 3	R(H-F) = 1	R(H-F) = 2	R(H-F) = 3
	R(R-L) = 2	1.01/1.18	1.05/1.24	1.11/1.91	1.03/2.19	1.87/18.87	4.02/83.33
	R(R-L) = 3	1.03/1.37	1.10/1.61	1.18/2.02	1.12/2.57	2.45/33.33	
	R(R-L) = 4	1.09/1.61		1.33/2.47	1.25/3.31		
sag		R(H-F) = 1	R(H-F) = 2	R(H-F) = 3	R(H-F) = 1	R(H-F) = 2	R(H-F) = 3
	R(A-P) = 2	1.02/1.24	1.06/1.28	1.14/1.43	1.07/1.92	2.03/18.52	5.28/90.91
	R(A-P) = 3	1.03/1.21	1.09/1.39	1.18/1.71	1.13/2.19	2.59/43.48	
	R(A-P) = 4	1.14/1.64		1.39/2.49	1.35/3.73		

Supporting Table 5S1: Mean and maximum (mean/max) g-factors measured in a body-sized phantom for the 8Tx/32Rx and the 8Tx/Rx array. The additional loops of the 8Tx/32Rx array enable higher acceleration factors due to the reduced g-factors. For example, the mean and maximum g-factors are lower for the 8Tx/32Rx array using right-left acceleration with factor $R(R-L) = 3$ and anterior-posterior acceleration with $R(A-P) = 3$ compared to using the 8Tx/Rx array with $R(R-L) = 2$ and $R(A-P) = 2$ in transversal orientation. In coronal and sagittal orientation, the advantage is even more prominent since three loops contribute in head-feet (H-F) direction.

		8Tx/32Rx			8Tx/Rx		
tra		R(R-L) = 1	R(R-L) = 2	R(R-L) = 3	R(R-L) = 1	R(R-L) = 2	R(R-L) = 3
	R(A-P) = 2	1.02/1.35	1.04/1.39	1.09/1.54	1.06/2.21	1.19/3.09	1.48/6.54
	R(A-P) = 3	1.06/1.72	1.10/1.80	1.18/1.92	1.18/3.22	1.54/11.63	
	R(A-P) = 4	1.15/2.07		1.35/2.60	1.41/4.69		
cor		R(H-F) = 1	R(H-F) = 2	R(H-F) = 3	R(H-F) = 1	R(H-F) = 2	R(H-F) = 3
	R(R-L) = 2	1.01/1.79	1.07/1.85	1.13/1.95	1.02/2.21	1.66/7.75	3.33/24.39
	R(R-L) = 3	1.05/1.49	1.13/2.03	1.22/1.81	1.09/2.18	2.12/16.39	
	R(R-L) = 4	1.15/2.26		1.40/2.62	1.22/3.51		
sag		R(H-F) = 1	R(H-F) = 2	R(H-F) = 3	R(H-F) = 1	R(H-F) = 2	R(H-F) = 3
	R(A-P) = 2	1.01/1.23	1.08/1.46	1.17/1.86	1.04/1.86	1.79/7.30	3.41/27.03
	R(A-P) = 3	1.05/1.50	1.13/1.73	1.26/2.02	1.19/3.19	2.49/23.81	
	R(A-P) = 4	1.14/1.70		1.44/2.57	1.51/4.93		

Supporting Table 5S2: Mean and maximum g-factors measured in Volunteer 1 for the 8Tx/32Rx array and the 8Tx/Rx array.

		8Tx/32Rx			8Tx/Rx		
tra		R(R-L) = 1	R(R-L) = 2	R(R-L) = 3	R(R-L) = 1	R(R-L) = 2	R(R-L) = 3
	R(A-P) = 2	1.02 ± 0.01	1.05 ± 0.00	1.09 ± 0.00	1.06 ± 0.01	1.21 ± 0.03	1.52 ± 0.05
	R(A-P) = 3	1.06 ± 0.02	1.10 ± 0.02	1.18 ± 0.02	1.17 ± 0.03	1.55 ± 0.02	
	R(A-P) = 4	1.15 ± 0.03		1.34 ± 0.04	1.37 ± 0.07		
cor		R(H-F) = 1	R(H-F) = 2	R(H-F) = 3	R(H-F) = 1	R(H-F) = 2	R(H-F) = 3
	R(R-L) = 2	1.01 ± 0.00	1.06 ± 0.01	1.13 ± 0.01	1.02 ± 0.01	1.54 ± 0.14	2.98 ± 0.55
	R(R-L) = 3	1.05 ± 0.01	1.12 ± 0.01	1.21 ± 0.02	1.10 ± 0.02	1.98 ± 0.18	
	R(R-L) = 4	1.13 ± 0.03		1.37 ± 0.04	1.24 ± 0.03		
sag		R(H-F) = 1	R(H-F) = 2	R(H-F) = 3	R(H-F) = 1	R(H-F) = 2	R(H-F) = 3
	R(A-P) = 2	1.02 ± 0.01	1.07 ± 0.01	1.17 ± 0.01	1.05 ± 0.01	1.67 ± 0.14	2.99 ± 0.54
	R(A-P) = 3	1.05 ± 0.01	1.13 ± 0.00	1.25 ± 0.02	1.16 ± 0.02	2.24 ± 0.24	
	R(A-P) = 4	1.13 ± 0.01		1.41 ± 0.03	1.38 ± 0.09		

Supporting Table 5S3: Mean g-factors of all 5 volunteers averaged with standard deviation for the 8Tx/32Rx and the 8Tx/Rx array.

		8Tx/32Rx			8Tx/Rx		
tra		R(R-L) = 1	R(R-L) = 2	R(R-L) = 3	R(R-L) = 1	R(R-L) = 2	R(R-L) = 3
	R(A-P) = 2	1.38 ± 0.13	1.42 ± 0.12	1.57 ± 0.11	2.42 ± 0.46	3.40 ± 0.46	7.53 ± 1.89
	R(A-P) = 3	1.92 ± 0.47	1.99 ± 0.45	2.15 ± 0.54	3.38 ± 0.77	9.47 ± 1.76	
	R(A-P) = 4	2.44 ± 0.92		2.95 ± 0.89	5.54 ± 1.55		
cor		R(H-F) = 1	R(H-F) = 2	R(H-F) = 3	R(H-F) = 1	R(H-F) = 2	R(H-F) = 3
	R(R-L) = 2	1.59 ± 0.25	1.70 ± 0.19	1.81 ± 0.27	2.03 ± 0.24	9.37 ± 2.91	29.54 ± 10.15
	R(R-L) = 3	1.47 ± 0.08	1.74 ± 0.18	1.97 ± 0.16	2.33 ± 0.14	23.76 ± 11.75	
	R(R-L) = 4	2.00 ± 0.18		2.69 ± 0.22	4.07 ± 0.61		
sag		R(H-F) = 1	R(H-F) = 2	R(H-F) = 3	R(H-F) = 1	R(H-F) = 2	R(H-F) = 3
	R(A-P) = 2	1.32 ± 0.10	1.45 ± 0.05	1.89 ± 0.08	2.01 ± 0.22	10.30 ± 4.86	27.65 ± 5.56
	R(A-P) = 3	1.51 ± 0.11	1.64 ± 0.13	2.18 ± 0.15	2.93 ± 0.54	18.25 ± 4.94	
	R(A-P) = 4	1.94 ± 0.39		2.72 ± 0.31	4.88 ± 0.54		

Supporting Table 5S4: Maximum g-factors of all 5 volunteers averaged with standard deviation for the 8Tx/32Rx and the 8Tx/Rx array.

Chapter 6 Summary and Discussion

Recently, the first clinical 7T MRI systems with a CE-label have been installed. Yet, clinical MR imaging at this field strength is only routinely possible in the head and in the knee.

In this thesis, simulations of 7T RF coil elements and arrays for both close-fitting and remote applications are presented. Furthermore, different coil setups for shoulder and body imaging are presented and evaluated.

Chapter 2 investigates the coupling behavior of micro stripline elements with meander structures at both ends using RF simulations. It is shown that for this specific element type, medium meander sizes are most advantageous with respect to next neighbor coupling when two elements are located side by side within an array configuration. This does only slightly change when the distance between the two elements or the distance between the elements and/or the phantom is varied. The main reason which can be identified is the change in power transfer between the different parts of the elements. The simulated coupling results were validated for four different pairs of elements in measurements with a network analyzer. Qualitative agreement is also achieved using B1+ measurements on a 7T MRI system. In conclusion, the coupling between micro stripline elements with meanders can be optimized depending on the specific application.

While in chapter 2 the investigated RF coil elements are heavily loaded (comparably small distance of about 3 cm to the subject), in chapter 3 results are presented that investigate the behavior of remote coil arrays where the RF coil elements are mounted on the boreliner. Consequently, the distance to the subject is in the range of 20-30 cm. The investigated elements are loops, micro striplines, meander elements, shielded dipoles with meanders, dipoles ($\lambda/2$) and shielded dipoles. These elements are combined in four different array designs with 4 or 8 RF coil elements each.

Coupling for these element types is increased when going from 4 to 8 elements. Regarding encoding capabilities, all arrays perform best in the central transversal slice followed by coronal and sagittal orientation. Other comparisons of important metrics like power and SAR efficiency indicate that 8 shielded dipoles are most favorable among the 22 different simulated configurations.

In chapter 4 the 8-channel transceiver 7-channel receive-only coil combination was successfully used for 7T shoulder imaging of volunteers and one patient. The coil setup itself could also be used for other applications such as musculoskeletal imaging in general or hip imaging in particular. Safe use of the coil setup is demonstrated by preceding field measurements. Adding the additional 7-channel receive-only coil boosts the SNR of the entire coil setup. In phantom measurements, an SNR gain factor of 3.76 can be achieved 42 mm from the phantom's surface. In addition, the acceleration capabilities of the setup are enhanced when both coils are used simultaneously. In vivo images show that either the right or the left shoulder of volunteers can be examined with the presented coil setup. A single RF shim is sufficient to cover the shoulder homogeneously. The examination of a 51-year old patient provides convincing image quality which can be used for adding high spatial resolution 7T imaging to the clinical 3T images. With the presented coil setup, more clinical follow-up studies are possible to evaluate diagnostic advantages of 7T shoulder MR imaging compared to 1.5 or 3T.

Results from the human body are presented in chapter 5 using an 8-channel transceiver 24-channel receive-only RF coil array and comparing this 8Tx32Rx coil to an 8TxRx coil with comparable configuration. As can be shown, the additional receive-only loops provide about 33% more SNR in the subject's center (and even more in regions close to the receive-only loops) as well as enhanced acceleration capabilities. Safe use is accomplished by comparing field measurements and simulated results of the same setup. Coupling between meander elements and loops of the same building block is

intrinsically low. In the center of a body-sized phantom a maximum B1+ amplitude of 12.42 μT can be achieved. Imaging results for volunteers indicate that one RF shim is sufficient to cover the coronal slice in the abdomen. Both the 8Tx32Rx and the 8TxRx RF coil array allow for fairly homogeneous transversal images when TIAMO is used. In the heart, very good blood/myocardium contrast is demonstrated when using the 8Tx32Rx coil. Pelvic imaging results in a volunteer indicate the potential of the 8Tx32Rx RF coil array when used for detection of potentially metastatic pelvic lymph nodes at a resolution of 0.66 x 0.66 0.66 mm³.

While it is undoubtedly more difficult to perform MRI at 7T compared to clinical field strength of 1.5 and 3T, the presented results indicate that there is potential for clinical applications at 7T besides neuro and musculoskeletal MRI.

Chapter 6 Samenvatting

Kort geleden zijn de eerste klinische 7T MRI systemen met CE goedkeuring geïnstalleerd. Deze worden klinisch echter alleen toegepast voor beeldvorming van het hoofd en de knie.

In deze thesis worden simulaties van 7T radiofrequente (RF) spoel elementen gepresenteerd voor zowel toepassingen waarbij de spoel dichtbij het onderzoeksobject wordt geplaatst en waarbij er een grotere afstand is tussen deze twee. Hiernaast worden ook verschillende spoel opstellingen beschreven voor de beeldvorming van de schouder en het lichaam.

In hoofdstuk 2 wordt met behulp van RF-simulaties het koppelgedrag tussen micro-stripline elementen met meander structuren onderzocht. Er wordt aangetoond dat voor dit specifiek element type, meander afmetingen van gemiddelde grootte de meeste voordelen bieden met betrekking tot koppeling wanneer deze twee elementen naast elkaar gelokaliseerd zijn binnen een array structuur. De koppeling tussen de elementen is grotendeels onafhankelijk van de afstand ertussen en de afstand tussen het element en het fantoom. De grootste reden voor variatie is de vermogensoverdracht tussen de verschillende onderdelen van de elementen. De gesimuleerde resultaten zijn met behulp van een netwerk analyser experimenteel bevestigd voor vier verschillende combinaties van twee elementen. Ook werd er in B1+ metingen op een 7T systeem een kwalitatieve overeenkomst aangetoond met de simulaties. Concluderend kan worden gesteld dat de koppeling tussen micro-stripline elementen met meander structuren geoptimaliseerd kan worden voor specifieke toepassingen.

Daar waar in hoofdstuk 2 de eigenschappen van spoелеlementen onderzocht worden onder een hoge belasting (relatief kleine afstand tussen spoel en onderzoeksobject van ongeveer 3 cm), wordt in hoofdstuk 3 nagegaan hoe deze elementen zich gedragen wanneer ze geplaatst worden

aan de randen van de tunnel van het MR-systeem. In dit geval zit er een afstand van 20-30 cm tussen de spoel en het onderzoeksonderwerp. Verschillende typen radiofrequente elementen worden onderzocht: loops, microstrip-lines, meander elementen, shielded dipoles met meanders, dipoles (half λ) en shielded dipoles. Deze elementen werden gecombineerd in vier verschillende array samenstellingen met elk 4 of 8 spoel elementen. De koppeling tussen de elementen is hoger bij 8 dan bij 4 elementen. Wat betreft de mogelijkheden met betrekking parallel imaging presteren alle array samenstellingen het best in de centrale transversale slice, gevolgd door de coronale en sagittale oriëntatie. In de vergelijking van de 22 verschillende gesimuleerde configuraties op basis van vermogen en SAR efficiëntie, laat de shielded dipole spoel met 8 elementen de beste resultaten zien.

In hoofdstuk 4 wordt de 8-kanaals zend- en ontvangstspoel in combinatie met de 7-kanaals ontvangstspoel succesvol gebruikt voor beeldvorming van de schouder op 7T in een vrijwilliger en een patiënt. De spoel kan ook goed gebruikt worden voor beeldvorming van bijvoorbeeld de heup of van het skeletstelsel in het algemeen. De veiligheid van de spoel werd aangetoond door middel van voorafgaande experimentele metingen van het elektromagnetische veld. Door de 7-kanaals ontvangst spoel toe te voegen aan de opstelling wordt de SNR verbeterd: in fantoomstudies werd hiermee een SNR versterkingsfactor van 3,76 verkregen op 42 mm afstand van het oppervlak van het fantoom. Daarbij geeft de combinatie met de ontvangstspoel ook nog meer mogelijkheden voor het versnellen van de beeldvorming. In vivo beeldvorming laat zien dat deze spoel gebruikt kan worden voor het afbeelden van zowel de linker als de rechter schouder. Het gebruik van één RF-shim is voldoende om de gehele schouder homogeen af te beelden. Onderzoek van een 51 jarige patiënt liet zien dat 7T MRI gebruikt kan worden voor hoge resolutie beeldvorming welke toegevoegd kan worden aan de standaard klinische 3T MRI. Met de in dit hoofdstuk

gepresenteerde spoel kunnen de voordelen van 7T MRI onderzocht worden ten opzichte van klinische 3T en 1.5T MRI.

Hoofdstuk 5 beschrijft de resultaten van een 8-kanaals zend- en ontvangspoel in combinatie met een 24-kanaals ontvangst spoel (8Tx32Rx). Deze spoel werd vergeleken met een 8-kanaals zend- en ontvangspoel zonder extra ontvangstkanalen (8TxRx). De extra ontvangst kanalen van de 8Tx32Rx spoel resulteren in een SNR toename van meer dan 33% in het centrum van een lichaams groot fantoom (en nog meer in de periferie). Daarnaast laten ze ook extra mogelijkheden zien voor acceleratie. De veiligheid van de spoelopstelling werd gevalideerd aan de hand van simulaties en experimentele metingen van het elektromagnetisch veld. De koppelingen tussen de meander elementen en de loops binnen één bouwblok zijn intrinsiek laag. In het centrum van een fantoom met lichaamsafmetingen werd een maximale B1+ amplitude behaald van 12,42 μ T. De resultaten in vrijwilligers laten zien dat één RF shim voldoende is om een coronale slice in het abdomen adequaat af te beelden en zowel de 8Tx32Rx als de 8TxRx spoel laten relatief homogene transversale beeldvorming zien in combinatie met TIAMO. In het hart wordt een zeer goed bloed/myocard contrast behaald bij gebruik van de 8Tx32Rx spoel. Beeldvorming van het bekken met de 8Tx32Rx spoel in een vrijwilliger met een resolutie van $0.66 \times 0.66 \times 0.66 \text{ mm}^3$ toont mogelijkheden voor het detecteren van potentiële lymfekliermetastasen.

Ondanks de uitdagingen die 7T MRI met zich meebrengt, laten de getoonde resultaten zien dat 7T potentie biedt voor klinische toepassingen, naast de al bestaande toepassingen in neuro en musculoskeletale MRI.

Chapter 8 Perspectives

With the introduction of a commercial 7T system with a CE-label, the number of about 60 research systems has already and will much likely be further increased. Yet, the extent of useful 7T applications is hard to predict. Currently, MR imaging at 7T is only possible in the head and in the knee using a maximum of 8 or 16 transmit channels with 8 or 16 kW RF peak power.

While head imaging is often the driver for innovation in MR, body imaging at 7T is especially difficult primarily due to B1 inhomogeneities (1,2). Currently, RF shimming (3,4) and TIAMO (5,6) can be used routinely to mitigate signal dropouts. Further research is performed using e.g. spokes (7) or parallel transmit (8–10) where not only the phase and amplitude among the RF channels is varied but also the shape of the pulse form that is played out and/or the gradient fields. These techniques require precise knowledge of the B1 and B0 fields. Regarding B1-mapping approaches have been presented to acquire reliable B1 maps even for body imaging (11). Combinations and further improvement of B0-mapping and shimming will further improve imaging capabilities. Applications for the 8Tx32Rx array are already currently investigated in the pelvis. Here, the coil can be used for the detection of metastatic lymph nodes without using an additional endorectal coil (12). A submillimeter resolution of 0.66 mm isotropic is possible in below 10 minutes with the 8Tx32Rx coil. This procedure has the potential to be one of the applications where 7T plays out its SNR advantage and can bring merit to the radiologist's diagnosis. Huge potential is also provided by X-nuclei since at 7T the SNR is much better when compared to 3T. If the Larmor frequency of the X-nuclei is lower e.g. below 128 MHz, the B1 inhomogeneities are also not severe. Multiparametric imaging in the prostate is only one example here (13).

Coil element and array development is a research and engineering task which will further be interesting and necessary. While even at 1.5 and 3T, where basically for all applications birdcage antennas are used for transmit and loop elements are used for receive, steady improvement is achieved in research and development, at 7T there is not even a most suitable coil element neither for transmit nor receive on which the majority of the community does agree. Most publications conclude that dipole-like elements are most suitable for transmit (14–17). Yet, the specific geometry of transmit or transceiver elements does vary from research site to research site and a comparison between all different elements and arrays can hardly be performed fairly. A general comparison is, consequently, very difficult.

In order to optimize the receive side, some publications present simulations and procedures to find the ultimate SNR in a phantom (18) or in body models (19). With this knowledge the maximum possible SNR received with any coil from outside the subject can be calculated (19).

Metrics for RF coils that can be derived from and optimized by simulations are power and SAR efficiency, coverage, degrees of freedom for shimming and parallel transmit (pTx) applications (20), size, geometry, and safety. Further practical issues are patient comfort, mechanical and electrical robustness, as well as flexibility. Optimization of so many variables necessarily leads to a compromise. While for 7T body imaging SAR efficiency and safety may be the most important features, the other characteristics are not to be neglected. With increasing simulation software and hardware more extensive simulations will be possible that could allow for an even better assessment and optimization of RF coils for 7T both for close-fitting and remote coils. In order to speed up the progress, improved collaboration between different research sites will be valuable.

To improve transmit capabilities, coil improvement goes hand in hand with improvements of the whole transmit chain. Here, more power and more

RF channels will increase the achievable flip angle and pTx capabilities. Currently, systems with 32-channels are built and evaluated (21–23). More channels also allow for better SAR efficiency if the SAR optimization is intrinsically included in the pulse calculation or shimming procedure.

While most 7T MR systems are currently equipped with a maximum of 32 receive channels which are exploited with the 8T32Rx RF body array, first systems with 64 receive channels are installed e.g. at the Center for Magnetic Resonance Research in Minnesota (23). There is also a constant drive to further expand the number of receive channels. Besides potential gains in SNR, a higher number of receive channels allows for faster acquisition using techniques like GRAPPA (24) or SMASH (25). Also simultaneous multi slice imaging, for example using PINS (26), is a promising approach for body imaging.

The drive for higher magnetic field strength has also led to plans for 14 or even 20T human MR system for research (27). With increasing field the B1 inhomogeneities, SAR and safety issues are even more severe (28). Yet, the higher frequencies also offer advantages like low cost hardware due to the frequency which then lies in the mobile phone frequency range, improved SNR (19) and the potential for other applications like hyperthermia (29).

Yet, due to the complexity and the fact that it is very time consuming to prove an added diagnostic value for the patient, 7T MRI will only slowly become more widely-used. Since the technology necessary for 7T MRI systems is expensive even compared to 3T MRI systems, radiologists who have also financial limitations, need to be able to significantly improve their diagnosis at least for specific questions.

References

1. Van de Moortele PF, Akgun C, Adriany G, Moeller S, Ritter J, Collins CM, Smith MB, Vaughan JT, Ugurbil K. B1 Destructive Interferences and Spatial Phase Patterns at 7 T with a Head Transceiver Array Coil. 2005;1518:1503–18.
2. Vaughan JT, Garwood M, Collins CM, Liu W, Delabarre L, Adriany G, Andersen P, Merkle H, Goebel R, Smith MB, et al. 7T vs. 4T: RF power, homogeneity, and signal-to-noise comparison in head images. Magn Reson Med 2001;46(1):24–30.
3. Collins CM, Liu W, Swift BJ, Smith MB. Combination of optimized transmit arrays and some receive array reconstruction methods can yield homogeneous images at very high frequencies. Magn Reson Med 2005;54(6):1327–32.
4. Mao W, Smith MB, Collins CM. Exploring the limits of RF shimming for high-field MRI of the human head. Magn Reson Med 2006;56(4):918–22.
5. Orzada S, Maderwald S, Poser BA, Bitz AK, Quick HH, Ladd ME. RF excitation using time interleaved acquisition of modes (TIAMO) to address B1 inhomogeneity in high-field MRI. Magn Reson Med 2010;64(2):327–33.
6. Orzada S, Johst S, Maderwald S, Bitz AK, Solbach K, Ladd ME. Mitigation of B1(+) inhomogeneity on single-channel transmit systems with TIAMO. Magn Reson Med 2013;70(1):290–4.

7. Schmitter S, DelaBarre L, Wu X, Greiser A, Wang D, Auerbach EJ, Vaughan JT, Uğurbil K, Van de Moortele P-F. Cardiac imaging at 7 Tesla: Single- and two-spoke radiofrequency pulse design with 16-channel parallel excitation. *Magn Reson Med* 2013;70(5):1210–9.
8. Katscher U, Börnert P, Leussler C, van den Brink JS. Transmit SENSE. *Magn Reson Med* 2003;49(1):144–50.
9. Grissom W, Yip C, Zhang Z, Stenger VA, Fessler JA, Noll DC. Spatial domain method for the design of RF pulses in multicoil parallel excitation. *Magn Reson Med* 2006;56(3):620–9.
10. Gras V, Mauconduit F, Vignaud A, Amadon A, Le Bihan D, Stöcker T, Boulant N. Design of universal parallel-transmit refocusing kT-point pulses and application to 3D T2-weighted imaging at 7T. *Magn Reson Med* 2018;80(1):53–65.
11. Brunheim S, Gratz M, Johst S, Bitz AK, Fiedler TM, Ladd ME, Quick HH, Orzada S. Fast and Accurate Multi-Channel B1+ Mapping Based on the TIAMO Technique for 7T UHF Body MRI. *Magn Reson Med* 2017;(epub ahead of print).
12. Philips BWJ, Fortuin AS, Orzada S, Scheenen TWJ, Maas MC. High resolution MR imaging of pelvic lymph nodes at 7 Tesla. *Magn Reson Med* 2017;78(3):1020–8.
13. Lagemaat MW, Philips BWJ, Vos EK, Van Uden MJ, Fütterer JJ, Jenniskens SF, Scheenen TWJ, Maas MC. Feasibility of Multiparametric Magnetic Resonance Imaging of the Prostate at 7 T. *Invest Radiol* 2017;52(5):295–301.

14. Erturk MA, Raaijmakers AJE, Adriany G, Tian J, Moortele P Van De, Berg CAT Van Den, Klomp DWJ. Comparison of 16-channel Stripline and 10-channel Fractionated Dipole Transceive Arrays for Body Imaging at 7T. *Proc Intl Soc MRM* 23 2015. p. 155268.
15. Raaijmakers AJE, Luijten PR, van den Berg CAT. Dipole antennas for ultrahigh-field body imaging: a comparison with loop coils. *NMR Biomed* 2016;29(9):1122–30.
16. Oezerdem C, Winter L, Graessl A, Paul K, Els A, Weinberger O, Rieger J, Kuehne A, Dieringer M, Hezel F, et al. 16-channel bow tie antenna transceiver array for cardiac MR at 7.0 tesla. *Magn Reson Med* 2016;75(6):2553–65.
17. Paška J, Cloos MA, Wiggins GC. A rigid, stand-off hybrid dipole, and birdcage coil array for 7 T body imaging. *Magn Reson Med* 2018;80(2):822–32.
18. Lattanzi R, Sodickson DK. Ideal current patterns yielding optimal signal-to-noise ratio and specific absorption rate in magnetic resonance imaging: computational methods and physical insights. *Magn Reson Med* 2012;68(1):286–304.
19. Guerin B, Villena JF, Polimeridis AG, Adalsteinsson E, Daniel L, White J, Wald LL. The Ultimate Signal-to-Noise Ratio in Realistic Body Models. *Magn Reson Med* 2017;78:1969–80.
20. Guérin B, Gebhardt M, Serano P, Adalsteinsson E, Hamm M, Pfeuffer J, Nistler J, Wald LL. Comparison of simulated parallel transmit body arrays at 3 T using excitation uniformity, global SAR, local SAR, and

- power efficiency metrics. *Magn Reson Med* 2015;73(3):1137–50.
21. Orzada S, Bitz AK, Solbach K, Ladd ME. A Receive Chain Add-On for Implementation of a 32-Channel Integrated Tx/Rx Body Coil and Use of Local Receive Arrays at 7 Tesla. *Proc Intl Soc MRM* 23 2015;3134.
 22. Orzada S, Bitz AK, Kraff O, Oehmigen M, Gratz M, Johst S, Völker MN, Rietsch SHG, Flöser M, Fiedler T, et al. A 32-channel integrated body coil for 7 Tesla whole-body imaging. *Proc Intl Soc MRM* 24 2016;167.
 23. Auerbach E, DelaBarre L, Van de Moortele P-F, Strupp J, Gumbrecht R, Potthast A, Pirkl G, Moeller S, Hanna B, Grant A, et al. An integrated 32-channel transmit and 64-channel receive 7 tesla MRI system. *Proc Intl Soc MRM* 25 2017;1218.
 24. Griswold MA, Jakob PM, Heidemann RM, Nittka M, Jellus V, Wang J, Kiefer B, Haase A. Generalized autocalibrating partially parallel acquisitions (GRAPPA). *Magn Reson Med* 2002;47(6):1202–10.
 25. Sodickson DK, Manning WJ. Simultaneous acquisition of spatial harmonics (SMASH): fast imaging with radiofrequency coil arrays. *Magn Reson Med* 1997;38(4):591–603.
 26. Norris DG, Koopmans PJ, Boyacioglu R, Barth M. Power independent of number of slices (PINS) radiofrequency pulses for low-power simultaneous multislice excitation. *Magn Reson Med* 2011;66(5):1234–40.
 27. Budinger TF, Bird MD, Frydman L, Long JR, Mareci TH, Rooney WD,

- Rosen B, Schenck JF, Schepkin VD, Sherry AD, et al. Toward 20 T magnetic resonance for human brain studies: opportunities for discovery and neuroscience rationale. *Magn Reson Mater Physics, Biol Med* 2016;29(3):617–39.
28. Winter L, Niendorf T. On the Electrodynamic Constraints and Antenna Array Design for Human In Vivo MR Up to 70 Tesla and EPR Up to 3GHz. *Proc Intl Soc MRM* 23 2015;1807.
29. Winter L, Oezerdem C, Hoffmann W, van de Lindt T, Periquito J, Ji Y, Ghadjar P, Budach V, Wust P, Niendorf T. Thermal magnetic resonance: physics considerations and electromagnetic field simulations up to 23.5 Tesla (1GHz). *Radiat Oncol Radiation Oncology*; 2015;10(1):201.

Acknowledgement

This work would not have been possible without the support of many people. Each of the persons I met during my work for this thesis (and before) contributed in their own special way and I am grateful for the experience of doing research in the Erwin L. Hahn Institute for MR Imaging. My time at the ELH was definitely the best so far in my life and I am happy to work in such a team which is extraordinary both from a scientific and personal point of view.

First of all I like to thank my promotor of my thesis Harald H. Quick. Thank you for giving me a place in your team in Erlangen during my master thesis and for offering me a position at the Erwin L. Hahn Institute in Essen. I am also grateful for the freedom you granted me regarding the priorities and topics of my research as well as for always finding time whenever I needed support. I learned a lot from your experience of how to write and submit paper manuscripts and give presentations. My sincere thanks also to David Norris for giving valuable feedback about this work and for supervising my thesis as promotor.

A big thank-you goes to Arend Heerschap, Radboud University Nijmegen, Andrew G. Webb, University Leiden, and Dennis Klomp, University Medical Center Utrecht, for being the thesis supervisory committee of this work.

I also would like to thank Mark Ladd for his support. Although I am sure that you have enough work to do with your team in Heidelberg, you always found time to proof read my paper manuscripts. Thanks for giving me the opportunity to work on the MRexcite project. Furthermore, I like to thank Tom Scheenen for the collaboration and for finding good use of my coil for body imaging.

Stephan Orzada, thank you for being such a great mentor. I highly appreciate your broad knowledge about MRI, Matlab, engineering and your

practical approach. Thank you also for your positive attitude and cheerful nature.

Thank you Stefan Maderwald for all your help with the scanner, protocols, ELH infrastructure and for sharing your knowledge about clinical MRI and scientific work. Furthermore, I like to thank you for finding time to be a volunteer so often.

Thank you Oliver Kraff for sharing your office with me and for performing nice shoulder images with the coil setup. Thank you for sharing your experience and also for organizing joyful events like Currywurst-eating and the coalmine exploration.

Marcel Gratz, thank you for all your help with computers, IT infrastructure, networks and programming. Your technical expertise in these areas, in MRI and your high scientific standard makes you invaluable for the whole institute. I am also grateful for interesting and funny conversations about music, Helge Schneider etc. I will never forget listening to elevator sounds in Singapore.

Thank you very much Maximilian Völker for always finding a good joke and your good mood. Thank you for your help with sequences and phantom cooking. Thanks goes also to Bixia Chen for saving my life at least twice during our stays in Singapore and Hawaii. Thank you both for adding me to your group on our pre- or post-ISMRM travels.

A big thank-you goes to Sascha Brunheim for his help and time with in-vivo measurements and B1 mapping. Without your help we would never have achieved useful B1 maps for our body measurements. Thank you also for being a volunteer so often. I wish you all the best for your work in Bonn.

Andreas Bitz, I am very thankful for all your help with simulations and simulation hardware, last but not least with the new head coil. Thank you for

your professional explanations and your friendly character. I hope you will again be able to find (more) time for MRI research soon.

Thank you Sören Johst for sharing your office with me and supporting me whenever possible. I really appreciate your calm and funny character. It was very amusing being in the X-mas committee with you and listening to announcements in the escalator during our stay in Singapore.

Viktor Pfaffenrot thanks for your support with the detuning board and for testing of the 32-channel switchboxes. I hope the new head coil will be a nice boost for your research. I wish you all the best for your next PhD steps.

Many thanks Peter Koopmans for providing the budget for the new head coils and for all critical questions. I wish you all the best for your new role as dad.

Bart van de Bank thank you very much for helping me when I just started building coils in the ELH. Thank you also for your cheerful nature and good mood. I am convinced you are an awesome teacher now.

Thank you Yacine Noureddine for introducing me to field measurements with the robot and for being such a funny guy. I wish you all the best for your job in Hamburg.

Jonathan Weine, thanks for your help with hardware construction, especially with bending all the loops. It really was a pleasure working with you. Thanks goes also to Daniel Leinweber for his work on the head coil and the TR-switches, Sarah Handtke for the CAD model of the head coil, Leonard Ruschen, Osama Al Rifai, Laura Fuentes Vallejos, Jessica Kohl and Raphaela Berghs. I wish all of you the very best for your further path.

I also like to thank Bart Philips, Mark van Uden and Rutger Stijns from the Radboud University Medical Center for the collaboration, Thomas Fiedler and Arthur Magill from the DKFZ Heidelberg for interesting discussions,

Beate Fraß, Corinna Heldt and Judith Kösters for managing the institute and help with bureaucratic tasks, Sigrid Radermacher for helping with all the online orders, Stefanie Zurek for organizing, Mark Oehmigen for his help with CAD modelling, Nicolai Spicher for sharing a room in Toronto and for interesting conversations about IT, Jennifer Schulz for sharing her experience about PhD thesis and defense (welcome in our office), Andrea Lazik for her radiological expertise and the nice collaboration, Juliane Göbel for the collaboration regarding cardiac imaging, Thomas Ernst for interesting discussions, Katharina Schröder and Nora Schulz for very amusing lunchtime in the ELH, Jan-Willem Thielen for always being funny, Donghyun Hong for the amazing food experience in Paris (I wish you all the best for your new job), Seyedmorteza Rohani Rankouhi for nice high resolution images of my brain and Karin Hensel and Dieter Brym from the mechanical workshop in Essen for their professional work on coil housings.

I like to thank my former colleagues from Erlangen, Susanne Ziegler, Harald Braun, Bharath Navalpakkam, Daniel Paulus, Bassim Aklan, René Kartmann and Christopher Ströhlein. I also like to thank Razvan Lazar from Siemens Healthcare for being such a superb mentor during my time as working student.

Ich danke meinen Schulkollegen Sascha M., Sebastian H., Manuel, Fabian, Christoph T. und Christoph P. für unsere schöne gemeinsame Zeit. Ebenfalls danke ich meinem Kumpel Sebastian K. für interessante Gespräche und entspannende Spaziergänge. Vielen Dank auch an meine Studienkollegen Sascha, Mav und Pat. Danke für jeden gemeinsamen Lernmarathon, die Mensa-/Restaurantbesuche und Veranstaltungen wie Projektpraktikum und Zockabende.

Des Weiteren möchte ich meinen Bandkollegen Andi, Chrissi, Hammers, Pat, Philipp und Joli danken. Obwohl wir inzwischen innerhalb von ganz Deutschland verstreut sind schaffen wir es regelmäßig zusammen zu spielen.

Ihr seid mit Sicherheit der coolste Sauhaufen den es gibt. Danke Sirs! Mein Dank geht außerdem an meine beiden Musiklehrer Jessica und Borris.

Tausend Dank auch an meine Großeltern Frieda, Eli, Gerhard und Hans. Insbesondere denke ich an meinen Opa Gerhard: Ich weiß wie stolz du wärst.

Bedanken möchte ich mich auch bei meiner Patentante Petra und meinen Cousinen Lena und Luisa. Ich freue mich, dass es inzwischen eine kleine Tradition geworden ist zusammen Weihnachten zu feiern.

Vielen Dank Iris und Günter, dass ihr mich direkt in eure Familie aufgenommen habt. Vielen Dank für eure Herzlichkeit und Großzügigkeit. Carina und ich freuen uns immer bei euch zu Gast zu sein.

Philipp, ich danke dir für unsere bisherige gemeinsame Zeit und Jugend. Ich finde es super, dass wir zusammen musizieren und bin begeistert von deinen Buchempfehlungen und unseren interessanten Gesprächen. Außerdem bin ich froh, dass dir deine eigene wissenschaftliche Arbeit in Berlin gefällt und bin überzeugt, dass du mehr als erfolgreich sein wirst. Einen besseren kleinen Bruder hätte ich mir wirklich nicht wünschen können.

Mein größter Dank geht an meine Eltern, Evi und Norbert für ihre immerwährende Unterstützung und dafür, dass sie mir und Philipp ein Studium ermöglicht haben. Es hat uns bei euch an nichts gemangelt. Papa, danke für all die Dinge die ich von dir lernen durfte. Du warst mein erster Mentor und ich lerne immer noch von dir. Mama, danke, dass du mir auch in schwierigen Situationen geholfen hast und mir notfalls auch den sprichwörtlichen Tritt in den A.... gegeben hast. Dass ich meinen Weg bis hierher gegangen bin verdanke ich in erster Linie euch beiden!

Zuletzt möchte ich mich noch bei meiner Partnerin Carina bedanken. Danke, dass du mir in Essen eine Heimat gegeben hast. Danke auch für dein Verständnis, wenn ich abends später nach Hause gekommen bin oder nach der Arbeit keinen guten Gesprächspartner mehr abgegeben habe. Ich freue

mich, dass wir so viele Dinge gemeinsam machen können. Gleichzeitig lässt du mir Raum eigene Dinge, wie die Musik, zu verfolgen. Danke für deine Aufgeschlossenheit und deinen Humor. Ich bin glücklich, dass wir uns gefunden haben.

Curriculum Vitae

Stefan Rietsch, born June 29th, 1988 in Erlangen, Germany

Education

Since 03/2014	Erwin L. Hahn Institute for MR Imaging, University Duisburg-Essen, Germany Highfield and Hybrid MR Imaging, University Hospital Essen, Germany PhD candidate
10/2011 – 10/2013	Friedrich-Alexander University Erlangen/Nürnberg, Germany, Master of Science physics
10/2008 – 10/2011	Friedrich-Alexander University Erlangen/Nürnberg, Germany, Bachelor of Science physics
09/1998 – 06/2007	Emil-von-Behring Gymnasium, Spardorf, Germany Abitur (secondary school)

Experience

Since 03/2014	Erwin L. Hahn Institute for MR Imaging, University Duisburg-Essen, Germany Highfield and Hybrid MR Imaging, University Hospital Essen, Germany research assistant: construction and simulation of radiofrequency coils
10/2013 – 12/2013	Institute for Medical Physics, Erlangen, Germany Research assistant in the Section of MR-Imaging Evaluation of methods for position registration of flexible RF coils
11/2010 – 07/2011	Siemens AG, Healthcare Sector, Erlangen, Germany Working student in the Magnetic Resonance Group,

	Research & Development, Hardware, Bodycoil & Integration Planning, construction and evaluation of a multidimensional MR-Bodycoil and related work
08/2009 – 09/2009	Siemens AG, Healthcare Sector, Erlangen, Germany Working student in the Imaging & IT Division Fabrication of Bodycoils for Magnetic Resonance Imaging
09/2007 – 05/2008	Civilian service, German Caritas Association in Neunkirchen am Brand, Germany

Stipends & Awards

2015- 2017	Educational stipends, International Society for Magnetic Resonance in Medicine (ISMRM), Berkley CA, USA
2016, 2018	Travel stipends, German Academic Exchange Service (DAAD)
2016	Magna Cum Laude Merit Award, ISMRM
2018	Young Investigator Award, Deutsche Gesellschaft für medizinische Physik (DGMP)

Scientific Publications

Original Papers	4 as first author, 1 as co-author
Conference Abstracts	8 as first author, 7 as co-author

Patents

2014	Method for determining a position-dependent attenuation map of surface coils of a magnetic resonance/PET apparatus, Patent number: 9541622
------	--

About the author

Stefan Rietsch was born in Erlangen, Germany the 29th of June 1988. He grew up in Dormitz (near Erlangen), with his parents Evi and Norbert and his brother Philipp. Following his secondary education at the Emil-von-Behring-Gymnasium in Spardorf in 2007, he worked in the day care station of the German Caritas Association in Neunkirchen am Brand to complete his civilian service.

From 2008 to 2013 he studied physics at the Friedrich-Alexander-University in Erlangen. During that time he also got in touch with MRI as a working student in the Research & Development department of Siemens where he was working on multi-channel bodycoil antennas. He finished his studies with the master thesis 'Integrated PET/MR: Position registration of flexible radiofrequency coils into PET attenuation correction' which was supervised by Prof. Dr. Harald H. Quick.

After moving to Essen he started his work as research assistant at the Erwin L. Hahn Institute for MR Imaging in March 2014 in the group 'highfield and hybrid MR Imaging' of Prof. Dr. Harald H. Quick. There, he focused on the simulation, construction and evaluation of radiofrequency coils for 7T MRI.

He has been visiting the ISMRM since 2014 and was awarded with a 'Magna Cum Laude' ISMRM merit award in 2016, several ISMRM stipends and two stipends of the German Academic Exchange Service (DAAD) as well as the Young Investigator Award of the German Society for medical physics (DGMP). He had the chance to review abstracts for the ISMRM 2018 and 2019 and peer-review publications for the journals Magnetic Resonance in Medicine (MRM), PLOS One, and Magnetic Resonance Materials in Physics, Biology and Medicine (MAGMA).

Stefan Rietsch lives with his life partner Carina Oberst in Essen, Germany.
In his free time he enjoys sports, singing and playing guitar.